Politecnico di Torino

ScuDo
Scuola di Dottorato ~ Doctoral School
WHAT YOU ARE, TAKES YOU FAR

Doctoral Dissertation
Doctoral Program in Electronic Engineering (38^{th}cycle)

Optical Systems for Advanced Sensing Application

From environment to cultural heritage monitoring

By

Chiara Bellezza Prinsi

******

Supervisor(s):
Prof. Perrone Guido, Supervisor
Prof. Vallan Alberto, Co-Supervisor

Doctoral Examination Committee:
Prof. Scalise Lorenzo, Referee, Università Politecnica delle Marche
Prof. Zaffora Andrea, Referee, Università di Palermo
Prof. Grassini Sabrina, Politecnico di Torino

Politecnico di Torino
2026

Declaration

I hereby declare that, the contents and organization of this dissertation constitute my own original work and does not compromise in any way the rights of third parties, including those relating to the security of personal data.

Chiara Bellezza Prinsi
2026

* This dissertation is presented in partial fulfillment of the requirements for **Ph.D. degree** in the Graduate School of Politecnico di Torino (ScuDo).

Abstract

Optical technologies are known for their capability of providing a core technology for the development of high-performances sensors for critical monitoring applications; however, their widespread adoption remains mainly limited by the costs, size, and complexity of the interrogation equipment.

This research addresses these challenge by investigating the design of simple, robust, and low-cost sensing devices, targeting the main application of extensive monitoring of chemical and biochemical quantities and parameters.

Current monitoring strategies largely rely on discrete sampling, followed by laboratory analysis using complex analytical instruments, which require specialized expertise. On the contrary, future developments are expected to promote ubiquitous, real-time, and non-invasive monitoring through compact and affordable optical systems. The approaches proposed in this thesis aim to enable continuous in situ assessment across diverse contexts, including environmental systems, water quality monitoring, agri-food sustainability and safety, as well as the protection of cultural and natural heritage

This evolution aligns with several United Nations Sustainable Development Goals (SDGs), such as clean water and sanitation (SDG 6), sustainable agriculture and food safety (SDGs 2 and 3), and sustainable cities and communities (SDG 11). In addition, it can significantly contribute to improving cultural heritage preservation procedures, a sector particular relevant in Italy since it also represents a key economic asset.

The research explores and experimentally validates two main application areas: water monitoring and cultural heritage conservation.

For water monitoring, Fluorescence Spectroscopy (FS) and fiber-based Surface Plasmon Resonance (SPR) sensors, integrated with Artificial Intelligence (AI) algo-

rithms, are developed for the detection and identification of contaminants. SPR-based refractometers enable the measurement of refractive index variations as indicators of contamination, while fluorescence combined with microfluidics allows accurate and continuous pH monitoring. The SPR sensor design is optimized through numerical simulations to identify the most suitable geometry for experimental implementation, followed by the development of an automated calibration procedure. Similarly, a dedicated calibration method is established for fluorescence-based sensing, ensuring accurate and repeatable pH measurements across the full operational range.

For cultural heritage applications, the combination of fluorescence imaging, Optical Coherence Tomography (OCT), and AI-powered segmentation algorithms enables the discrimination between pigment and varnish layers, providing a non-invasive and cost-effective alternative to traditional analytical methods. OCT techniques allow real-time estimation of the thickness and surface roughness of protective layers on artworks, supporting safer and more informed conservation treatments. The simultaneous use of fluorescence further enhances the capability to assess the state and thickness of protective layers in real time.

Overall, the results demonstrate the effectiveness and versatility of optical fiber and light-based sensing approaches for real-time, minimally invasive, and distributed monitoring. The developed solutions represent a significant step toward the practical implementation of compact, affordable, and high-performance optical systems for environmental and cultural heritage applications. Through careful sensor design, proper calibration, and the integration of complementary optical techniques, this research confirms that high measurement accuracy can be achieved while maintaining portability, low cost, and ease of use.

Contents

List of Figures

List of Tables

Chapter 1

Introduction

Optical technologies are well known to enable the development of high-performance sensors for critical monitoring applications, although their wide deployment is typically limited by the costs, size, and complexity of the interrogation equipment. The challenge is thus how to exploit these approaches to build simple, robust, and low-cost devices, in particular for continuous monitoring of chemicals and biochemicals. At present, most chemical monitoring strategies still rely on discrete sampling, transportation of samples to specialized laboratories, use of complex analytical instruments, and expertise of trained personnel. However, future developments are expected to enable a transition towards ubiquitous, real-time, non-invasive assessment through compact and low-cost devices. Such an approach would allow continuous, in situ monitoring across diverse contexts, ranging from environmental systems, water quality monitoring, agri-food sustainability and safety, to cultural and natural heritage protection. This evolution is strongly aligned with several United Nations Sustainable Development Goals (SDGs) [1]. For instance, SDG 6 aims to ensure access to clean and safe water for all; however, billions of people worldwide still live without safe drinking water. Similarly, SDG 2 promotes sustainable agriculture, while food safety is recognized as a fundamental requirement for healthy lives (SDG 3). Furthermore, cultural heritage represents one of the most significant assets in countries such as Italy, where its preservation is essential not only for safeguarding it for future generations (SDG 11) but also for its considerable economic impact.

The aim of the research is to exploit a combination of light-based approaches for the continuous, real-time, and minimally invasive evaluation of changes in the compo-

sition of substances relevant for "environmental" (in the broadest sense) monitoring applications. In particular, two main applications have been studied, developing and experimentally validating specific photonic-based monitoring solutions:

- **Water quality monitoring** The goal of this application is to detect and identify contaminants such as bacteria or PFAS through the combination of Fluorescence Spectroscopy (FS) and fiber-based Surface Plasmon Resonance (SPR) integrated with Artificial Intelligence (AI) techniques. More in detail:
  - SPR, implemented in an all-fiber configuration, is used to track the changes in the refractive index, which can be used as first indicator of water contamination. This represents a first step towards the development of an integrated device that can be used directly on pipes. Particular attention is devoted to balance performance and costs to enable adoption of the developed solution also in developing Countries, in which the water quality problem is the worst.
  - Fluorescence is exploited to develop a microfluidic system for the continuous monitoring of pH. This work constitutes a significant advancement toward the development of an integrated device able to detect and identify contaminants such as bacteria and PFAS directly in pipelines.
- **Cultural heritage monitoring** The goal for this application is to develop a tool that supports conservators during interventions. Cleaning of historical artifacts has always represented a critical treatment in conservation practice, requiring a delicate balance between effective removal of unwanted materials and preservation of the original surface.

  The combination of Fluorescence with OCT and AI empowered image segmentation algorithms makes it possible to discriminate pigment layers from protective varnish layers, resulting in a cost-effective and noninvasive tool (unlike SEM imaging) that can be routinely applied to reduce errors due to the conservator's ability to correctly identify the various layers.
  - OCT (Optical Coherence Tomography) can be used to develop a widely deployable, real-time, and non-invasive procedure to estimate the thickness of protective transparent layers on ancient artifacts, which must be removed during conservation treatments.

  - Fluorescence for the precise identification of the different layer stratification.

1.1 Optical Sensor Overview

What is an optical sensor?

An optical sensor is a device that detects and measures changes in light properties (such as intensity, wavelength, phase, or polarization) in response to an external perturbation and converts them into a readable signal, typically electrical or digital. Optical sensors can be used to monitor physical, chemical, or biological phenomena [2]. They are widely used in Earth observation, climate monitoring, and disaster management, offering precise and real-time data to support environmental and scientific research. By detecting and analyzing optical signals in various spectral bands, they provide critical insights into water quality, air pollution, greenhouse gas emissions, deforestation, oceanic currents, and natural disasters such as wildfires, hurricanes, and volcanic eruptions. The focus of this work will be on optical sensors implemented using free-space discrete components or optical fibers, the so-called Fiber Optic Sensors (FOSs), due to their unique advantages, including compactness, lightweight, immunity to electromagnetic interference, and capability for distributed sensing. Fiber optic sensors are excellent candidates for monitoring environmental changes and they offer many advantages over conventional electronic sensors such as:

- Easy integration into a wide variety of structures, with reduced invasive impact due to their small size and lightweight.
- Intrinsic impossibility to cause electrocution or start fires for the absence of electric current.
- Immunity to electromagnetic and radio frequency interference.
- Robustness and resistance to harsh environments.
- High sensitivity.
- Multiplexing capability to form sensing networks.
- Remote sensing capability.

- Multifunctional sensing capabilities such as strain, pressure, corrosion, temperature and acoustic signals.

Fiber optic sensors have been used to monitor a wide range of environmental parameters such as position, vibration, strain, temperature, humidity, viscosity, chemicals, pressure, current, electric field and several other environmental factors [3].

Fiber optic sensors can be classified according to three criteria: sensing location, operating principle, and application [4].

As for the sensing location, the classification can be further subdivided in intrinsic or extrinsic: the first type senses direct changes in an optical property of an analyte (e.g. chlorophyll, hemoglobin or flavine). Those sensors are simple and robust but not selective: anything absorbing at the same wavelength will interfere. The second type of sensors (namely extrinsic one), require a chemical indicator to produce an optical signal or a chemical coating such as organic dyes, quantum dots, polymers, Sol-Gels, hydrogels and nanomaterials. Those sensors presents a high sensitivity due to selective chemical reagents and can be used in remote, confined or harsh locations.

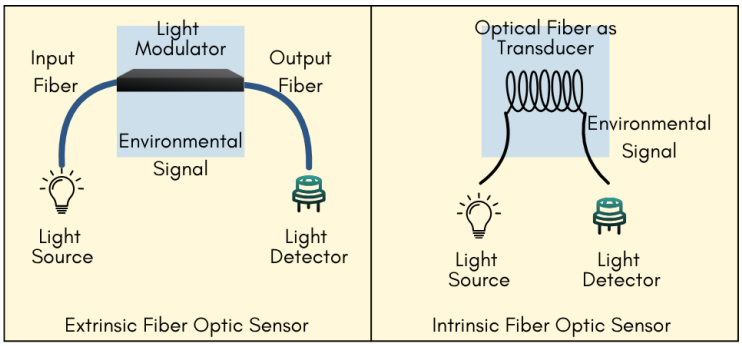

Fig. 1.1 Extrinsic and intrinsic types of fiber optic sensors.

From the point of view of the sensing principle, FOS operate in exactly the opposite way of telecommunications. Indeed, while optical communications goal is to transmit signals with minimal distortion and interference, optical sensing fundamentally depends on the intentional perturbations of the optical signal caused by the parameter being measured. This characteristic allows optical sensors to be designed based on variations in different properties of an optical wave, such as amplitude modulation, phase modulation, polarization changes, and wavelength conversion [5].

1. **Amplitude modulation**: typical of intensity-based sensors (sometimes also called "intensiometric"), which operate by detecting variations in the intensity of light due to absorption, scattering, or reflection. This approach is the simplest and most cost-effective optical solution, since it requires only a light source (a Superluminescent LED, SLED, or a laser, typically a semiconductor laser diode, for more demanding applications), the transmission medium (which can be air or, most commonly, an optical fiber) that serves also as the transducer, and a photodetector at the receiving end. This simple design makes these sensors an attractive choice, although this lack of complexity comes at the expense of very poor selectivity, since any type of perturbation that affects the received power, including fluctuations in the source emissions, is indistinguishable from the actual quantity under measurement.

2. **Phase modulation**: typical of interferometric sensors, which rely on the interference between two co- or counter-propagating waves that are affected by different phase changes. The measured physical quantity (e.g., strain, pressure, temperature) induces a phase shift in one of the two optical signals, which leads to modification in the interference pattern. These sensors are highly sensitive and widely used in precision measurements, being capable of detecting extremely small changes in physical parameters. Unlike intensity-based sensors, they are less affected by variations in optical power due to source fluctuations or other types of losses. When implemented in optical fibers, multiplexing is possible, allowing for the development of quasi-distributed sensing networks.

3. **Polarization change**: typical of polarimetric sensors, which exploit the changes in the polarization state of light as it propagates through an optical medium. The measured physical parameter (e.g., stress, strain, temperature, or magnetic fields) induces birefringence or alters the polarization state, which can then be analyzed using polarimeters or other detection techniques. The main advantages are high achievable sensitivity and immunity to intensity fluctuations. However, they also suffer from poor selectivity because temperature fluctuations, mechanical stress, or fiber bending (in case of optical fiber-based devices) can induce unwanted polarization changes.

4. **Wavelength conversion**: typical of inelastic scattering approaches or of spectroscopic techniques. These sensors operate by detecting changes in the

wavelength (or frequency) of light induced by the interaction between the optical signal and the measured physical parameter. This can be achieved through linear (e.g., Rayleigh scattering) and nonlinear optical effects (such as Raman or Brillouin scattering), fluorescence, or shifts in the absorption/emission spectrum of specialized materials. These sensors are particularly useful in applications requiring highly selective and sensitive detection.

Several specific approaches can be employed to implement these four categories, and the most commonly used ones are those described below.

- Absorption sensors, the prototype of the intensity-based category, operate by detecting changes in received signal intensity due to the absorption of specific wavelengths by the target substance.
- Scattering sensors – another type of intensity-based optical sensors – detect power variations at the receiver caused by scattering phenomena [6, 7]. When implemented as free-space discrete-component sensors, they measure light scattered by macroscopic particles, enabling the evaluation of particle concentrations in aerosols or fluids.
- Evanescent wave sensors are intensity-based sensors that exploit the interaction of the exponentially decaying portion of a guided field that extends beyond the core of an optical waveguide (e.g., an optical fiber or a planar waveguide), the so-called “evanescent field tails", with the surrounding medium. These sensors are widely used in chemical and biosensing applications, such as detecting specific particles, monitoring environmental pollutants, and performing real-time biomedical diagnostics exploiting the high sensitivity of the evanescent tails to changes in refractive index. Upon proper functionalization, the sensor can be tailored to detect specific bio-molecules. A notable variation of this approach is Surface Plasmon Resonance (SPR), which enhances sensitivity by exploiting the resonant oscillations of conduction electrons at the interface between a metal and a dielectric medium. SPR-based sensors are extensively used in bio molecular interaction studies, drug discovery, and clinical diagnostics due to their ability to provide label-free, highly sensitive detection. These sensors can detect trace amounts of hazardous gases such as hydrogen, oxygen, and Volatile Organic Compounds (VOCs). Alternatively, evanescent

wave sensors can also monitor air and water quality, humidity, and chemical contaminants [8].

- Interferometric sensors, such as Michelson [9], Fabry-Pérot, Mach-Zehnder [10], and Sagnac interferometers. The Michelson interferometer is one of the most well-known configurations, using a beam splitter to divide light into two perpendicular arms; then, the reflected beams recombine, producing interference patterns. The resulting interference pattern depends on the difference in optical path length between the two arms. By adjusting the position of one mirror, constructive or destructive interference can be observed. This principle allows for precise measurements of wavelength, small displacements, and refractive index variations. The interferometer's high sensitivity makes it fundamental in fields such as metrology, experimental physics, and is also widely used in OCT for high-resolution imaging.

- Fiber Bragg Grating (FBG) sensors, among the most widely used fiber optic sensing technologies, rely on periodic variations in the refractive index of an optical fiber core, which causes the selective reflection of specific wavelengths (the Bragg wavelength). Any external perturbation such as strain, temperature, pressure, or mechanical deformation, induces a shift in the reflected wavelength, enabling precise measurements. FBG sensors have established themselves as the gold standard in fiber optic sensing, thanks to their unparalleled combination of sensitivity, robustness, adaptability, and ability to provide quasi-distributed, real-time monitoring with high accuracy [11].

- Luminescence and fluorescence-based sensors relate the quantity under measurement to the fluorescent emission from target molecules when excited by a specific light source.

- Raman and spectroscopic sensors analyze molecular vibrations to identify chemical compounds. Other applications include the monitoring of gases and of bio-molecules.

Part I

Water monitoring

Chapter 2

Water monitoring

The World must pursue sustainable development, as evidence clearly shows that the Earth's resources are finite and must be managed responsibly.

Water is one of those resources and the climate change is exacerbating the already critical shortage of uncontaminated freshwater so much that millions of people continue to die every year from waterborne disease, making the UN's 2030 SDG 6, Safe Water for All, (United Nations Sustainable Development Goal) far from being realized. Still today one third of the population in the World is treated for waterborne infections due to the poor access to free and clean water. And besides, in many Countries water sources are polluted by untreated industrial wastes, pesticides and fertilizers.

This calls for the availability of a new, continuous, real-time, and environmental friendly method to monitor the quality of water. Currently, commonly used water treatment systems do not satisfy all these requirements because the analysis is based on periodic and long-lasting measurement processes than can be carried out only in dedicated labs by trained technicians. Sampling and transportation are quite critical parts because it must be guaranteed that the sample represents the water it was taken from, maintaining at least the specific properties that are supposed to be analyzed. The most common tests are chemo-physical (turbidity, temperature, pH, and presence or concentration of contaminants such as PFAS, heavy metal ion, ammonia, chloride etc.), bacteriological, radiological, and overall acceptability (odor, taste, color) analyses.

This at least in highly developed Countries. But in Countries or areas in which the water distribution system is not well established the distribution systems are characterized by unexpected events that interrupt the water flow or introduce contamination. In such cases the authorities can ensure the quality of water only at some key points of the system, but it is impossible to guarantee not the quality but even not the safety at the final consumer. Considering the random variations typical of discontinuous service cases, sampling and analyzing periodically does not help and the tragic numbers regarding the diseases and deaths caused by contaminated water reported before confirm the critical importance of ensuring a constant water quality. The optimal solution to these problems would be to monitor the water quality in real time and in a distributed way to inform the population in case of hazardous circumstances.

Photonic-based technologies can be used to develop highly sensitive devices for the detection of contamination in water, exploiting a number of different approaches, going from plasmon surface resonance to spectroscopic techniques. Of course, the complexity makes not feasible a low-cost solution if one aims to quantify the same amount of parameters of traditional analyses carried out in laboratories but it becomes a realistic goal if some simplifications are introduced. In this spirit, this dissertation discusses the first steps towards a real-time water quality monitoring device suitable for wide deployment, which is based on the continuous monitoring of different parameters such as Refractive Index (RI) and pH, as a preliminary starting point.

Refractive index is monitored though a fiber-based refractometer that exploits the physical phenomenon called “Surface Plasmon Resonance” (SPR), which is know for its higher sensitivity and resolution with respect to other configurations with similar applications. The first part of the work is focused on the simulation of the fiber geometry in order to determine the most suitable one in terms of easy of fabrication and best performance. Once the perfect geometry is found the sensor is calibrated with the aid of Artificial Intelligence approaches to characterize the response without the need to test every single sensor. As a future perspective, the fiber could be also functionalized to enable a selective detection and thus to monitor specific contaminants such as bacteria or PFAS, and not just the changes in the refractive index regardless their causes.

The continuous measurement of pH is fundamental not only in environmental monitoring applications, but also to ensure the consistency of many industrial processes. In environmental applications, pH is one of key parameters to be evaluated for assessing water quality and the health status of aquatic ecosystems. In this application the target measurement range is close to neutral (pH values from 6.5 to 8.5), as water that is too acidic or too alkaline harms wildlife and indicates pollution, such as acid rain, industrial discharges or excessive agricultural residues.

Traditional pH measurement methods are either overly simplistic and insufficiently accurate for process monitoring, such as pH-indicator strips, or rely on bulky, expensive instrumentation that requires calibration, maintenance, and trained operators. Additionally, both approaches often involve manual sampling or periodic calibration, which slows down response times, representing an important drawback in dynamic situations. An alternative is the use of electrochemical pH probes for in-situ measurements. These devices consist of two electrodes: a sensor electrode and a reference electrode, the latter typically made to have a neutral pH of 7. The pH is determined by measuring the potential difference between these electrodes, which, in turns, depends on the hydrogen ion concentration in the solution. Electrochemical pH sensors are characterized by compactness, high sensitivity, and ease of use, with the added advantage of enabling remote monitoring. However, they are not suitable for continuous measurements due to the need for regular calibration, cleaning, and proper storage to ensure accuracy. Furthermore, these sensors have limited durability and are prone to drifting over time, which can impact their reliability in long-term applications.

A more effective solution for continuous monitoring applications, combining high sensitivity with remote operation, is provided by photonic-based technologies. These can be implemented through a number of different approaches, the most common being surface plasmon resonance, Fiber Bragg Gratings (FBGs), and spectroscopic techniques. Among these, fluorescence-based pH sensors are particularly attractive because the strong correlation between fluorescence changes and pH variations results in a higher signal-to-noise ratio and reduced artifacts due to cross-sensitivity phenomena. A fluorescence-based sensing system can be built by sampling a small quantity of the liquid under test using a micro-pump and introducing a specific dye via another micro-pump. The pH is then determined by analyzing the dyes' fluorescence, which changes in response to pH-induced alterations in its electronic structure. This approach offers both precision and reliability, making it highly suitable for

continuous and remote pH monitoring applications. In recent years, fluorescence spectroscopy has gained significant popularity and has been successfully employed in various fields, including the detection of nitrites and nitrates in environmental samples, the identification of bacteria, and the analysis of wastewater composition.

The second part of the work is dedicated to the characterization of a selected dye in terms of pH, temperature, and LED influence. The sensor is then calibrated in a lab-setup for the analysis of the data both with a “traditional” approach and with artificial intelligence for a broader estimation of water quality parameters. The sensor is then integrated into a microfluidic circuit to be used “on-site”.

Chapter 3

SPR - Theoretical background

Before addressing the achievements in developing a low-cost SPR-based system for water contamination monitoring, it is useful to briefly review the underlying physical phenomenon.

SPR relies on the excitation of the surface electrons of a conductive layer (metal, plasma) by properly polarized light at a metal–dielectric interface that shows up as a longitudinal EM wave. Under certain conditions the energy carried by the photons, is transferred to the surface electrons oscillating synchronously and produce a surface plasma oscillation that propagates along the surface. This oscillation is what it is named a Surface Plasma Wave (SPW). Such a wave has a resonance-like range of oscillating frequencies that modifies the spectrum of the exciting optical signal as the energy is transferred to the SPW. This transfer of energy can be generated only at a specific resonance wavelength of light for which the momentum of the photon matches that of the plasmon [12].

Looking at the phenomenon from another point of view – the quantistic or particle description – this means that the photons of proper energy coupling with electrons of the metal surface create another wave, the particle of which is called the Surface Plasmon Polariton (SPP). Since SP waves are tightly bound to metal–dielectric interfaces penetrating around 10 nm into the metal (the so-called skin depth) and typically more than 100 nm into the dielectric (depending on the wavelength), they concentrate EM waves in a region that is considerably smaller than their wavelength [13, 14].

The frequency or wavelength for which the curve takes its minimum value is what it is called the surface plasmon resonance condition. SPR is responsible for a

dip in reflectance at the specific wavelength, the dip resulting from the absorption of optical energy in the metal.

There are two main types of surface plasmons (SPs) with respect to their propagation characteristics along the interface: extended or propagating and localized. The propagating SP is considered more classical since it has been known for a longer time. However, the latest advancements in nanotechnology have made the fabrication of structures with nm-scale features feasible, thus the localized SPR has become a subject of interest during the last two decades. Localized SPs are excited in metallic structures with lateral dimensions less than half the wavelength of the exciting EM wave [15].

A third type of plasmons may be mentioned called long-range SPR (LRSPR), which exists in thin metal films or stripes characterized by low attenuation and traveling along the surface for distances up to a few mm in the visible or even a few cm in the infrared. This latter type might have applications in active photonic components and highly sensitive sensors.

In the case of propagating SPR (PSPR), plasmons propagate along the interface between metal and dielectric, for distances of the order of no more than hundreds of microns and decay evanescently in the z direction (perpendicular to the interface) with decay length of the order of half the wavelength ($\approx 200\,\text{nm}$ for wavelengths in the visible range).

The interaction between the metal and dielectric surfaces can be observed in three ways: (a) angle, (b) wavelength shift, and (c) imaging. In the first two, the reflectivity of light from the metal surface as a function of either wavelength (at constant incidence angle) or as a function of incidence angle (at constant wavelength) is measured. The third mode uses light of both constant wavelength and incidence angle to interrogate a two-dimensional region of the sample, mapping the reflectivity of the sample as a function of position. In each of these modes one can measure intensity, phase or polarization change [16].

Despite the possible quantistic approach, the theoretical background of the topic can be covered by solving Maxwell's equations at the interface between a metal and dielectric, taking into account the proper boundary conditions. For the light to couple some energy towards the surface plasma wave, matching conditions both in terms of energy and momentum must be fulfilled. For the plasma wave to exist, the dielectric

constants of the materials at the interface must fulfill the following conditions [17]:

$$\begin{aligned} \varepsilon_{\mathrm{m}}(\omega) \cdot \varepsilon_{\mathrm{d}}(\omega) < 0 \\ \varepsilon_{\mathrm{m}}(\omega) + \varepsilon_{\mathrm{d}}(\omega) < 0 \end{aligned} \tag{3.1}$$

where ε_{m} stands for the dielectric constant of the metal and ε_{d} for the dielectric constant of the dielectric material. The wave vector (propagation constant) of a SPW at the interface of a metal and a dielectric, expressed as the left hand side of Eq. 3.2, is always larger than the wave-vector (propagation constant) of a light beam traveling in the dielectric, expressed as in the right hand side of Eq. 3.2 [18]:

$$k_{\mathrm{SP}}(\omega) = \frac{\omega}{c}\sqrt{\frac{\varepsilon_{\mathrm{m}}(\omega) \cdot \varepsilon_{\mathrm{d}}(\omega)}{\varepsilon_{\mathrm{m}}(\omega) + \varepsilon_{\mathrm{d}}(\omega)}} > k_{\mathrm{light}}(\omega) = \frac{\omega}{c}\sqrt{\varepsilon_{\mathrm{d}}(\omega)} \tag{3.2}$$

This equation implies that the light propagating in a dielectric is not energetic enough to generate a plasmon wave at the interface of that dielectric with a metal. However, this limitation can be overcome if light propagates through a higher refractive index medium but generates the plasma wave on a metal interface with a lower RI medium (which constitutes the analyte, the material to be sensed). This leads to the well-known Kretschmann and Otto configurations for prism-based SPR sensors, as pictured in Fig. 3.1 [19, 20]. This requirement can be better illustrated considering the dispersion curves for a water SPR sensor as in Fig. 3.2. The graph clearly shows that the SPW dispersion (pink line) never intersects the light propagating in water (green line) and that the excitation of the SPW is possible only by light that propagates in a glass substrate (blue line) characterized by a higher RI value. For example, considering the case of a glass – metal (Au) – water system the wavelength intersection for which the SPR occurs is around 615 nm.

The SPW exponentially decays in the transverse direction both in the metal and in the lower RI dielectric. Another important fact to be remarked is that it propagates parallel to the interface, making it a p-polarized (parallel, transverse magnetic, or TM-polarized) wave; therefore, in order to satisfy the continuity at the boundaries, the light wave that excites such a wave must be p-polarized too.

This aspect is very important to maximize the SPW excitation in prism-based sensors since for those configurations it is possible to control the polarization of the incident light used for the interrogation. On the contrary, in standard cylindri-

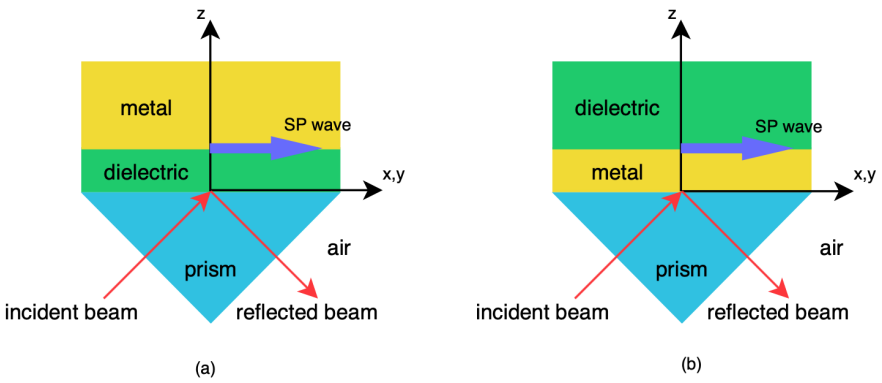

Fig. 3.1 Prism based configurations. (a) Otto configuration (b) Kretschmann configuration.

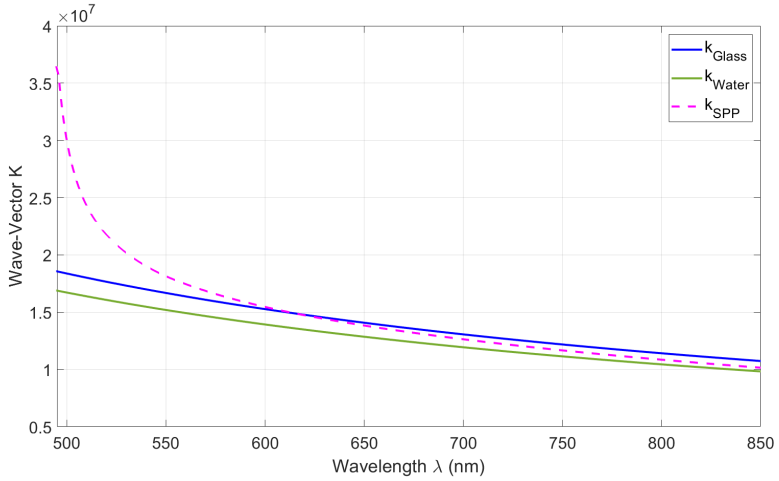

Fig. 3.2 Dispersion curves for a water SPR sensor.

cally shaped optical fiber, the mode polarization overlap prevents any control on the polarization of incident light. Therefore, despite this can be mitigated with properly designed fibers (e.g., D-shaped fibers), in OFSPR applications the contrast of the SPR spectral curves is reduced with respect to the corresponding prism-based configurations.

Another important parameter impacting the excitation of the SPW when it comes to Kretschmann-like configurations is the thickness of the metal layer. Indeed, this has to be thicker than the penetration depth of light, in order for the field to have a

non-negligible interaction with the lower RI material on the other side of the metal, otherwise the metal layer would act as a “perfect” mirror. For this configuration the thickness of the lower RI dielectric (i.e., the analyte) is irrelevant. On the contrary, for the Otto configuration, is the metal layer thickness that is irrelevant (Fig. 3.1(a)).

OFSPR based sensors are all Kretschmann-like systems in which the metal layer is deposited for a certain length onto the fiber, having totally or partially removed the cladding to allow a strong enough interaction with the guided field (Fig. 3.3). Typically, the metal has a thickness of few tens of nanometers. Most common metal is gold (Au) for its chemical inertness, although in practice the metal layer is actually made by a stack of different metals, going from one or more adhesion layers in contact with the glass (usually titanium/chromium) to a gold layer in contact with the analyte.

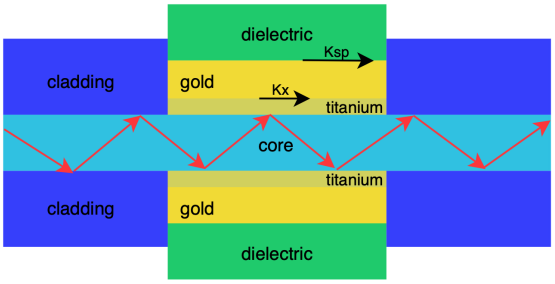

Fig. 3.3 Basic structure (not in scale) of a OFSPR sensor.

SPR phenomenon has been regarded as a powerful sensing approach due to the high sensitivity of the detection of the analyte’s RI. As the field decays exponentially in the medium under test, the sensor is sensitive only to the variations in the very proximity of the metal layer, thus creating a big potential for molecular and biomedical sensing. The sensor described so far is sensitive to variations in the RI, regardless of their origin. However, it can be made selective to specific species by proper functionalization of the metal surface [21, 22].

Propagating SP waves are excited with TM-polarized EM waves when the component of the k-vector along the metal–dielectric interface matches the SP k-vector. The condition of TM polarization is needed to generate the charge distribution on the metal–dielectric interface. In the mentioned case the electric field has a component perpendicular to the interface. The SP phenomenon can easily be understood, and

its main characteristics can be determined by solving Maxwell's equation to the boundary-value problem. We start our discussion by considering SPs on the interface of semi-infinite metal and dielectric then the effect of the finite thickness of the metal film will be considered.

When the conditions for the excitation of a SPW are met (i.e., the SPR occurs), the spectrum exhibits a notch-like behavior with a dip that red-shifts or blue-shifts depending on the analyte RI increment or decrement (Fig. 3.4). The SPR wavelength is found either in the visible range or the near infrared for most of the metals of interest. The sensitivity of the sensor with respect to RI changes is not linear, even though quite often it is linearized to give a single mean value expressed in nm/RIU, where RIU stands for Refractive Index Unit, pseudo unit of measurement since the refractive index is a dimensionless quantity. For the visible range measurements, the sensitivity for the same RI change is higher for higher RI (thus on the rightmost extreme of the spectrum). This depends on the dispersive nature of the dielectric constant of the metals used. In practical applications, the shift in the resonance wavelength is typically evaluated by fitting the measured curve with the theoretical curve or with a polynomial approximation to lower the impact of noise and thus improve the resolution.

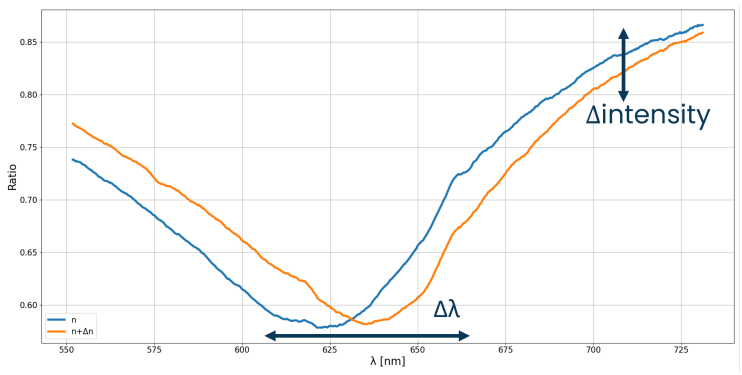

Fig. 3.4 Intensity and wavelength interrogation methods.

The response of an SPR sensor is evaluated by spectral analysis and detection of the SPR dip. This can be performed by means of a spectrometer in combination with either a broadband or a tunable narrowband light source. A simplified intensity-based interrogation technique can be implemented by exploiting a fixed wavelength laser (or even an LED) with emission on one of the shoulders of the SPR curve and replacing the spectrometer with a simple photodiode [23, 24]. As shown in Fig. 3.4,

this configuration converts changes in the analyte RI into changes of the received intensity. Clearly, this approach is more sensitive to noise than the previous technique; however, it is preferred for real-time monitoring as measuring the intensity requires far less elaboration compared to the acquisition of the entire spectrum. Depositing a suitable uniform metal layer on a fiber is not an easy task due to the round shape of the fiber. Moreover, different combinations of core/cladding diameter and numerical aperture will impact the performance of the sensor. Some considerations on these aspects will be reported in Sec. 4.1.

Another choice in designing OFSPR based sensors is how to maximize the interaction between the light field and the metal layer. Indeed, standard telecommunication fibers are characterized by a thick cladding, so the field becomes negligible well before it can reach the cladding-coating interface. To overcome this problem, some researchers have chosen to use Multi-Mode Fibers (MMFs) with a large core (200 µm or more) made of glass, surrounded by polymeric cladding. A plastic cladding simplifies its removal in the sensing section, as it can be done by means of chemical (usually acetone) and/or mechanical stripping. For example, aiming at widely deployable low-cost sensors, this has been the choice made during this work: 200 , 400 or 600 µm silica core/plastic cladding fibers were used. See Appendix A for further details.

3.1 Performance Parameters

The performance of the sensors is usually presented in terms of sensitivity, Detection Accuracy (DA) and Figure of Merit (FoM), which should be as high as possible [25]. A list of commonly used parameters to compare different optical fiber sensors is reported below [26, 27].

Sensitivity is defined as the resonance wavelength ($\delta\lambda_{res}$) variation due a unit change in the analyte refractive index (δn_d) as shown in Eq. 3.3:

$$S = \frac{\delta\lambda_{res}}{\delta n_d}\left(\frac{nm}{RIU}\right) \tag{3.3}$$

where RIU stands for Refractive Index Unit.

By fixing the wavelength, the sensitivity can be also expressed as the change in the transmittance (δT) due a refractive index variation (δn_d) as reported in Eq. 3.4:

$$S_\lambda = \left(\frac{\delta T}{\delta n_d}\right)_\lambda \left(\frac{1}{RIU}\right) \tag{3.4}$$

Accuracy is the degree of correspondence between the measured value of the measurand and its real value (i.e., refractive index or analyte concentration).

Detection Accuracy (DA) represents the accuracy with which the optical fiber sensor can measure the resonance wavelength (λ_{res}), and thus the refractive index of the analyte. The value should be as high as possible. Higher values are obtained if the width of the SPR curves is narrower. Indeed DA is defined as (Eq. 3.3):

$$DA = \frac{H}{FWHM} \tag{3.5}$$

where H is the dip height, and $FWHM$ the Full Width at Half Maximum.

Figure of Merit (FoM) is another important parameter, whose values are high in case of high performance sensors. It is obtained as (Eq. 3.6):

$$FoM = \frac{S}{FWHM} \tag{3.6}$$

whit S being the sensitivity (Eq. 3.3) and $FWHM$ the Full Width at Half Maximum.

Limit of Detection (LoD) indicates the minimum concentration of the analyte that can be detected with reasonable certainly by the sensor according with its spectral resolution. The smallest amount that can be detected is imposed by the resolution of the spectrometer, since it sets the minimal shift in the resonance wavelength that can be appreciated. It is possible to obtain the LoD from Eq. 3.7:

$$\text{LoD} = \frac{\Delta\lambda}{S_{c_{\min}}} \tag{3.7}$$

where $S_{c_{\min}}$ indicates the sensitivity evaluated in presence of the minimum/zero amount of the analyte. Since the LoD is an ideal parameter that does not take into account the noise and fluctuations that can affect the measurement, if the noise is greater than the spectrometer resolution it is convenient to introduce the LoQ.

Limit of Quantification (LoQ) takes into consideration the standard deviation of the resonance wavelength res calculated in the near zero analyte concentration in order to determine the performance of the sensor. It can be computed as Eq. 3.8:

$$\mathrm{LoQ} = \frac{\sigma\lambda_{res}}{S_{c_{\min}}} \tag{3.8}$$

Chapter 4

SPR - Simulation

This section addresses the main design parameters of the OFSPR sensor and analyzes how these parameters affect the overall sensing performance. The simulations are carried out with the aim of identifying, given the available materials, the most suitable geometrical configuration capable of delivering the required performance.

The modeling procedure consists of multiple steps. It begins with a numerical simulation (as described in the following sections), followed by a Support Vector Machine (SVM) prediction based on the dataset obtained with the numerical simulation to accelerate the computation of further stages. Finally, a Genetic Algorithm (GA) is employed to optimize the design parameters and to identify the best configuration among all possible geometries.

Given the large number of combinations, Multi-Objective Optimization Algorithms (MOOA) can be used to explore the design space and identify optimal configurations. However, evaluating each configuration through the numerical simulation is computationally expensive, often requiring numerous iterations before achieving satisfactory performance. This is translating in a process that requires many hours to find viable solutions.

In most cases, the choice of parameters is constrained by commercially available components and by practical fabrication limitations. For example, the only optical fibers available at the time of simulation and subsequent fabrication were Thorlabs fibers with core diameters of 200 µm, 400 µm, and 600 µm, all featuring TECS (Technology Enhanced Clad Silica) cladding.

4.1 SPR - Simulation with COMSOL Multiphysics®

The resonance frequency at which surface plasmons are excited depends primarily on the type and thickness of the metal film and on the refractive index of the surrounding medium. Optical fiber SPR probes represent one of the most miniaturized forms of SPR devices and are particularly attractive for chemical and biological sensing, particularly in difficult to access locations exploiting their small size, mechanical flexibility, and ability to transmit optical signals over long distances.

This chapter focuses on the design simulations of OFSPR sensors performed using a commercial Finite Element Method (FEM) software, namely COMSOL Multiphysics®.

In this section, the optical behavior is analyzed using physical optics, adopting a FEM approach. This method is particularly suitable for small-core fibers, where the fiber dimensions are comparable to the wavelength, and the assumptions of geometrical optics are no longer valid. In the following chapters, the analysis will instead be carried out using geometrical optics through ray tracing simulations, which provide a more efficient description for multimode fibers, where a full-wave analysis would be computationally impractical.

FEM simulations were carried out to investigate and optimize the RI sensing performance within the constraints of the experimental setup. In this section, a conventional single-mode fiber (SMF-28) made of pure silica is considered. Owing to its small core size, this fiber falls within the regime where physical optics must be applied, as the core dimensions are comparable to the optical wavelength and geometrical optics assumptions are no longer valid. This fiber has a core diameter of 8.2 µm, a cladding diameter of 125 ± 0.7 µm, and a coating diameter of 245 ± 5 µm. In the COMSOL Multiphysics® model, the cladding was replaced with a combination of two layers, 20 nm titanium adhesion layer in contact with the core followed by a gold layer with thickness varying from 45 to 60 nm.

First, a fiber in air was modeled. Subsequently, the analyte region was filled with different liquids, and the corresponding sensing performance was calculated.

Fig. 4.1 show the cross-section and the overall geometry of the proposed sensor. The refractive index of the silica core (n_s) was derived as a function of wavelength

using the Sellmeier dispersion equation (Eq. 4.1), where the coefficients were taken from the literature [28].

$$n_s = \left(1 + \frac{a_1\lambda^2}{\lambda^2 - b_1^2} + \frac{a_2\lambda^2}{\lambda^2 - b_2^2} + \frac{a_3\lambda^2}{\lambda^2 - b_3^2}\right)^{\frac{1}{2}} \tag{4.1}$$

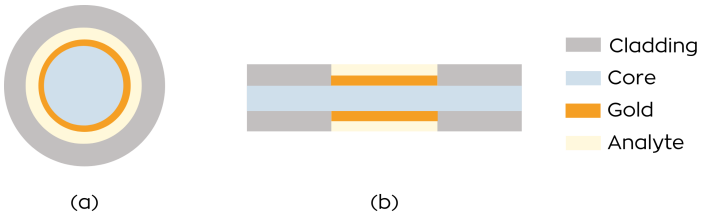

Fig. 4.1 Schematic illustration of the simulated structure. (a) Cross section, (b) Geometry.

The numerical analysis was carried out using the Wave Optics module in COMSOL Multiphysics®. The structure was discretized into a fine mesh and surrounded by a Perfectly Matched Mayer (PML) to absorb any light propagating towards the boundary.

The parameters to simulate the proposed sensor were defined in COMSOL Multiphysics® and some are shown in Tab. 4.1.

Parameter	**Value**		**Unit**	**Description**
d_{co}	8.2	$\times 10^{-6}$	m	Core diameter
d_{Au}	8.25	$\times 10^{-6}$	m	Gold diameter
d_{analyte}	1.125	$\times 10^{-5}$	m	Analyte layer diameter
PML	1.825	$\times 10^{-5}$	m	Perfectly Matched Layer (PML) boundary
λ_{op}	6.5	$\times 10^{-7}$	m	Operating wavelength
f_{op}	4.6122	$\times 10^{20}$	Hz	Operating frequency (c/λ_{op})
n_{s}	1.4565		–	Sellmeier equation result
n_{Au}	0.29364		–	Gold refractive index
n_{air}	1.00027632		–	Air refractive index

Table 4.1 Parameters used in the simulation model.

The sensor performance depends on the parameters of its structure. The key parameters of this simulation is the gold thickness. Fig. 4.2 shows the electric field distribution in the fundamental core mode. As the thickness decreases, the SPR dips

become wider but deeper (Fig. 4.3), which results in higher sensitivity with a lower signal-to-noise ratio. The SPW can no longer be efficiently stimulated when the metal thickness is too large due to the significant absorption of the metal. As the RI of the analyte layer changes, the effective RI (n_{eff}) also changes.

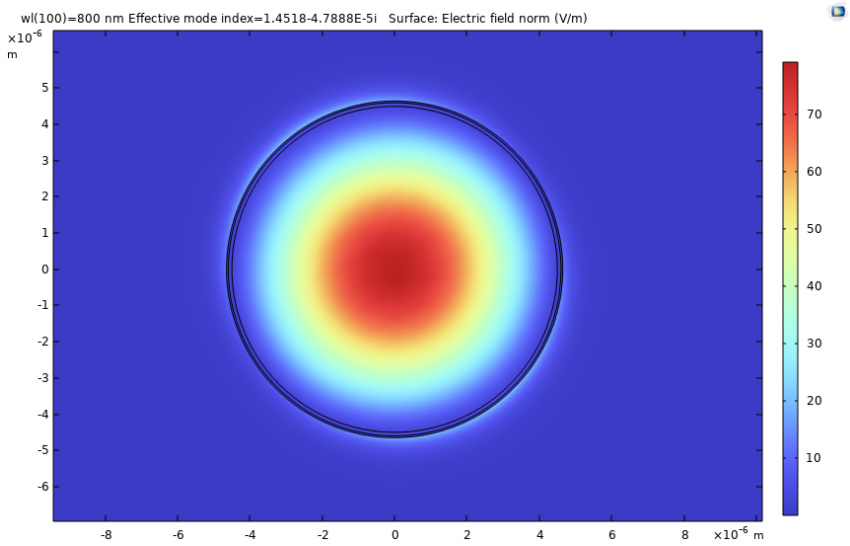

Fig. 4.2 Electric field distribution of the fundamental mode for a gold thickness of 50 nm.

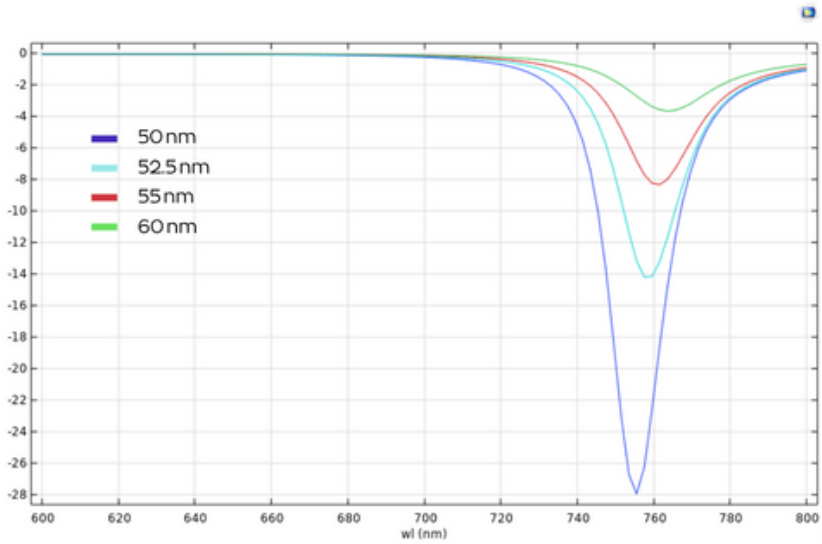

Fig. 4.3 SPR dips for a gold thickness of 50 nm, 52.5 nm, 55 nm and 60 nm

4.2 Numerical Simulation with MATLAB®

This section will focus on the numerical simulations of the OFSPR sensors in MATLAB®, discussing the assumptions taken in consideration to simplify the simulation process and it continues with the choice of the design parameters and their impact on the sensing performance according to some quality standard parameters. This part can be considered also as a continuation of Chapter 3, as it covers the mathematical model of the sensor, and the reader can understand in a more explicit way how the design parameters have direct impact on the final result. The chapter starts with the main aspects of the mathematical and physical model, discussing the assumptions taken in consideration to simplify the simulation process. The refractive indices of the materials involved in the simulations, considering the wavelength dependency (dispersion) are taken from https://refractiveindex.info/

As seen earlier in Chapter 3, the SPR phenomenon consists of the excitation of a SPW at the interface between a metal (gold) and a low RI dielectric (water) from light coming from a higher RI dielectric (glass). Thus, to start creating the first physical model for an SPR structure, one should imagine a three layer structure, where a thin metal layer is sandwiched between a substrate of glass in one side and water one the other side.

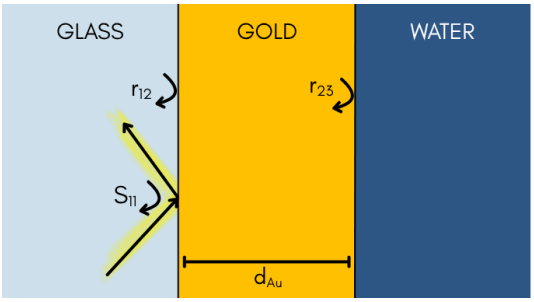

Fig. 4.4 Schematic illustration of the simulated three layered structure.

Fig. 4.4 schematically illustrates the three layer structure. For simulation purposes the glass and water layers can be considered semi-infinite, thus their thickness is irrelevant, while the thickness of the metal layer plays a very important role as it will be seen. The light beam is incident from the glass and at the glass-metal interface is partially reflected and partially absorbed to excite the SPW.

The equation that describes the light reflection on a three layered (slab) structure is written below in Eq. 4.2:

$$S_{11} = \frac{r_{12} + r_{23} \cdot e^{-j \cdot k_{z2} \cdot d_{Au}}}{1 + r_{12} + r_{23} \cdot e^{-j \cdot k_{z2} \cdot d_{Au}}} \tag{4.2}$$

where r_{12} and r_{23} are the elementary Fresnel coefficients calculated as in Eq. 4.3; k_{z2} is the wave vector in the direction of propagation z (horizontal axis in the figure) in metal, medium 2, and d_{Au} the corresponding thickness.

$$\begin{aligned} r^{\mathrm{s}}_{l,l+1} &= \frac{Z^{\mathrm{s}}_{l+1} - Z^{\mathrm{s}}_{l}}{Z^{\mathrm{s}}_{l+1} + Z^{\mathrm{s}}_{l}} \qquad \text{for } s-\text{polarization} \\ r^{\mathrm{p}}_{l,l+1} &= \frac{Z^{\mathrm{p}}_{l+1} - Z^{\mathrm{p}}_{l}}{Z^{\mathrm{p}}_{l+1} + Z^{\mathrm{p}}_{l}} \qquad \text{for } p-\text{polarization} \end{aligned} \tag{4.3}$$

where l indicates the layer number and Z is the characteristic impedance of the respective materials, which depends on the wavelength, polarization and angle of the incidence and the refractive index of the material.

As mentioned also in the previous chapter (Ch. 3), usually between the glass substrate and the gold layer, a few nanometers of titanium (Ti) or chromium (Cr) are deposited to enhance the adherence. Therefore, in order to have the simulation as close as possible to the experimental reality, it is necessary to consider also this auxiliary layer in the calculations. When extending the structure from three to four

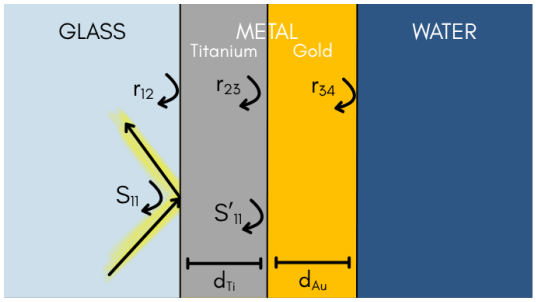

Fig. 4.5 Schematic illustration of the simulated four layered structure.

(or more) layers, the same set of calculations is repeated iteratively. The procedure proceeds from right to left: the previously obtained S_{11} now refers only to the three rightmost layers of the structure, and is therefore denoted as S'_{11} , as expressed in

Eq. 4.4.

$$S'_{11} = \frac{r_{23} + r_{34} \cdot e^{-j \cdot k_{z3} \cdot d_{Au}}}{1 + r_{23} + r_{34} \cdot e^{-j \cdot k_{z3} \cdot d_{Au}}} \tag{4.4}$$

The term S'_{11} can now be regarded as the secondary elementary reflection coefficient of a three-layered structure, and it can be substituted into the same expression leading to Eq. 4.5.

$$S_{11} = \frac{r_{12} \cdot S'_{11} \cdot e^{-j \cdot k_{z2} \cdot d_{Ti}}}{1 + r_{12} \cdot S'_{11} \cdot e^{-j \cdot k_{z2} \cdot d_{Ti}}} \tag{4.5}$$

Fig. 4.5 schematically illustrates the four-layer configuration, which includes the Ti layer.

This procedure is standard for any multilayered structure; what makes the present case distinctive are the specific materials used and their order within the stack. The thickness of the metallic layer should not exceed 100 nm, ideally ranging between 50 nm and 70 nm. This range is supported both by our simulations and by experimental results reported in the literature [29]. For thicknesses below 50 nm, the metal layer is insufficiently reflective, whereas for thicknesses above 100 nm, the value approaches the metal's maximum penetration depth, resulting in only a small fraction of light reaching the second interface. It is worth noting, however, that these values are specific to gold and are expected to vary for different materials.

The simulations are meant to get as close as possible to the experimental reality by considering as many details as possible, in order to be valid representatives of the experimental work. A very important detail of the fiber multi layered structure present in reality but not considered in the simulation is the cylindrical shape of the fiber. In practice, these simulations consider only the meridional rays (those passing through the center of the fiber), neglecting the presence of the skew rays propagating in the fiber, implicitly assuming that their behavior is very similar to the others. Another assumption considered in the simulation is the flatness of the surfaces and the uniform thickness of the metal layers. However, in the actual sensors the thickness of the metal layer is not uniform, as we deposit the metal layer only on two symmetrical sides of the fiber, not continuously rotating it. This means that the thickness of the gold layer varies from 0 to 50 nm in an elliptic shape (Fig. 4.6). More details on the sensor preparation and on the metal deposition process can be found in Appendix A.

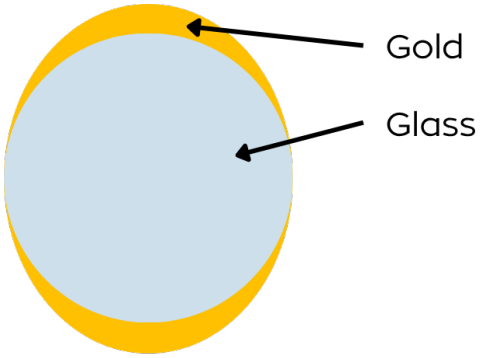

Fig. 4.6 Schematic illustration of the non uniform deposited metal layers (out of scale) that varies from 50 to 0 nm.

After analyzing the physical and the mathematical approach of the SPR fiber structure, we can now move to the simulation of the light source and of the power distribution within the fiber. In practice, to observe the SPR curve in wavelength interrogation we use a white LED with an almost flat spectrum in the 470 nm to 850 nm range. However, the measurements are always taken with respect to a reference, thus the spectrum can be considered perfectly flat and normalized. Thus, in the simulation we can easily consider a light source with a flat spectrum. However, LEDs have a Lambertian shape power distribution with respect to the launching angles, which means different launching angles carry different power densities. Moreover, the optical power generated by the LED does not couple totally into the fiber as it is limited by the fiber numerical aperture, which determines the acceptance cone.

The coupled portion propagates along the fiber with normal distribution, meaning that the central rays carry more power within the fiber compared to the peripheral ones. The coupled power portion in the fiber is described by the following Eq. 4.6 [30–32].

$$P_{\text{in}}(\theta_{\text{critical}})d\theta_{\text{critical}} \propto \left(\tan(\theta_{\text{critical}})/\cos^2(\theta_{\text{critical}})\right) d\theta_{\text{in}} \tag{4.6}$$

and the power distribution with respect to each angle due to the Lambertian power distribution of the source can be expressed as in Eq. 4.7:

$$P(\theta) \propto n_{\text{core}}^2 \sin(\theta)\cos(\theta) \tag{4.7}$$

Depending on the sensitive length and on the core diameter, another parameter that plays an important role is the number of reflections for each of the angles in which light is propagating. The number of reflection within the sensitive length can be expressed as in Eq. 4.8:

$$N_{\text{refl}} = \frac{L}{d\tan(\theta_{cm})} \tag{4.8}$$

where θ_{cm} is the angle in the core-metal interface. It has to be considered that only the p-polarized light (TM polarization) contributes to the SP excitation, thus considering a non-polarized light with 50% of its power being s-polarized, only the 50% portion of the p-polarized light will be affected by the phenomenon [33, 34]. The final equation of the power transmitted can be written as expressed in Eq. 4.9:

$$P = P_{\text{distrib}} \cdot (W_{\text{s}} \cdot R_{\text{s}}^{N_{\text{refl}}} + W_{\text{p}} \cdot R_{\text{p}}^{N_{\text{refl}}}) \tag{4.9}$$

where $W_{\text{s,p}}$ is the weight of each polarization, respectively (50% in case of nonpolarized light); $R_{\text{s,p}}$ is the reflectivity calculated as mentioned in Eq. 4.5; P_{distrib} is the coupled power distribution calculated from Eq. 4.6 and in Eq. 4.7; N_{refl} is the number of reflections within the sensitive area calculated from Eq. 4.8.

Last but not least, to be remarked is also the fact that both in practice but also replicated in the simulations, the SPR curve plotted in the graphs in this dissertation (but also in the literature) is not the raw spectrum. Actually a reference needs to be taken when the sensor is exposed in air. Thus what we call SPR curve is actually the effect of the SPR phenomenon in water divided by the effect of the SPR phenomenon in air.

In the simulations, the titanium adhesion layer thickness is varied between 10 nm and 30 nm, while the gold layer thickness ranges from 30 nm to 60 nm, using a step of 5 nm. We have selected to simulate lengths in the 1 cm to 4 cm with 1 cm step. The maximum length has been limited to 4 cm, to keep the dimension of the sensor handy and guarantee robustness.

Tab. 4.2 shows all the variables with their respective intervals and the number of total combinations that can be achieved which is 3360. The MATLAB® program is executed for each of the geometrical combinations generated and the output parameters are stored.

Variable	Value	Unit	Description
n_{layers}	5	–	Number of layers
th_{Ti}	10 : 5 : 30	nm	Titanium layer thickness
th_{Au}	30 : 5 : 60	nm	Gold layer thickness
th_{SiO_2}	`eps:5:15+eps`	nm	Silica layer thickness
d_{core}	$[200, 400, 600]$	µm	Core diameter
l_{sens}	0.01 : 0.01 : 0.04	m	Sensitive length

Table 4.2 Geometry Parameters.

The combination of possible geometries and their respective output parameters are stored into a dataset in order to be used to train the SVR model.

4.3 SVR (Support Vector Machine)

Support Vector Regression (SVR) [35] is a type of Support Vector Machine (SVM) [36] algorithms and is commonly used for regression analysis. Classical SVM aims to identify the optimal hyperplane that separates the data into two classes with the maximum possible margin. The margin is defined as the distance between the hyperplane (a flat subspace of dimension p-1 in a p-dimensional space, where p is the number of input features) and the closest data points of each class, known as support vectors. Maximizing this margin enhances the generalization capability of the classifier. In analogy with SVM, SVR employs the concepts of hyperplane and support vectors, but modifies their definitions for regression purposes. Instead of separating data points belonging to different classes, SVR attempts to find a regression function $f(x)$ that lies within a specified tolerance band around the target values. This tolerance band, the ε-insensitive tube, is the margin in the regression context. This tube allows some deviation of the data points from the hyperplane without being counted as errors. The hyperplane is the best fit possible to the data that fall within the ε-insensitive tube. The objective of SVR is therefore to find a function that accurately predicts the target variable while simultaneously keeping the complexity of the model as low as possible in order to avoid overfitting. SVR can be mathematically formulated as a convex optimization problem. In practice this translates into finding the flattest function $f(x)$ that deviates from the training targets by at most ε. Flatness of the function implies that it is less sensitive to small

changes in the input data, which reduces the risk of overfitting. For a linear case, flatness corresponds to minimizing the norm of the weight vector w in the expression $f(x) = \langle w, x \rangle + b$.

When it is not possible to fit all training samples within the ε-insensitive tube, slack variables (ξ_i and ξ_i^*) are introduced to quantify the deviation of those points that lie outside the tube. To balance the trade-off between model complexity (i.e., flatness of $f(x)$) and the magnitude of deviations beyond ε, a regularization parameter $C > 0$ is introduced. The parameter C penalizes large deviations and thus controls the tolerance for prediction errors.

SVR assigns zero loss to data points falling inside the ε-insensitive tube, while penalizing deviations outside the tube proportionally to their corresponding slack variable ξ. This makes SVR more robust compared to traditional regression models, especially when dealing with noisy data.

Another important feature of SVR is its ability to handle nonlinear regression problems through the use of kernel functions. In cases where a linear regression is not sufficient to describe the underlying relationship, kernel functions implicitly map the input data into a higher-dimensional feature space, where a linear regression can be performed. Commonly used kernels include the linear, polynomial, radial basis function, and sigmoid kernels. By selecting an appropriate kernel, SVR can effectively capture highly nonlinear dependencies between the input and output variables.

4.3.1 Results

In MATLAB®, the SVR implementation was carried out taking advantage of the Statistics and Machine Learning Toolbox [37]. The first step consisted in arranging the input and output data from the numerical simulations into two matrices: a feature matrix X, containing the design parameters (fiber core diameter, Ti and Au thicknesses, etc.), and a target vector Y, containing the corresponding quality parameters obtained from the numerical simulation. Before training the model, the data were normalized using the *normalize()* function in order to have 0 mean value and unitary standard deviation to ensure that all variables had comparable ranges and to improve the convergence of the SVR algorithm.

The complete dataset was then split into a training set and a test set using *cvpartition()*, which enables the creation of reproducible partitions of the data for validation purposes (in this case, 80% of the data for training and 20% for testing).

The SVR model was trained using the *fitrsvm()* function, which provides a wide set of options to set the kernel function, the regularization parameter C, and the value of ε. In this work, the Gaussian kernel (also called Radial Basis Function, RBF) was used, setting the parameter *KernelFunction = 'gaussian'*. The values of C and ε were tuned empirically through a grid-search procedure by repeatedly calling *fitrsvm()* over a range of possible values and evaluating the error through cross-validation. The *crossval()* function was used to perform a 5-fold cross-validation on the training set and to determine the best hyper-parameters in terms of minimum Root Mean Square Error (RMSE).

At this point, the performances at test level are evaluated. In particular, Fig. 4.7 reports the real values of the three performance parameters plotted against the predicted values of the model. The red line is representing the regression line.

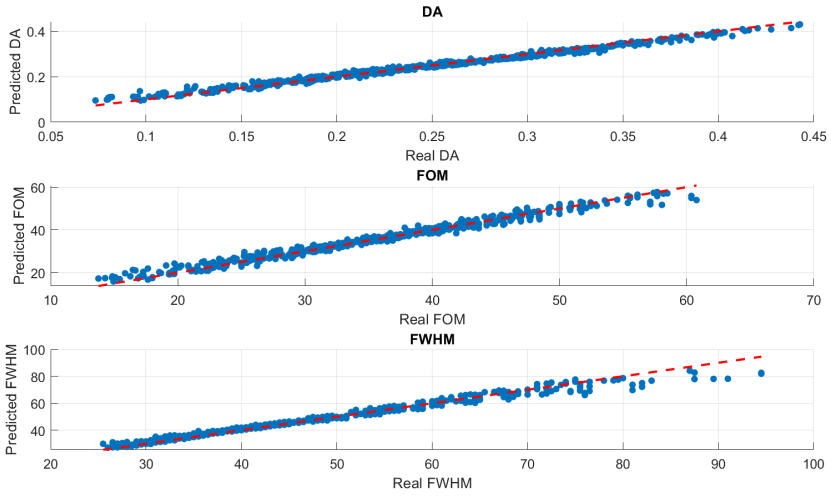

Fig. 4.7 Real values of the three performance parameters plotted against the predicted values of the model.

The points are well distributed along the line, meaning that the prediction are very close to the real values. The R^2 score is 0.9853, 0.9779 and 0.9768 respectively as the models are well able to exploit the variability of the test set. The total fit time is 0.256 seconds and the Mean Squared Error on the test set is 9.22×10^{-5} , 2.20

and 4.37 respectively. It is interesting to see also that the error associated with every prediction is quite low especially for the FWHM (Fig. 4.8). Once the SVR model has been properly trained the following multi-objective problem is implemented using it as evaluation model for each individual.

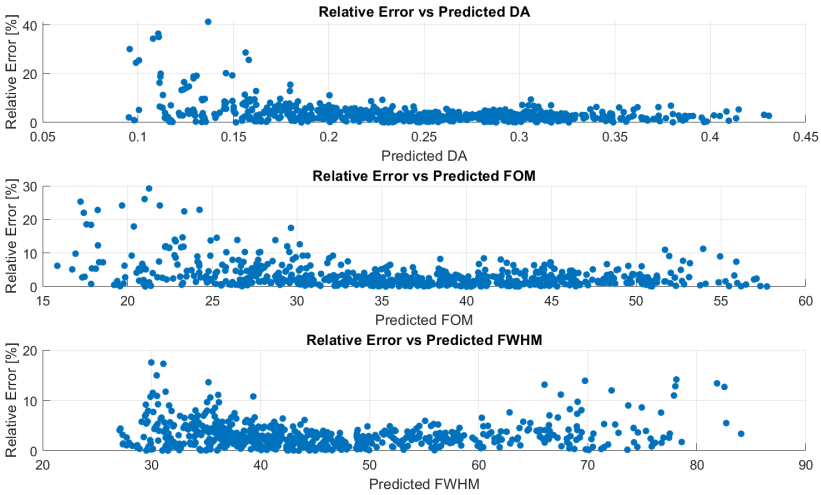

Fig. 4.8 Error associated with predictions.

4.4 GA (Genetic Algorithm)

Genetic Algorithms (GAs) are stochastic, population-based optimization methods inspired by the principles of natural selection and biological evolution. Unlike classical deterministic techniques that focus on a single solution, GAs maintain and evolve a population of candidate solutions, each representing a possible answer to the optimization problem [38].

At each generation, the individuals are evaluated using a fitness function, which quantifies how well they satisfy the problem objectives. Based on the fitness values, a subset of individuals is selected to act as parents, and new candidate solutions (offspring) are generated using crossover and mutation operators. Crossover combines genetic material (i.e., design variables) from two parents to explore potentially beneficial combinations, while mutation introduces random perturbations in order to preserve diversity and avoid premature convergence to local minima. By iteratively applying selection and genetic operators, the algorithm gradually improves the popu-

lation and converges toward highly fit solutions. Since GAs do not require gradient information and can work with non-differentiable, discontinuous, or highly nonlinear functions, they are widely used in engineering design and scientific optimization problems.

In practical applications, Genetic Algorithms can be efficiently implemented using MATLAB®, which provides the built-in function *ga()* (part of the Global Optimization Toolbox) [39, 40]. The user first defines the objective function, specifies the number of decision variables and optionally configures the algorithm's parameters such as population size, crossover rate, mutation rate and termination criteria. For more control over the evolutionary process, MATLAB® allows the use of custom selection, crossover and mutation functions. Real-time convergence plots (e.g., best fitness vs. generation) can also be displayed to monitor the algorithm and verify its convergence behavior.

4.4.1 Results

To determine the optimal geometry of the device, a multi-objective optimization procedure was carried out using a genetic algorithm. The previously trained SVR models (for DA, FOM and FWHM, see Sec. 3.1) were used as surrogate models within the optimization loop. In this way, instead of directly evaluating the physical system, which would be computationally expensive, the algorithm relies on the predictions provided by the SVR models to estimate the quality of each candidate solution.

Since the SVR models were trained on normalized data, the geometric parameters used during optimization were also normalized using the same mean and standard deviation, in order to ensure consistency between the data space and the search space. The multi-objective genetic algorithm was configured with an appropriate population size and Pareto fraction, in order to preserve the most promising solutions at each generation. During the evolutionary process, the candidate geometries are evaluated through the SVR models and progressively refined by applying selection, crossover and mutation operators.

At the end of the optimization, a set of Pareto-optimal solutions is obtained, representing the best possible compromise among the different performance indicators. The corresponding geometries are then denormalized, so that they can be

expressed in terms of real physical values and used in the practical application. Finally, a specific solution can be selected from the Pareto front according to the designer's preferences or by assigning a weight to each objective, depending on which performance indicator is considered more relevant for the application.

It is now possible to introduce the implementation of the algorithm and the main parameters that have been used in this study. An initial population composed by 100 individuals is created, using random uniform distribution. Each individual is thus characterized by 6 features (the geometrical parameters) and 3 labels (the three quality parameters). Since the evaluation is based on the SVR, it is mandatory to be consistent with the dataset used during training. Therefore each features has to respect the upper bound and the lower bound of the dataset. Moreover, each geometrical variable has to be pre-processed to be normalized as done for the SVR training.

During the evolutionary loop, the algorithm iteratively improves the population by applying mutation, crossover and selection operators until the maximum number of generations is reached. The mutation operator introduces diversity into the population by perturbing selected individuals using a scaling factor. In this work, a fixed scaling factor equal to 0.75 is adopted in most cases to promote exploration of the design space, while a random value is used with a small probability (10%) to favor exploitation around promising regions. After mutation, the values of each feature are checked to ensure that they remain within the predefined bounds, guaranteeing that all individuals can still be correctly evaluated by the SVR surrogate models. The crossover phase combines information from a mutated individual and a current solution (target) in order to generate a new trial candidate. The degree of inheritance from the mutant is controlled by the crossover rate. A crossover rate of 0.3 has been selected, which encourages a more local search and therefore accelerates convergence while still allowing for enough variability in the population. Once mutation and crossover have generated a pool of new individuals, the selection operator is applied to restore the original population size. To preserve diversity and avoid premature convergence towards a single region, a crowding-distance criterion is used to prioritize solutions that are well distributed across the objective space. At the end of the evolution process, the algorithm returns the Pareto Front, which contains the non-dominated solutions that represent the best trade-off among the considered objectives. Each point of the Pareto Front corresponds to a specific geometrical configuration.

The simulation was performed three times to account for the fact that the fiber core must assume a specific value, whereas the MATLAB® implementation only allows the definition of a range rather than discrete values.

The normalized values of the design variables are converted back into their real (denormalized) values using the mean and standard deviation of the training set, so that the corresponding geometries can be directly used also for practical implementation.

Fig. 4.9 present (for each d_{core} value) the comparison between the Pareto front obtained from the SVR-based optimization (blue dots) and that obtained from the full numerical simulations performed with the denormalized geometrical parameters (orange dots). The two results show only slight differences, which are consistent with the error reported in Sec. 4.3.1 for the evaluation of the SVR performance. The fact that the SVR and the numerical simulations provide slightly different quality parameter values is not an issue, since the final assessment of the geometries is always carried out with the numerical model once the optimal candidates have been identified. Despite these small discrepancies, the use of SVR significantly enhances the efficiency of the GA optimization. This is because the evaluation of a single geometry with the numerical model requires approximately 14 seconds, whereas the same evaluation performed with the SVR model takes only 0.1076 seconds. Consequently, the surrogate model makes it possible to explore the design space much more extensively, thereby improving the quality of the optimization results.

The next Fig. 4.10 shows the different combinations of the parameters for the 6 best geometries selected for each d_{core}. The results show that the solutions tend to cluster around a limited set of values, indicating that the algorithm converges toward an optimal configuration. The most promising parameters are approximately 15 nm for the Ti thickness, 55 nm for the gold layer, and 10 nm for the SiO_2 layer, while the sensing length exhibits greater variability depending on the selected fiber.

Since the deposition of silica on the gold layer can be a challenging process, the case without the silica layer has also been evaluated in order to assess how its presence affects the overall performance. In Fig. 4.11 the comparison between the geometries in the case with and without the silica is reported. As it can be seen the main differences are again in the length of the sensing region. Fig. 4.12 reports the results of the Pareto front, where we can see that the absence of the silica

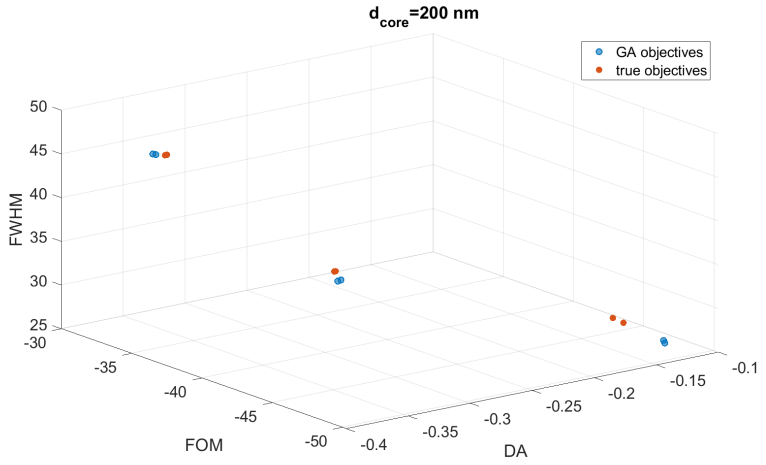

(a) Pareto front for $d_{core} = 200\,\text{nm}$

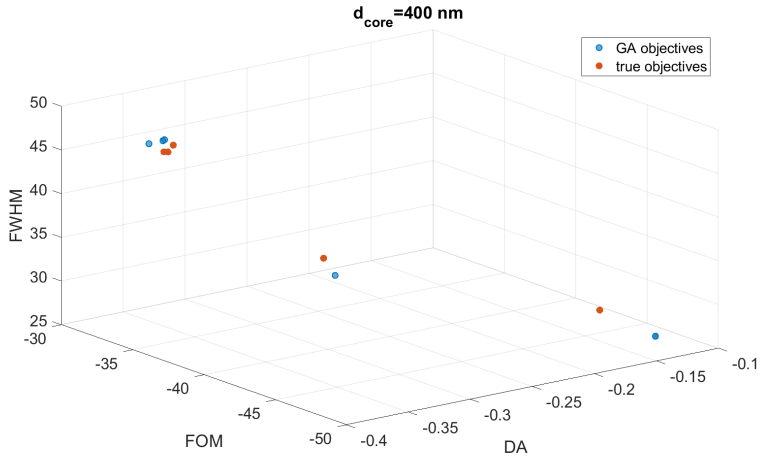

(b) Pareto front for $d_{core} = 400\,\text{nm}$

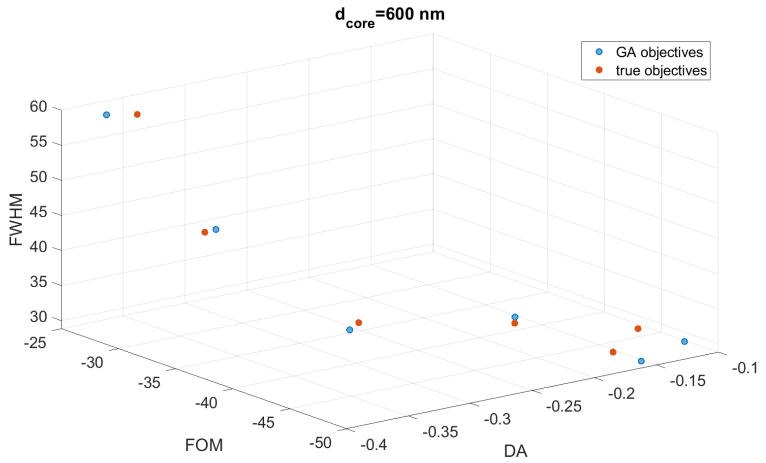

(c) Pareto front for $d_{core} = 600\,\text{nm}$

Fig. 4.9 Comparison between the Pareto front obtained from SVR-based optimization (blue dots) and from numerical simulations (orange dots).

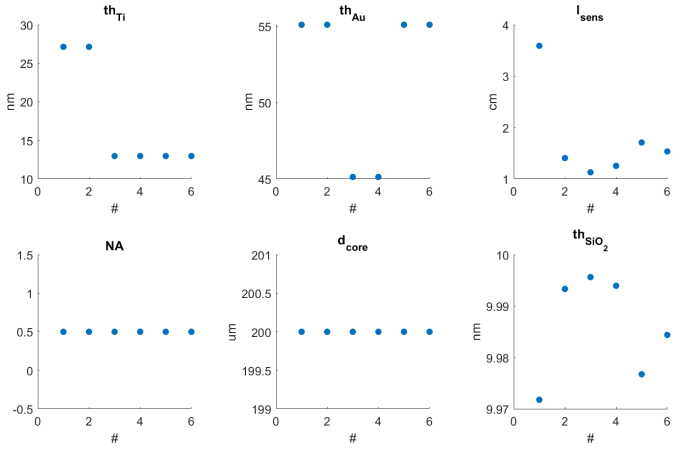

(a) Six optimal geometries for $d_{core} =$ 200 nm.

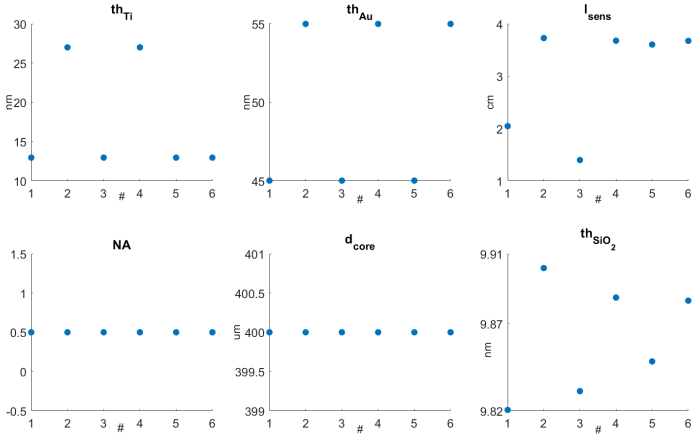

(b) Six optimal geometries for $d_{core} =$ 400 nm.

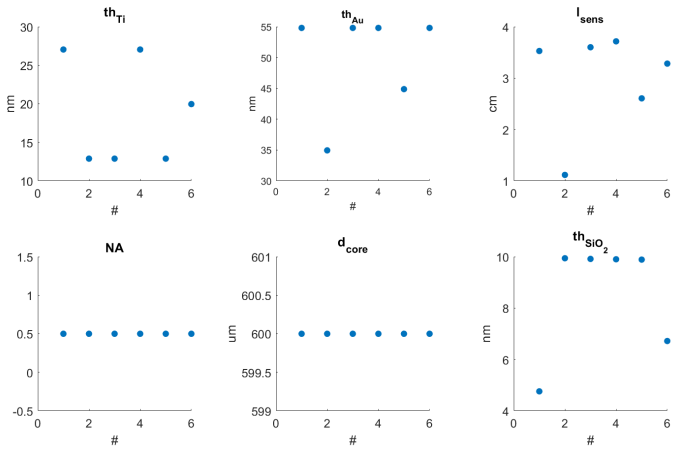

(c) Six optimal geometries for $d_{core} =$ 600 nm.

Fig. 4.10 Eighteen optimal geometries for $d_{core} =$ 200, 400 and 600 nm.

causes a slightly worst results in the quality parameters, as the FWHM (that must be minimized) changes from 40 to 55 compared to Fig. 4.9b.

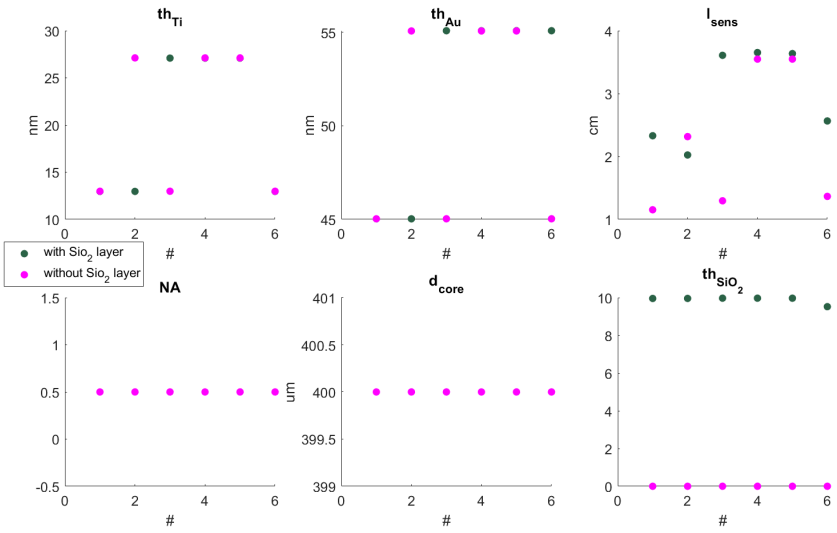

Fig. 4.11 Comparison between the geometries with (green dots) and without (pink dots) the SiO_2 layer.

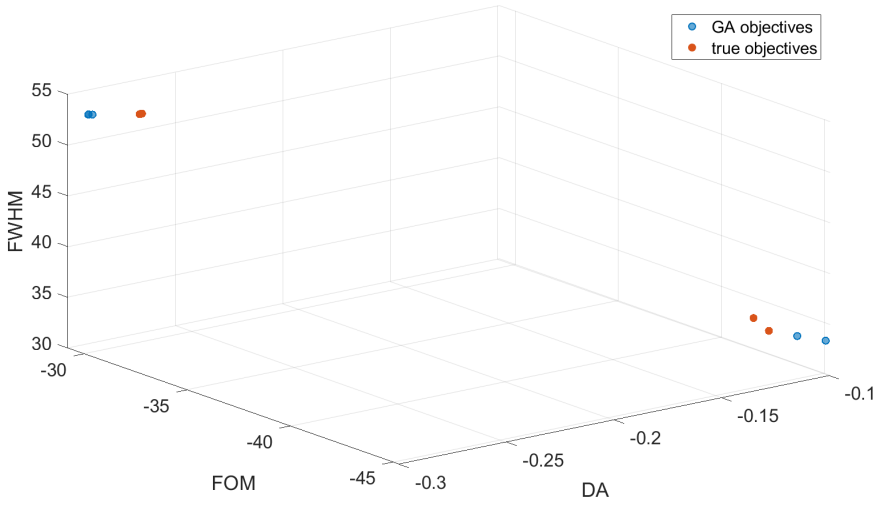

Fig. 4.12 Comparison between the Pareto front obtained from SVR-based optimization (blue dots) and from numerical simulations (orange dots) for $d_{core} = 400\,\text{nm}$, without the SiO_2 layer.

Tab. 4.3 presents an example of six possible geometries that can be selected for the device design. Fig. 4.13 reports the output obtained for those geometries

assuming an external RI of 1.34 (slightly higher than water). Since no uniquely optimal geometry can be defined, the choice depends on specific design requirements and technological constraints. In this work, the 4th configuration was selected as the most compatible with the available fabrication process among the proposed options.

Parameter	**Geometry**					
	#1	#2	#3	#4	#5	#6
th_{Ti} [nm]	12.979	12.979	27.128	12.979	12.979	27.128
th_{Au} [nm]	55.089	45.071	55.089	55.089	45.071	55.089
l_{sens} [m]	0.023	0.013	0.021	0.036	0.010	0.036
NA	0.50	0.50	0.50	0.50	0.50	0.50
d_{core} [µm]	400	400	400	400	400	400
th_{SiO_2} [nm]	0	0	0	0	0	0

Table 4.3 Six optimal geometries for $d_{core} = 400\,\text{nm}$.

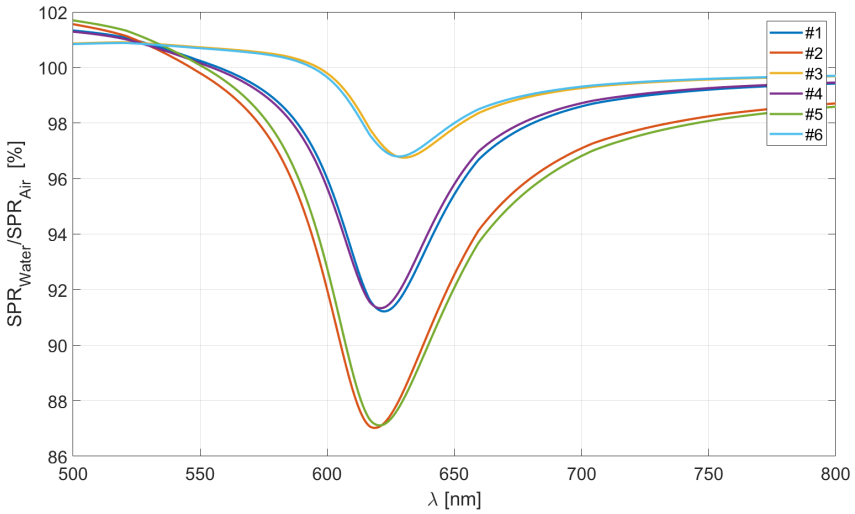

Fig. 4.13 SPR curves correspondent to the geometries reported in Tab. 4.3.

Chapter 5

SPR - Auto Calibration

Sensor calibration is a crucial step in the measurement process, as it directly influences the reliability, repeatability, and accuracy of the data collected. In its most general definition, calibration is the comparison of the output of a measurement device with a known reference standard, which is itself traceable to national or international standards. This procedure allows determining to what extent the sensor deviates from the true value of the physical quantity being measured and to define a mathematical relationship that compensates for these deviations.

Without proper calibration, even the most advanced sensor may provide data that are systematically biased, leading to incorrect conclusions in experimental studies, industrial processes, or monitoring applications. The calibration process typically begins with the identification of the environmental and operational conditions under which the sensor will be tested, since factors such as temperature, humidity, and electromagnetic interference can strongly influence its response. Next, a set of reference points is established by exposing the sensor to controlled stimuli whose values are precisely known. By recording the output signal of the sensor at each of these reference points, it is possible to construct a calibration curve that describes the relationship between the sensor output (voltage, current, digital signal, etc.) and the actual physical quantity of interest.

This calibration curve is often expressed in the form of a regression function, such as a linear, polynomial, or logarithmic model, depending on the behavior of the sensor. The parameters of the chosen model can then be used to compute correction factors that translate the raw signal into a reliable estimate of the measured quantity.

In addition, the calibration process allows the experimenter to evaluate the uncertainty associated with the sensor, which includes both systematic and random components. Quantifying uncertainty is essential in order to establish the confidence level of the measurements and to ensure that the sensor meets the accuracy requirements of the specific application.

While this principle provides exceptional sensitivity for biochemical detection, it also makes the sensor output highly dependent on environmental factors, fabrication variability, and surface conditions. As a consequence, calibration cannot be performed universally or generalized across multiple devices: each SPR sensor requires its own individual calibration procedure. This individualized approach ensures that the measured shifts in resonance wavelength can be accurately correlated with the concentration of the analyte under investigation. However, this individual calibration makes the process inherently slow, complex, and costly. The sensor must be exposed to multiple reference samples with known refractive indices or analyte concentrations, often under carefully controlled laboratory conditions. Moreover, the surface profile of each SPR chip can vary slightly due to fabrication tolerances, which adds an additional layer of complexity to the calibration process. These factors not only increase the time and resources required for calibration but also introduce limitations in the scalability of SPR-based sensing technologies, particularly when deploying large arrays of sensors for high-throughput applications.

Due to the intrinsic sensitivity of SPR devices to environmental conditions, fabrication tolerances, and surface variations, it is not possible to adopt a single, standardized calibration curve for all sensors. Instead, each SPR sensor requires its own individual calibration, which ensures that the measured resonance shifts can be reliably correlated with the actual refractive index changes or analyte concentrations. While essential for guaranteeing accuracy, this procedure is often time-consuming, labor-intensive, and expensive, especially when large numbers of sensors must be deployed or when rapid calibration is needed for real-time applications.

In recent years, Artificial Intelligence (AI), specifically Machine Learning (ML), has been increasingly considered as tools to overcome these limitations. The key advantage of AI lies in its ability to capture complex, nonlinear relationships between raw sensor outputs and the true underlying physical quantities, without relying only on analytical models. By training on large datasets of experimental or simulated measurements, AI algorithms can generalize calibration curves, identify hidden

patterns, and predict the sensor response under new conditions with high accuracy. This has the potential to drastically reduce the number of reference measurements required, accelerating the calibration process and lowering its overall cost. Furthermore, AI-based models can be designed to adapt to sensor-to-sensor variability, effectively compensating for the differences introduced during fabrication or surface preparation.

This allows for the development of predictive models that can significantly accelerate the calibration process, reducing the number of experimental reference points needed. AI can even compensate for sensor-to-sensor variability by recognizing common patterns and applying adaptive correction factors, thereby lowering costs and improving scalability. As a result, the integration of AI into SPR sensor calibration not only enhances measurement accuracy but also has the potential to transform these systems into practical tools for real-time monitoring in clinical, pharmaceutical, and environmental applications.

Here AI-driven calibration is investigated as a novel strategy to improve the efficiency and reliability of SPR sensor measurements. The following section presents the methodology adopted to integrate machine learning into the calibration workflow, describing the database construction, pre-processing, and training phases. Subsequently, the results are presented and discussed, with particular attention to the benefits in terms of speed, cost reduction, and robustness, as well as the challenges and limitations that remain. This approach highlights how AI can significantly enhance the usability and scalability of SPR technology, bringing it closer to practical applications in real-world scenarios.

The dataset employed in this study was generated entirely through numerical simulations, rather than direct experimental measurements. This approach allowed full control over the parameters influencing the SPR sensor response, such as refractive index variations, resonance wavelength shifts, and environmental noise. By systematically varying these parameters within physically realistic ranges, it was possible to produce a large set of calibration data while avoiding the time and cost typically associated with laboratory-based procedures. Each simulated instance consisted of input features representing the raw sensor response under specific conditions, paired with output labels corresponding to the true reference values defined in the simulation framework. To enhance realism, stochastic noise and small perturbations were introduced into the simulated signals, mimicking the variability that would

be present in real measurements. Once generated, the dataset was organized into a structured format and preprocessed through normalization and outlier handling, ensuring consistency across all samples. This strategy provided a reliable and scalable foundation for training and validating the AI-based calibration models, while also enabling extensive experimentation with different parameter settings that would be impractical to replicate experimentally.

In the implementation, the simulated dataset was first organized into input and output variables. The input matrix X contained the spectral data obtained from the simulations, where each row represented a full spectrum and each column corresponded to a spectral point. The output vector Y stored the reference refractive index values associated with each simulated spectrum. To ensure an unbiased evaluation of the calibration model, the dataset was divided into a training and a testing subset using a hold-out cross-validation scheme. Specifically, 80% of the samples were allocated to the training set, while the remaining 20% were set aside for independent testing.

A regression tree model [41] was then trained on the training subset to learn the mapping between spectral features and refractive index values. Once the model was fitted, it was applied to the unseen test data to generate predictions of the refractive index. The performance of the model was assessed by calculating the Mean Squared Error (MSE) between the predicted values and the true reference indices in the test set. This metric provided a direct quantitative measure of how closely the model could replicate the ground truth, thereby evaluating its effectiveness as a calibration tool for SPR sensor data.

The evaluation of the trained model on the test set yielded an MSE value, which reflects the average squared deviation between predicted and true refractive index values. A low MSE indicates that the model is able to reproduce the ground truth with good accuracy, confirming that the regression tree successfully captured the relationship between simulated spectral responses and the reference refractive indices. The use of the *fitrtree()* function in MATLAB ® [41] allowed the construction of a regression tree model, a supervised learning algorithm that predicts continuous variables by recursively partitioning the input space into regions with similar output values. At each split, the algorithm selects the spectral feature and threshold that best reduce prediction error, effectively creating a hierarchical decision structure that maps spectral patterns to refractive index values. This method is particularly

useful in the context of SPR calibration, since the spectral response is nonlinear and can exhibit local variations that are difficult to approximate with a single model. By dividing the feature space into smaller, more homogeneous regions, the regression tree provides a simple yet effective way to capture these nonlinearities. Although computationally lightweight and easy to interpret, the regression tree already demonstrates the potential of machine learning to accelerate and automate the calibration of SPR sensors.

5.1 Results

The regression tree model was trained using automatic hyperparameter optimization provided by the MATLAB ® function *fitrtree()*. The software performs a search for the best combination of hyperparameters (e.g., maximum tree depth, minimum leaf size, split criterion) in order to minimize the generalization error. The optimization is carried out constructing a probabilistic surrogate model of the objective function (in this case, the cross-validated error) and iteratively proposes new hyperparameter configurations to evaluate. The choice of the next point is guided by an acquisition function ("*expected-improvement-plus*"). This acquisition function balances exploration (searching new regions of the hyperparameter space) with exploitation, refining the search around already promising regions. The maximum number of hyperparameter configurations tested was limited to 30 and the performance of each candidate model was estimated using 5-fold cross-validation (*'KFold',5*), which provides a more reliable error estimate by reducing the variability due to a single train/test split.

Fig. 5.1a shows the progression of the best cross-validated error achieved as the optimization proceeds.

- The x-axis corresponds to the number of function evaluations (i.e., the number of hyperparameter configurations tested).
- The y-axis corresponds to the minimum objective function value (the cross-validated error).
- The decreasing trend indicates that the optimization procedure is successfully identifying better hyperparameter settings over time.

Fig. 5.1b represents the surrogate model's estimate of the objective function as a function of a key hyperparameter, here the minimum leaf size.

- The plot illustrates how different values of *MinLeafSize* influence the expected cross-validated error.
- It highlights the region of the hyperparameter space where the error is minimized, thereby indicating the most promising range for this parameter.

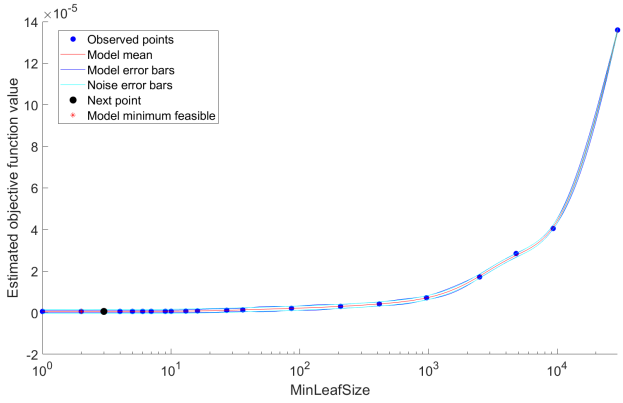

(a) Progression of the best cross-validated error.

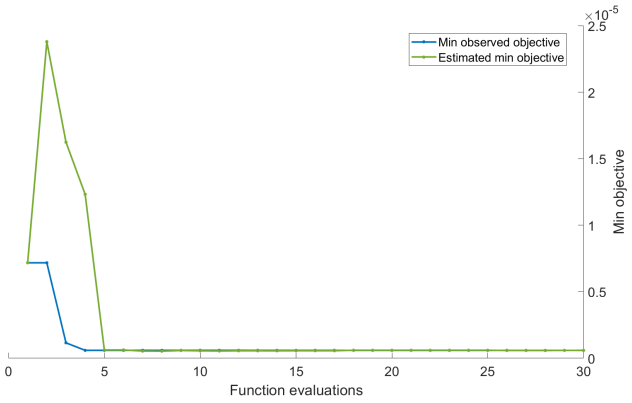

(b) Surrogate model's estimation of the objective function as a function of minimum leaf size.

Fig. 5.1 Optimization results.

The optimization results suggest that the model's predictive accuracy can be substantially improved by selecting appropriate hyperparameters rather than relying on default values. In particular, the analysis of the *MinLeafSize* parameter shows that very large leaf sizes tend to oversimplify the model, resulting in higher errors, while

excessively small leaf sizes risk overfitting. The optimal value lies in an intermediate range, where the trade-off between model complexity and generalization ability yields the lowest cross-validated error.

After the optimization procedure, the regression tree model with the best-performing set of hyperparameters was selected. This optimized model was then retrained on the available training data in order to fully exploit the information contained in the dataset. Subsequently, the trained model was applied to our dataset for the calibration phase, i.e., to generate predictions and compare them with the observed values. This step allowed to evaluate the model's ability to reproduce the experimental data and to quantify its accuracy through error metrics such as the Mean Squared Error (MSE). The analysis of the optimization plots showed that the objective function decreased over successive evaluations, indicating that the procedure successfully identified improved hyperparameter configurations. In particular, the exploration of the *MinLeafSize* parameter highlighted the trade-off between model complexity and generalization, with the optimal range yielding the lowest cross-validated error.

By using the final optimized model in the calibration step, the predictions were ensured to be based on the most suitable configuration discovered during the optimization process. This not only improved the model's accuracy compared to default settings but also provided stronger reliability in the evaluation of the calibration results.

The optimized regression tree model was evaluated on the independent test set, and the results demonstrate a very high level of predictive accuracy. As shown in the scatter plot (Fig. 5.2), the predicted values are tightly clustered along the bisector line, indicating an excellent agreement between the model outputs and the observed data. Quantitatively, the model achieved a coefficient of determination ($R^2 = 0.9965$), confirming that 99% of the variance in the test set is explained by the regression tree. In addition, the MSE $= 4.7 \cdot 10^{-7}$ is extremely low, which demonstrates that the average deviation between predicted and measured values is minimal. These two indicators, taken together with the graphical evidence, highlight the robustness of the optimized model and its ability to generalize beyond the training data. Following this validation, the optimized regression tree was applied to a real dataset in order to perform the calibration phase. The strong performance observed on the test set provided confidence in the reliability of the model when transferred to real-world

data, ensuring that the calibration results are not only statistically but also practically applicable.

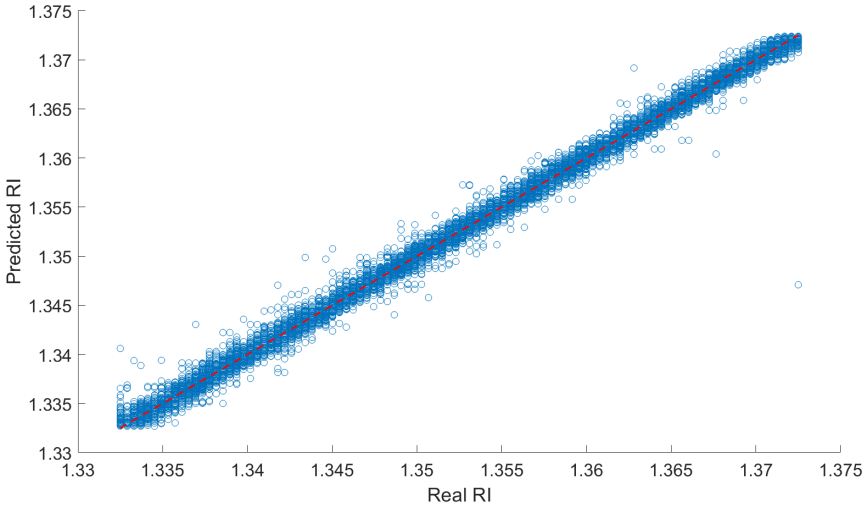

Fig. 5.2 Scatter plot comparing the predicted and real refractive index (RI) values from the simulated dataset. The diagonal line represents the ideal prediction.

5.1.1 Test on a real dataset

Once the model has been trained, was applied to a real dataset. The combination of spectral data acquired from the optical set-up and the refractive index values measured with the refractometer was subsequently used to construct a dedicated dataset. Unlike the datasets employed during the training and preliminary validation stages of the algorithm, this dataset was generated entirely from experimental measurements and therefore represents a real-case scenario. Each dataset entry consisted of the processed transmission spectrum obtained from the sensor and the corresponding refractive index determined independently by the refractometer. The complete dataset (6500 samples) spanned multiple refractive index values – from 1.3413 to 1.3613 – and included measurements from two different sensors, thereby providing a robust experimental basis for testing.

This dataset was employed as an independent case study to evaluate the algorithm's performance under real experimental conditions. In this way, the effectiveness of the algorithm in extracting refractive index values directly from fiber sensor spectra could be assessed in a realistic context, bridging the gap between theoretical

development and practical application. For clarity, the sensor fabrication, the acquisition procedures and experimental protocols followed in the generation of this dataset are described in Appendix A.

The algorithm, previously trained and validated on independent datasets, was tested on the experimental dataset constructed from the fiber sensors. The performance of the model was evaluated by comparing the refractive index values predicted from the spectral data with the actual refractive indices measured using the refractometer. A direct comparison between real and predicted values is reported in Fig. 5.3, where the refractive index obtained experimentally is plotted against the value predicted by the algorithm. Ideally, a perfect correspondence would result in all data points lying on the identity line ($y = x$). The results reveal that the predictions

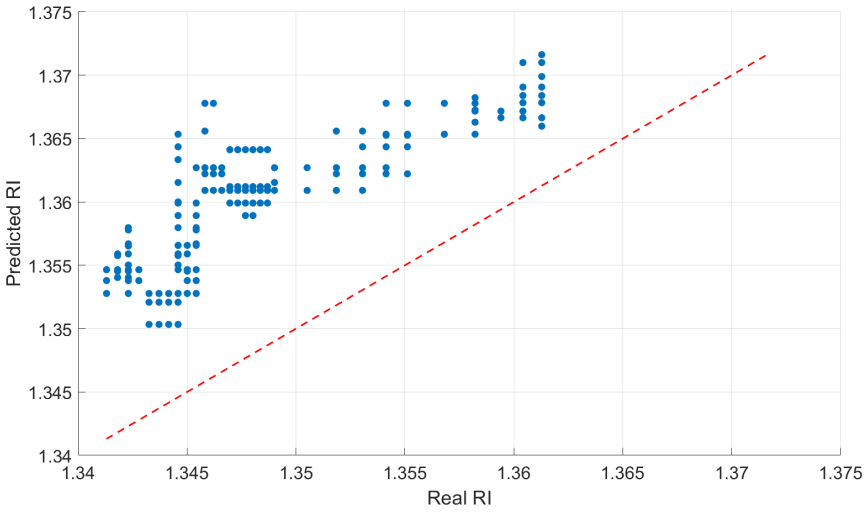

Fig. 5.3 Scatter plot comparing the predicted and real refractive index (RI) values from the experimental dataset. The diagonal line represents the ideal prediction.

exhibit a clear systematic overestimation of the refractive index. This systematic error can be attributed to the fact that the simulations used for algorithm training were based on simplified representations of the optical set-up. These simplifications introduce a spectral shift between the simulated response and the real sensor behavior (Fig. 5.4), which directly translates into a displacement of the predicted values with respect to the measured ones. Fig. 5.5 shows the distribution of the prediction errors obtained from the trained model. The left panel reports the error values as a function of the true RI, while the right panel shows the corresponding histogram of the errors. Also from this plot is evident that the prediction error is always positive, indicating

that the model consistently overestimates the refractive index across the entire range of values.

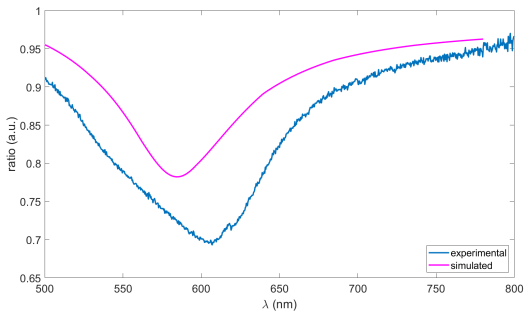

Fig. 5.4 Spectral shift between the simulated (pink) response and the real sensor behavior (blue).

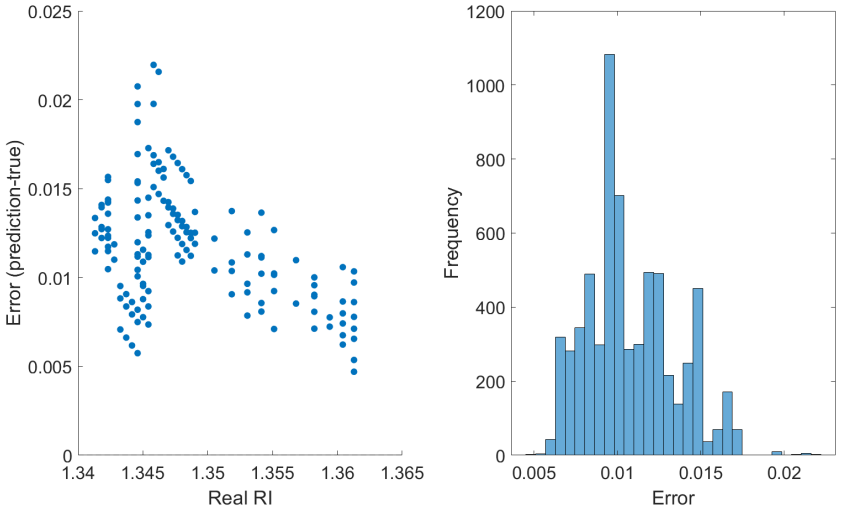

Fig. 5.5 Distribution of the prediction errors. Left: error values as a function of the true RI. Right: corresponding histogram of the errors.

However, since the discrepancy is essentially a constant spectral offset, it can be corrected in a straightforward way. By applying an offset to all predicted values, the corrected results (shown in Fig. 5.6) align almost perfectly with the bisector, indicating that the algorithm is able to capture the correct dependence between the spectral features and the refractive index.

Fig. 5.7 shows the distribution of the prediction errors obtained from the model and corrected for the offset. Now the errors are mostly distributed around zero,

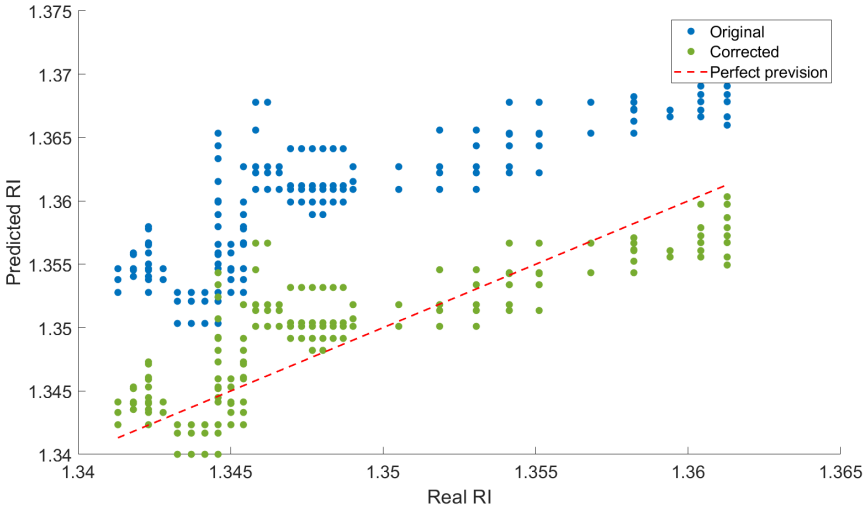

Fig. 5.6 Scatter plot comparing the predicted and real refractive index (RI) values from the experimental dataset after the correction. The diagonal line represents the ideal prediction.

indicating that the trained model provides a reliable estimation of the RI within the considered range, with residual errors mainly due to model generalization limits and the intrinsic variability of the simulated data.

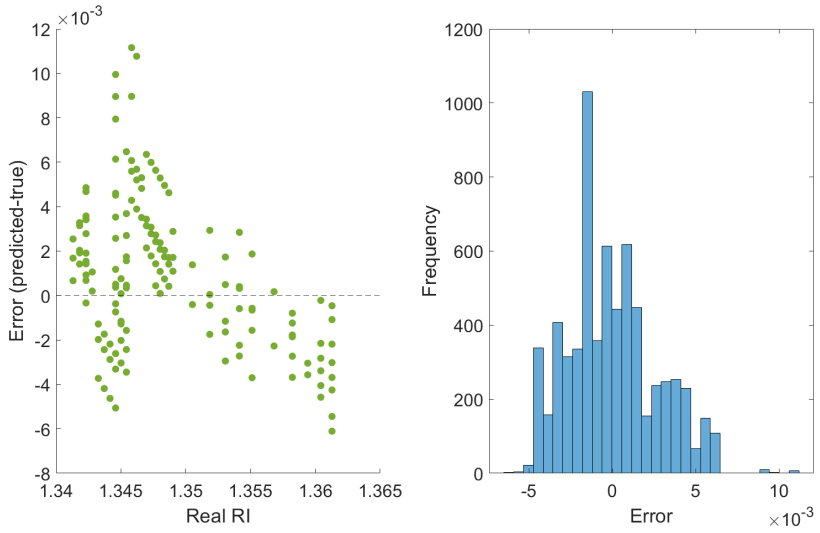

Fig. 5.7 Distribution of the prediction errors after the correction of the offset. Left: error values as a function of the true RI. Right: corresponding histogram of the errors.

The results demonstrate that the majority of the points cluster close to the identity line, confirming that the algorithm is capable of reproducing the experimental values with good accuracy, even if with small deviations. These discrepancies may be attributed to several factors:

- The presence of experimental noise in the acquired spectra.
- Variability among different sensors, arising from fabrication tolerances (e.g., slight differences in metallic film thickness or surface roughness).
- The limited number of solution concentrations tested, which restricts the density of the dataset and therefore the resolution of the calibration.

Despite these limitations, the overall trend shows strong agreement between predicted and measured refractive indices. This indicates that the algorithm, although trained on simulated data (which inevitably introduces some errors), remains valid and requires only minor calibration to adapt to real experimental conditions.

5.1.2 Limitation of the synthetic dataset

Despite the promising results obtained, this work also presents some limitations that are worth discussing, particularly with respect to the use of fully numerically generated datasets for the analysis and calibration of the SPR sensor. In this study, synthetic data were employed to optimize the sensor design and to train and validate the calibration and fitting algorithms, enabling a systematic and controlled exploration of the parameter space. This approach allowed the isolation of specific physical effects, reduced experimental costs, and facilitated repeatability during the early development stages.

However, the exclusive reliance on numerically generated data inherently neglects several non-ideal factors that are present in real-world measurements. These include stochastic noise sources (e.g., intensity fluctuations, thermal drift, and detector noise), fabrication tolerances, surface roughness, material inhomogeneities, and long-term instabilities of the optical and fluidic components. As a consequence, algorithms trained solely on synthetic datasets may exhibit reduced robustness when applied to experimental data, potentially leading to biased estimations or degraded performance under realistic operating conditions.

The use of real experimental datasets, or hybrid datasets combining synthetic and measured data, would represent a significant improvement. Hybrid approaches, which are becoming increasingly common in data-driven sensing and photonic applications, can preserve the physical consistency and completeness of numerical models while incorporating the complexity and variability of experimental conditions. In the specific context of SPR-based water monitoring, such datasets would enable more reliable calibration procedures, improve generalization capabilities, and enhance resilience against noise and environmental perturbations.

Moreover, while stochastic noise modeling is often adopted as a first-order approximation, it may not fully capture structured or correlated disturbances typical of optical sensing platforms deployed in real environments. Future developments could therefore benefit from advanced noise modeling strategies, domain adaptation techniques, or transfer learning approaches, allowing models trained on synthetic data to be progressively refined using limited but representative experimental measurements.

Overall, the use of synthetic data in this work should be regarded as a necessary and effective choice for a feasibility and proof-of-concept study. Nevertheless, the transition towards real or hybrid datasets is a crucial step for translating the proposed SPR sensing strategies into robust, deployable systems suitable for long-term, in-field operation.

Chapter 6

Fluorescence

6.1 Theoretical background

Fluorescence is a phenomenon for which light absorbed by a substance at one wavelength is then emitted at a longer wavelength. When a fluorophore absorbs a photon, one of its electrons is promoted to an excited electronic state; the molecule then relaxes to the ground state by emitting a photon. The difference between the excitation and emission wavelengths, known as the Stokes shift (Fig. 6.1), is a key characteristic of each fluorescent species and determines the color and spectral separation of the emitted light [42]. Fluorescence differs from phosphorescence mainly in the timescale of emission: while fluorescence occurs within nanoseconds after excitation, phosphorescence involves longer-lived excited states and delayed emission. Because of its short lifetime and high sensitivity to the surrounding environment, fluorescence is widely exploited in sensing applications, from biological imaging to chemical analysis and environmental monitoring.

Fluorescence is prevalent in both natural and manufactured materials, including minerals, biological systems, and materials such as fluorescent lighting and dyes. Fluorescence has a wide range of practical uses, for example in mineralogy, gemology, medicine, chemical sensors, biological detectors, and cosmic ray detection. It is also employed in daily products like fluorescent lights and LED bulbs, where it transforms UV or blue light into longer wavelengths to generate white light.

Following excitation, a molecule can return to its ground state either by radiative emission (fluorescence) or through non-radiative processes such as internal con-

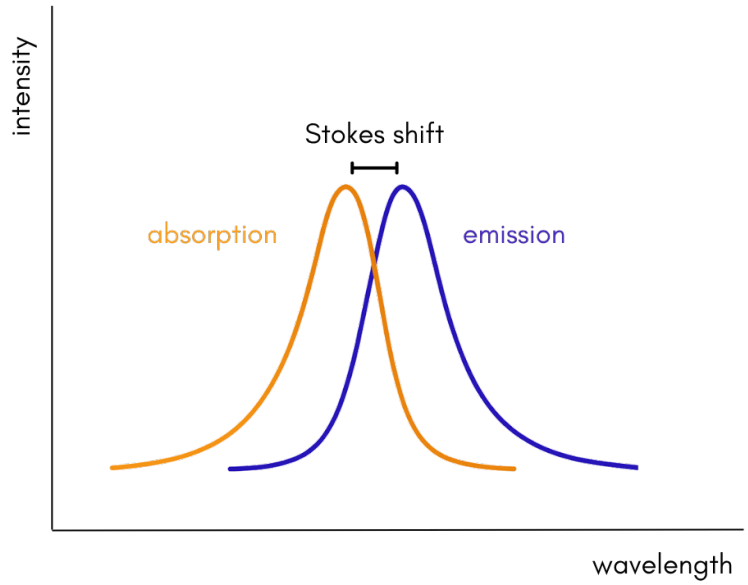

Fig. 6.1 The absorption and emission bands of a molecule. The differences in wavelength between the peaks is known as Stokes shift.

version or vibrational relaxation, where the absorbed energy is dissipated as heat. The balance between these pathways defines the quantum yield, i.e., the fraction of absorbed photons that result in fluorescence. This parameter depends strongly on the molecular structure and on environmental factors such as temperature, solvent, and pH. Jablonski diagrams [43] are used to represent the light shift from absorption to emission; these are an effective tool to visualize the transitions that may occur after a molecule has been photo-excited. Fig. 6.2 depicts a typical Jablonski diagram.

Fluorescence and pH Dependence

The fluorescence behavior of many dyes is highly sensitive to pH, since protonation or deprotonation processes alter their electronic structure and, consequently, their absorption and emission properties. Depending on the pH of the surrounding medium, a fluorophore can exist in different ionic forms with distinct spectra and fluorescence efficiencies.

A well-known example is fluorescein [44], whose emission intensity and spectral position vary markedly with pH. At low pH, the dye is mostly in its neutral or cationic form, exhibiting weak fluorescence; as the pH increases, anionic species become predominant, resulting in stronger emission around 520 nm (Fig. 6.3). This

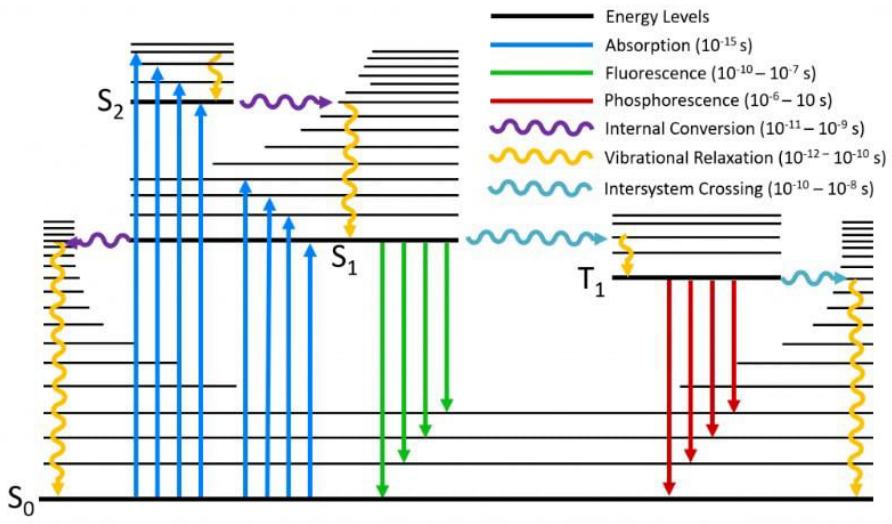

Fig. 6.2 Jablonski diagram, the colored arrows depict the various energy-transfer transitions between molecular states. [43]

pH-dependent behavior enables the use of fluorescein and similar dyes as optical pH indicators.

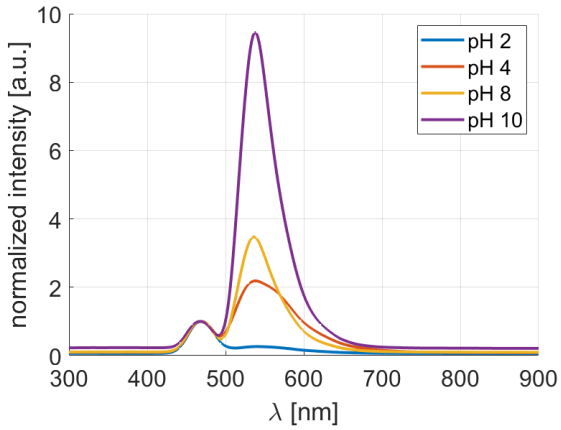

Fig. 6.3 Fluorescein emission spectra at different pH values. The fluorescein peak appears on the right, while the left peak corresponds to the excitation LED used in the experiment. The emission maximum is around 520 nm.

Fluorescence-based sensors exploit this correlation between pH and emission properties to achieve precise and non-invasive pH measurements. By exciting a fluorescent dye with a suitable light source and recording its emission intensity or spectral shift, the pH of the surrounding medium can be continuously monitored.

Such optical approaches offer several advantages over traditional electrochemical methods: they enable miniaturization, remote sensing, and operation in confined or opaque environments. In particular, they are highly compatible with microfluidic systems, where small sample volumes and real-time analysis are essential.

Based on these principles, the next chapter describes the development and characterization of a fluorescence-based microfluidic system for continuous pH monitoring.

6.2 Experimental analysis

The validation of the pH monitoring approach was carried out using the laboratory setup schematically illustrated in Fig. 6.4a, given the aim of assessing the feasibility of the proposed system before designing the actual version in Fig. 6.4b. The primary focus was on measuring the pH of nearly neutral solutions, specifically those with pH values around 7.

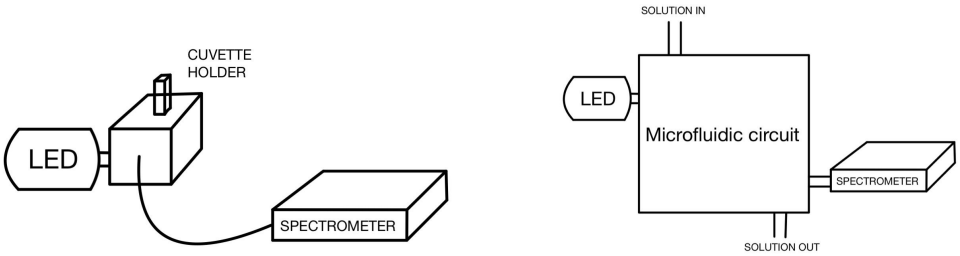

(a) Schematic representation of the lab pH monitoring system.

(b) Schematic representation of a possible in-field pH monitoring system.

Fig. 6.4 Schematic representation of pH monitoring systems.

After conducting preliminary trials, Fluorescein was selected as the fluorophore for the study for its exceptional photo-stability, high fluorescence quantum yield (0.95), and cost-effectiveness.

In order to evaluate the efficacy of Fluorescein in pH tracking, a Fluorescein solution was prepared by dissolving 15 g of Fluorescein ($C_{20}H_{12}O_5$) in 120 mL of distilled water, yielding a molar concentration of $3.76 \times 10^{-1}\,\mathrm{mol\,L^{-1}}$. This solution was subsequently diluted to obtain the working concentration used for fluorescence measurements. Specifically, 0.1 µL of the solution was added to 3 mL of the sample, resulting in a final concentration of $1.25 \times 10^{-8}\,\mathrm{mol\,L^{-1}}$. This value represents the lowest concentration at which the fluorescence emission peak of fluorescein could be clearly detected under the adopted experimental conditions. The working solution was freshly prepared before each measurement to minimize the effects of photobleaching and chemical degradation.

The primary objective of this experiment was to establish a correlation between the fluorescence emission peak and the pH of the solution.

The experimental set-up is illustrated in Fig. 6.4a. The sample was inserted in a cuvette holder, in which a 450 nm mounted LED [45] was added, along with the fiber cable for connection with the spectrometer [46]. This setup is a lab solution, which is useful for preliminary tests, but clearly not suitable for in-field applications. A possible alternative can be represented by a microfluidic circuit (Fig. 6.4b) connected to the solution under analysis and equipped with a small reservoir for the fluorophore dye and a tank to collect the wastewater after the measurement.

Initially, the LED was operated in continuous mode during the entire acquisition period. With these conditions a large decay of the fluorescence peak intensity was recorded over time. At the same time, a gradual increase in the solution temperature was observed, caused by the continuous optical excitation. When the solution temperature returned to ambient conditions, the fluorescence intensity did not recover. This irreversible loss of signal suggests that the phenomenon was not merely thermal but is instead due to photo-bleaching, a process in which prolonged light exposure induces structural modifications in the fluorophore, permanently impairing its fluorescence emission.

Since photo-bleaching represents a significant modification input for reliable pH measurements, the excitation protocol was adapted in order to mitigate fluorophore degradation. In particular, the LED duty cycle was reduced from continuous operation (100%) to 5%, corresponding to an excitation of 3 s/min. This pulsed-excitation scheme was implemented using a National Instruments DAQ board [47], configured as a square-wave generator and connected to the LED driver. The LED operation was controlled through a custom LabVIEW script, which simultaneously managed both the fluorescence acquisition and the excitation timing, thereby ensuring proper synchronization of the measurement process.

This approach was effective in reducing the impact of photo-bleaching, thereby improving the stability of the recorded fluorescence signal and making the method more suitable for long-term pH monitoring applications.

For the calibration of the pH monitoring system, a set of buffer samples was prepared, covering the range pH 5.5 to 9.5 in increments of 0.5 units. The samples were obtained by mixing commercially available standard buffer solutions at fixed pH values (pH 4, pH 7, and pH 10).

When two buffer solutions of different pH are mixed, the resulting pH cannot be determined by a simple arithmetic average, since pH is defined on a logarithmic scale as the negative logarithm of the hydrogen ion concentration (Eq. 6.1):

$$\mathrm{pH} = -\log_{10}\left([H^+]\right). \tag{6.1}$$

Thus, to compute the pH of a mixture, the concentrations of hydrogen ions contributed by each solution must first be calculated and then combined according to the respective mixing ratios. If two solutions of volumes V_1 and V_2, with pH values pH_1 and pH_2, are mixed, the resulting concentration of hydrogen ions is (Eq. 6.2):

$$[H^+]_{\mathrm{mix}} = \frac{V_1 \cdot 10^{-\mathrm{pH}_1} + V_2 \cdot 10^{-\mathrm{pH}_2}}{V_1 + V_2}. \tag{6.2}$$

The pH of the mixture is then obtained as (Eq. 6.3):

$$\mathrm{pH}_{\mathrm{mix}} = -\log_{10}\left([H^+]_{\mathrm{mix}}\right). \tag{6.3}$$

This approach allows the preparation of intermediate calibration solutions (e.g., pH 5.5, 6.0, 6.5, etc.) by accurately mixing the standard buffers in appropriate ratios. The resulting mix was then verified with a pH-meter with a minimum error of ± 0.1pH. Fig. 6.5 reports the spectral response of Fluorescein for different pH values, clearly demonstrating the dependency of the peak fluorescence emission with the pH. In more detail, it can be noted that the intensity around 520 nm decreases as the pH value increases.

However, for a given fluorescein concentration and pH value, the absolute peak intensity value depends on the excitation intensity. Therefore, in order to have an evaluation of the pH without the dependence on the excitation intensity each spectra was normalized with respect to the LED intensity, as shown in Fig. 6.6.

For each investigated pH value, approximately 30 spectra were collected in order to ensure a sufficiently robust statistical basis for the analysis. Fig. 6.7 reports the normalized intensity values. As can be observed, even after normalization, the spectral maximum alone does not represent a sufficiently discriminative parameter: in fact, its intensity does not allow for the unambiguous attribution of a given spectrum to a specific pH value.

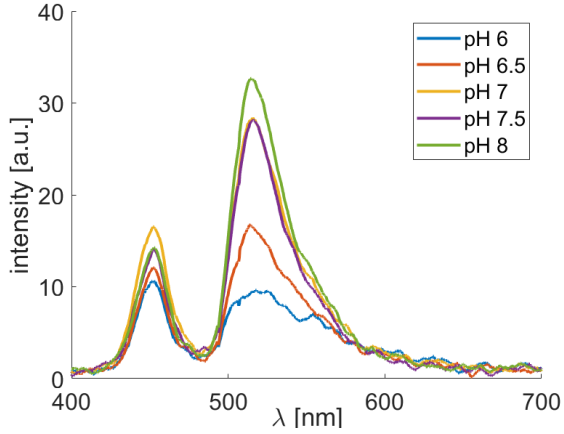

Fig. 6.5 Spectral response of Fluorescein for different pH values.

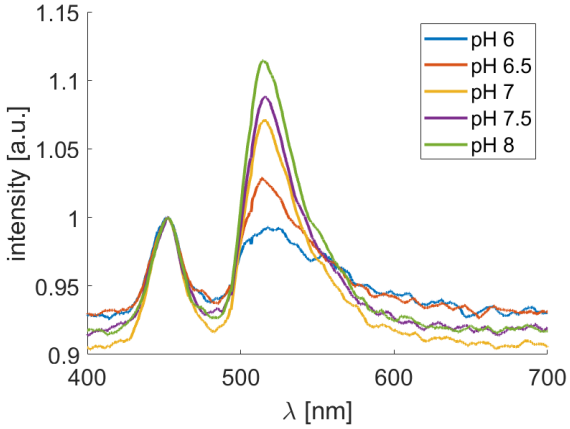

Fig. 6.6 Normalized spectral response of Fluorescein for different pH values.

The subsequent aim of the analysis is therefore to evaluate whether, by considering multiple spectral points simultaneously (rather than relying solely on the maximum) it becomes possible to identify a set of features that uniquely associates each acquisition with its corresponding pH. In other words, the objective is to investigate whether a suitable combination of spectral variables can act as a characteristic "fingerprint" for each pH, thus overcoming the ambiguities encountered when using only the intensity maximum.

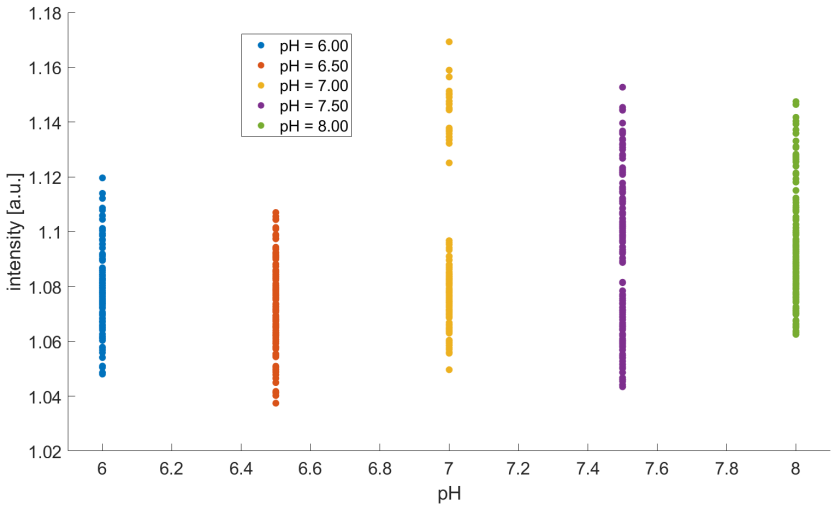

Fig. 6.7 Normalized intensity peaks for different pH values.

6.3 Data analysis

Moreover, the broader goal is to evaluate the feasibility of developing a practical and low-cost pH sensing device that exploits fluorescence without requiring continuous recalibration. Using a broadband spectrometer capable of capturing the full emission spectrum would significantly contribute to the cost of each unit, making the realization of a compact, cost-effective device impractical. To overcome this limitation, an alternative approach based on an eight-channel, low-cost spectrometer is proposed.

To assess this possibility, a MATLAB® simulation was carried out starting from the complete spectral dataset, with the dual objective of verifying whether a distinctive fingerprint can indeed be identified for each pH value and evaluating the suitability of the miniaturized eight-channel spectrometer for this application. To identify spectral features that can be used as markers correlated with specific pH values, the data acquired with the broadband spectrometer were resampled at selected wavelengths. The purpose of this approach was to investigate whether an n-channel spectrometer, ways more affordable than a full-range device, can be employed without compromising the accuracy of the fluorescence peak/pH correlation. In particular, the laboratory spectrometer data were resampled according to the spectral response characteristics specified in the datasheet of a commercial device (AMS AS7341) [48].

The resampling was performed at the central wavelengths of the eight channels, applying appropriate weights to account for their relative sensitivities (see Fig. 6.8).

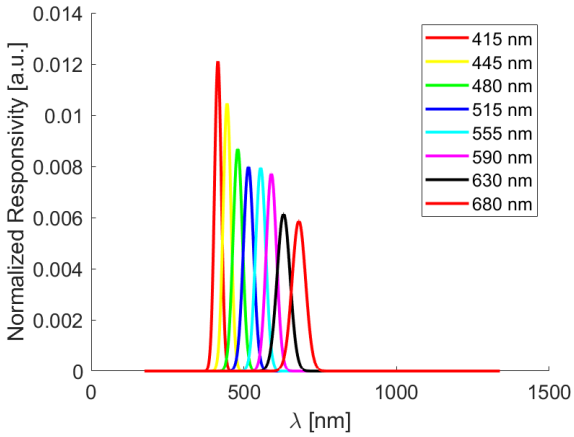

Fig. 6.8 Sensitivity of each channel of the spectrometer (AMS AS7341) [48].

Scatter plots were employed to examine whether consistent and reproducible patterns could still be associated with distinct pH clusters. This work aims to develop a scalable and cost-effective classification framework that can be iteratively refined to reach a specified precision level.

Among the eight available channels, the bands centered at 515 nm and 555 nm were selected for further analysis (highlighted in red in Fig. 6.9 and referred as Channel 4 and Channel 5 from now on), since they are the only ones overlapping significantly with the fluorescence emission peak.

Fig. 6.10 shows the scatter plot of the correlation between the two selected channels. Recognizable clusters corresponding to different pH values were observed. However, when analyzing data collected over multiple days, partial overlaps between these clusters were also evident (Fig. 6.11). This outcome suggests that the current measurement protocol has limited repeatability, probably due to experimental noise and uncontrolled environmental factors. It expected that reducing this variability allows having a datasets with well-separated clusters, enabling the effective application of classification algorithms. When clustering the data obtained within a single measurement cycle for each pH, the degree of overlap between clusters decreases significantly (Fig. 6.10). Although the separation is improved, variability across successive acquisitions within the same cycle remains evident. This highlights that the main limitation is not the spectrometer resolution alone, but the intrinsic instability

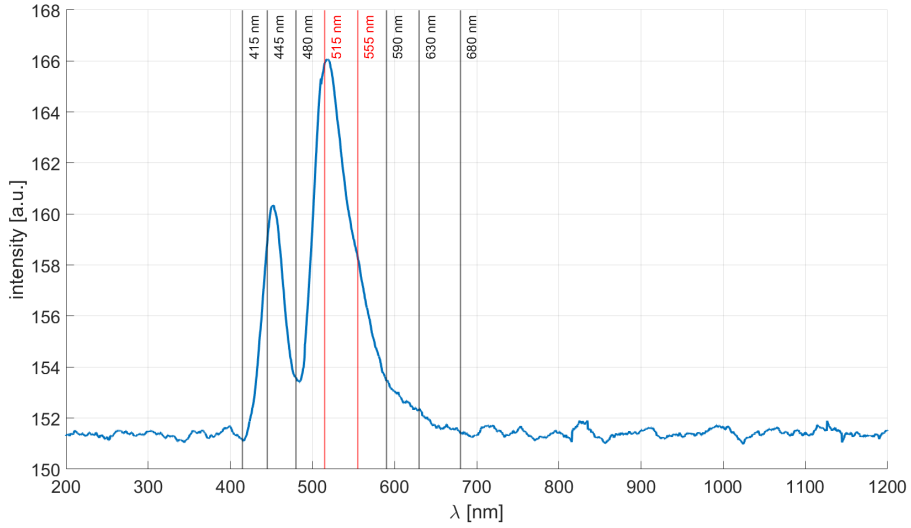

Fig. 6.9 Example of spectra with the positions of the 8 channels of the spectrometer. 515 nm and 555 nm channels (selected for the analysis and referred as Channel 4 and Channel 5) highlighted in red.

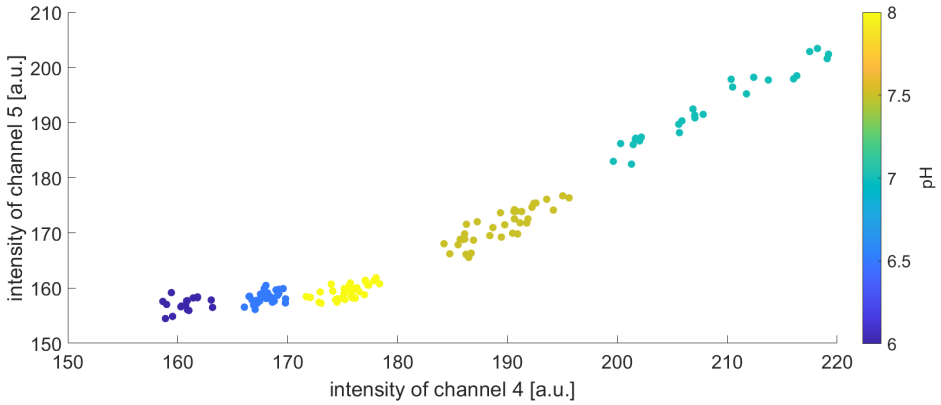

Fig. 6.10 Scatter plot illustrating the correlation between the responses of the two selected channels (4 and 5) for a single acquisition.

and reproducibility of the fluorescence measurements under the current experimental conditions. Therefore, error reduction strategies, such as improved calibration protocols, temperature and excitation-source stabilization, must be considered in order to achieve the level of repeatability required for a reliable sensor.

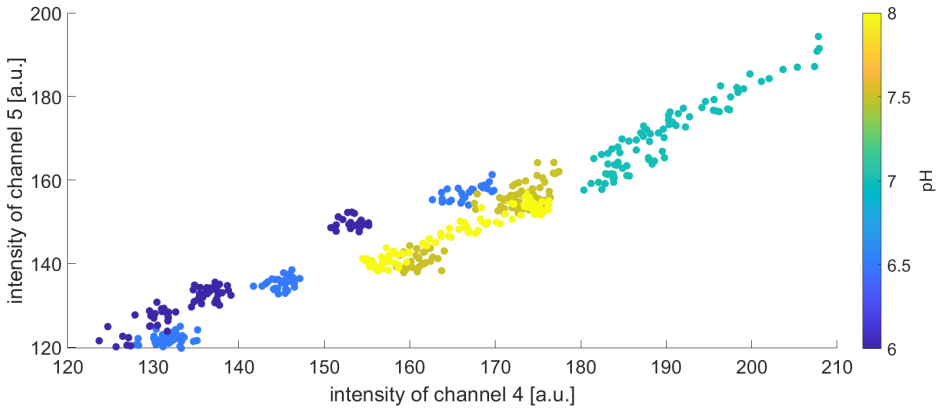

Fig. 6.11 Scatter plot illustrating the correlation between the responses of the two selected channels (4 and 5) across three independent measurements. Each acquisition cover the entire pH range analyzed.

6.3.1 Data post-processing

To analyze the acquired spectral data, a supervised classification approach based on the k-Nearest Neighbors (kNN) [49] algorithm was adopted. The feature set was constructed from the selected spectral channels, while the corresponding pH values were used as class labels. A kNN classifier with three neighbors (k = 3) was trained using the MATLAB® function *fitcknn()* [50] provided by the Statistics and Machine Learning Toolbox [37]. To evaluate its predictive ability, the model was tested on new input points, yielding a predicted pH value based on the nearest neighbors in the training set.

The kNN algorithm was selected for this analysis due to it simple, non-parametric, and instance-based learning approach. In kNN, classification is performed by assigning an unknown sample to the majority class among its k nearest neighbors in the feature space, with proximity typically evaluated using the Euclidean distance. This characteristic makes the method particularly suitable for small datasets, where more complex machine learning methods may not be justified, and where interpretability and robustness are key requirements. In this work, kNN provided a straightforward framework to explore whether distinct pH clusters could be separated in the reduced feature space obtained from the spectrometer channels.

In order to assess the generalization capability of the classifier, cross-validation was performed using the *crossval()* function. The average classification error was

then computed with *kfoldLoss()*, providing an estimation on the model reliability across multiple folds of the dataset. This procedure reduced the risk of overfitting and ensured that the reported performance was not biased by a specific training/test split. Furthermore, the decision boundaries of the trained classifier were visualized. A fine grid of points spanning the feature space was generated, and to each point was assigned a predicted label using the trained kNN model. The resulting decision regions were plotted as a scatter map, with the original data points superimposed to highlight their distribution relative to the classification boundaries. The visualization, shown in Fig. 6.12, illustrates both the partitioning of the feature space induced by the classifier and the location of the experimental data within it.

Also from this representation of the data is evident how the clustering works perfectly when a single acquisition is done while presents some overlapping when more acquisitions are considered. Interestingly the kNN algorithm is able to discriminate between different pH values with accuracy of 90.36% even with the already discussed reproducibility issues, meaning that, with a more complex data processing, the sensitivity can be improved without the need of expensive setups or trained technicians.

The kNN algorithm was selected for this analysis due to it simple, non-parametric, and instance-based learning approach. In kNN, classification is performed by assigning an unknown sample to the majority class among its k nearest neighbors in the feature space, with proximity typically evaluated using the Euclidean distance. This characteristic makes the method particularly suitable for small datasets, where more complex machine learning methods may not be justified, and where interpretability and robustness are key requirements. In this work, kNN provided a straightforward framework to explore whether distinct pH clusters could be separated in the reduced feature space obtained from the spectrometer channels.

In the case of classification, the procedure can be summarized as follows: for a new input point, the algorithm identifies the k training samples that are closest in the feature space, typically using Euclidean distance as a metric. The class of the new point is then determined by a majority vote among these neighbors. The parameter k controls the smoothness of the decision boundaries: small values of k (e.g., 1 or 3) lead to highly flexible boundaries that may capture local variations but can be sensitive to noise, while larger k values produce smoother, more generalized boundaries at the cost of losing sensitivity to fine distinctions.

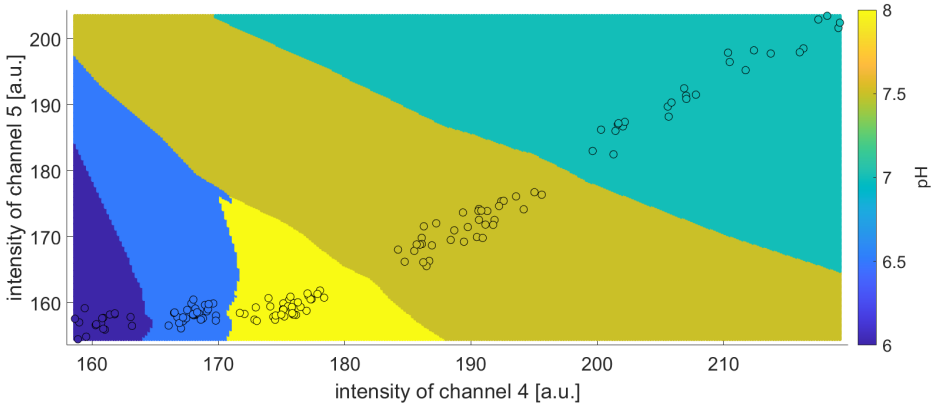

(a) Single measurement.

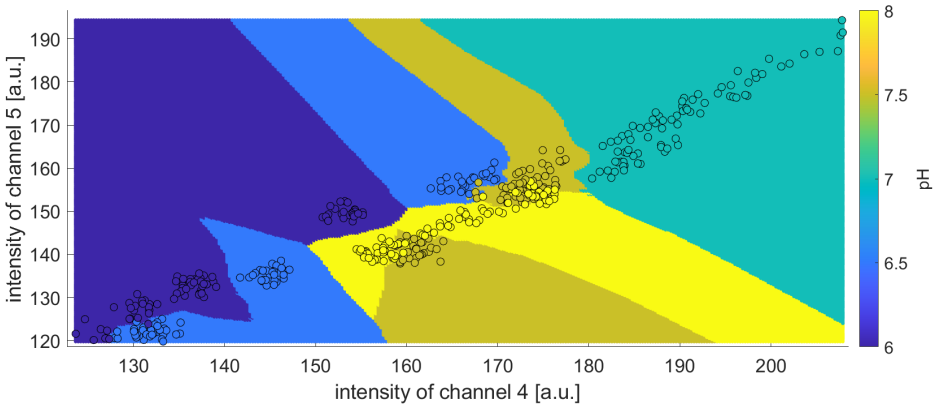

(b) Three independent measurements.

Fig. 6.12 Decision regions plotted as a scatter map, with the original data points superimposed.

The strengths of kNN lie in its simplicity, non-parametric nature, and interpretability. Since no assumptions are made about the underlying data distribution, kNN is particularly useful in exploratory analysis or when prior knowledge about the data structure is limited. Its main limitations are computational cost for large datasets (because all training samples must be considered at prediction time) and sensitivity to irrelevant or poorly scaled features.

In this work, kNN was chosen as a first approach because the dataset was relatively small and low-dimensional, making computational cost negligible. Moreover, the method provides an intuitive and visual way to assess whether distinct pH clusters can be separated in the reduced feature space derived from the spectrometer channels. By visualizing the decision regions generated by kNN, it becomes possible to

evaluate whether the selected features contain sufficient information to discriminate between different pH values and to guide the design of more advanced classification strategies.

The performance of the k-nearest neighbors (kNN) classifier was evaluated through a combination of cross-validation and classification error analysis. In this work, the dataset, with spectral features corresponding to different pH values, was used to train and test the model by means of k-fold cross-validation. This approach divides the dataset into k equally sized subsets, iteratively training the model on (k–1) folds and validating it on the remaining one. The mean misclassification rate, computed across all folds using the MATLAB® function *kfoldLoss()*, provides a robust estimation of the model's generalization ability and its sensitivity to data variability.

In addition to numerical performance metrics, visual inspection of decision boundaries was employed to qualitatively assess the classifier's ability to separate the data. The decision regions generated by the trained model were plotted over the feature space, with the experimental data points superimposed. This visualization enables an intuitive understanding of how well the classifier distinguishes between pH clusters, revealing whether the selected spectral channels contain enough discriminative information.

In this specific case, performance evaluation is particularly important because the data originate from a low-resolution, reduced-channel spectrometer simulation. The goal is not only to achieve high classification accuracy, but also to determine whether meaningful clustering can be maintained despite the limited spectral resolution. A low cross-validated classification error and well-separated regions in the decision plot would indicate that the miniaturized spectrometer provides sufficient information for reliable pH classification.

6.4 Device prototype

To enable a portable and low-cost setup for handling and mixing the tracer and sample solutions, a passive microfluidic circuit was designed, providing precise fluid control without the need for bulky or expensive instrumentation.

The design process began with the creation of a preliminary CAD model in Autodesk Fusion 360, which defined the overall geometry of the fluidic network. The resulting model was exported in STL format and subsequently imported into COMSOL Multiphysics® for numerical simulation. Within COMSOL Multiphysics®, the geometry was converted into a two-dimensional cross-section representing the fluidic channels, which served as the computational domain for the analysis.

The simulations employed a combination of physics interfaces: the Laminar Flow module, which solves the Navier–Stokes equations for an incompressible Newtonian fluid, and the Transport of Diluted Species module, used to model the evolution of the tracer concentration under the combined effects of advection and diffusion. The finite-element solver was thus able to predict the deterministic streamlines and concentration gradients characteristic of laminar microfluidic flow.

Through iterative optimization, the channel geometry was progressively refined by introducing features such as serpentine paths, wall protrusions, and split-and-recombine structures. Each modification was evaluated through simulation to assess its influence on mixing efficiency. This approach enabled a substantial reduction in the need for extensive experimental prototyping, thereby accelerating the overall design and validation process.

Fig. 6.13a illustrates the initial microfluidic architecture, which consisted of a planar serpentine channel designed to promote passive mixing primarily through diffusion. The circuit has two inlets, one for the sample and one for the tracer, and a single outlet chamber to collect the resulting mixture. The elongated path of the serpentine channel was intended to increase the contact time between the two fluids, thereby enhancing mixing within the constraints of laminar flow.

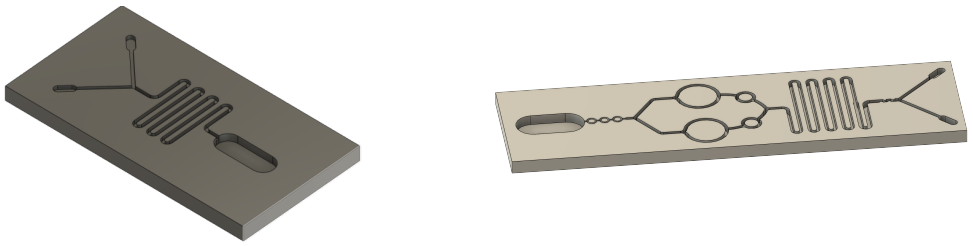

(a) Initial microfluidic architecture, which consisted of a planar serpentine channel.

(b) Optimized microfluidic with a split-and-recombine strategy.

Fig. 6.13 Two microfluidic architectures.

In the improved design, shown in Fig. 6.13b, a split-and-recombine strategy was implemented to further enhance the mixing efficiency of the device. The optimized microfluidic circuit comprises several key components, highlighted in Fig. 6.14:

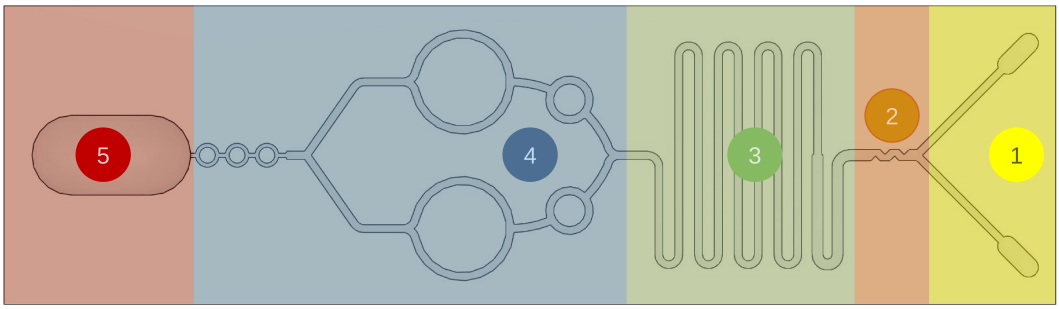

Fig. 6.14 Optimized microfluidic circuit with highlighted key components.

1. Inlet Ports: two dedicated inlets allow the introduction of the solutions to be mixed.
2. Wall Protrusions: immediately after the Y junction, small protrusions are incorporated along the channel walls. These structures disturb the parallel laminar flow, forcing the fluids to merge into each other's flow paths, enhancing mixing at an early stage.
3. Serpentine Channel: The main section of the mixing circuit consists of a long serpentine channel with multiple bends. At the beginning of the serpentine, the channel width is reduced to increase the interaction between the fluid layers and improve mixing efficiency.
4. Split-and-Recombine Chambers: the two streams then converge in circular mixing chambers, providing an additional stage of mixing. The flow is then split and recombined across three further circular chambers.
5. Output Channel: the mixed solution flows through a single output channel. The miniaturized spectrometer and the temperature NTC sensors, which perform real-time analysis of the fluid, are positioned above this channel .

This design approach combines passive mixing strategies such as serpentine geometry, wall protrusions, and split-and-recombine chambers to achieve efficient passive mixing in a compact, low-cost microfluidic system suitable for portable applications.

The serpentine channel offers several advantages for passive mixing in microfluidic systems. First, it promotes chaotic advection: the curved layout generates a complex flow pattern while keeping the flow laminar, causing the fluid layers to fold, stretch, and recirculate, which improves mixing. Second, the serpentine geometry increases the total path length of the fluids, allowing more time for both diffusion and advection to occur. Third, the design enhances diffusion thanks to the high surface-to-volume ratio typical of microfluidic channels, which is further increased by the serpentine shape and the extended flow path. Finally, the channel is simple and reliable, as it can be produced using standard microfabrication methods and does not require moving parts or external energy sources. In a practical implementation, the microfluidic circuit would be interfaced with two inlet pumps to independently deliver the solutions into the device, while a third pump would be used to flush and empty the sensing chamber after the measurements are completed. However, this configuration is intended solely as a feasibility study, aimed at validating the proposed mixing strategy and overall system architecture rather than representing the final operational design.

This microfluidic design achieves passive mixing, relying solely on fluid dynamics rather than external forces such as magnetic fields, heat, or electrical stimulation. The serpentine geometry generates microscale chaotic advection, effectively mimicking turbulent mixing within a laminar flow regime. This increases contact between the solutions, enhances diffusion, and results in efficient mixing.

6.4.1 Prototype Testing and Simulation

An initial experimental prototype of the microfluidic circuit was developed to provide a validation of the proposed mixing idea. This early version, fabricated at a larger scale with channels approximately 1 mm wide, allowed a visual inspection of the fluid behavior and a qualitative assessment of the passive mixing performance. Although this configuration cannot be considered a true microfluidic device, it provided essential insight into the flow dynamics and confirmed that the designed geometry could promote mixing even in the absence of active elements.

The scaled-up prototype was also tested experimentally by flowing a colored dye solution and a transparent reference fluid through the inlets. Despite being a qualitative test, the results visually confirmed the numerical predictions, showing

that the designed geometry promoted efficient passive mixing through a combination of advection and diffusion.

Some practical limitations were observed, mainly due to the material used for fabrication. The prototype was printed in polylactic acid (PLA), which, while non-porous, exhibits relatively high surface friction and roughness. This required reduced flow rates to maintain laminar conditions and occasionally caused leakage or overflow since the prototype was not hermetically sealed. The circuit will be fabricated in PMMA (polymethyl methacrylate) to achieve a true microscale realization of the proposed design. PMMA offers several advantages for microfluidic applications, including low surface friction, optical transparency, and chemical stability, enabling more reliable fluid handling and quantitative optical analysis. The transition to PMMA will allow to validate the simulation results experimentally and to have a fully functional, low-cost, portable pH sensing platform.

Following these preliminary test, a simulation using COMSOL Multiphysics® was carried out to evaluate the feasibility and optimization potential of the proposed design at microscale dimensions. Two physical interfaces were employed and coupled to fully describe the system's behavior:

- Laminar Flow: This module solves the Navier–Stokes equations for an incompressible, Newtonian fluid, providing detailed information on the velocity field, pressure distribution, and streamline structure inside the channels. The simulations were done under laminar flow conditions, where the Reynolds number remains below the critical threshold for turbulence, ensuring stable and predictable flow.

- Transport of Diluted Species: this module was used to solve the advection–diffusion equation to model the dispersion of the fluorescent tracer within the flow. This enabled the analysis of both spatial and temporal evolution of concentration profiles for the tracer and analyte solutions. The two interfaces were coupled such that the velocity field computed by the Laminar Flow module directly drove the convective transport in the Transport of Diluted Species module.

The simulation setup included inlet boundary conditions specifying velocity and concentration for each incoming stream, no-slip wall boundaries along the

channel walls, and a convective flux condition at the outlet. A parametric sweep was then performed over different flow rates and geometrical parameters to analyze their influence on the mixing efficiency. Results confirmed that simple straight or narrowed channels were unable to achieve satisfactory mixing, as diffusion alone was insufficient to mix properly the two fluids. Fig. 6.15 shows that at the output the two fluids are well separated at the two extremities of the channel. However, the introduction of serpentine paths, wall protrusions, and split-and-recombine chambers significantly enhanced the interfacial area between the two liquids and leaded to more uniform concentration fields.

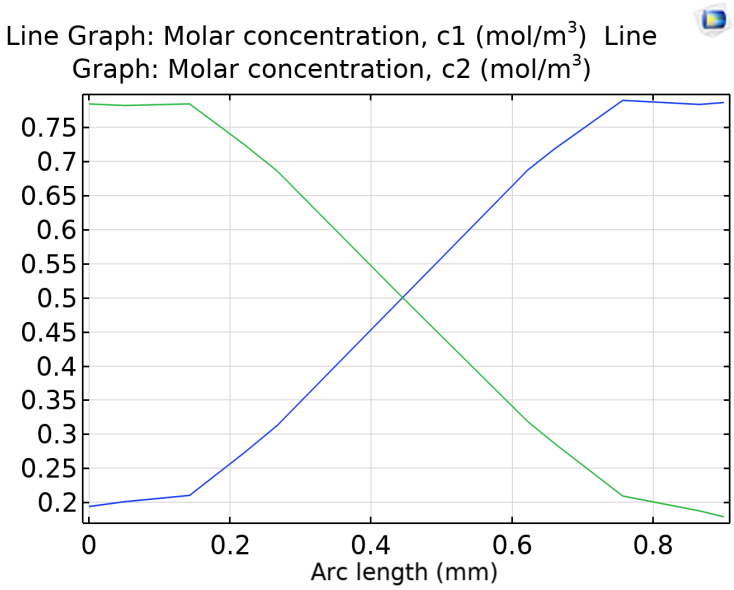

Fig. 6.15 Molar concentration of c_1 and c_2 after the simple straight channel.

The primary objective of this analysis was to quantify how effectively the tracer and sample solutions merged along the flow path, and to determine whether the geometry ensured a uniform concentration distribution at the outlet.

In the preliminary phase, qualitative analysis was performed by visually inspecting the concentration maps generated by the Transport of Diluted Species module. These maps provide a direct visualization of the concentration gradients throughout the channel and allow identification of regions where diffusion and advection are most active. In particular, a well-mixed region appears as a homogeneous color field, while the presence of sharp color transitions indicates incomplete mixing.

This visualization approach was useful to compare different geometrical configurations, such as straight channels, channels with width reduction, serpentine patterns, and split-and-recombine architectures. The qualitative results confirmed that while diffusion alone in simple geometries was insufficient, the addition of curved paths and wall perturbations significantly enhanced contact between the fluids, leading to a more uniform concentration distribution downstream (Fig. 6.16).

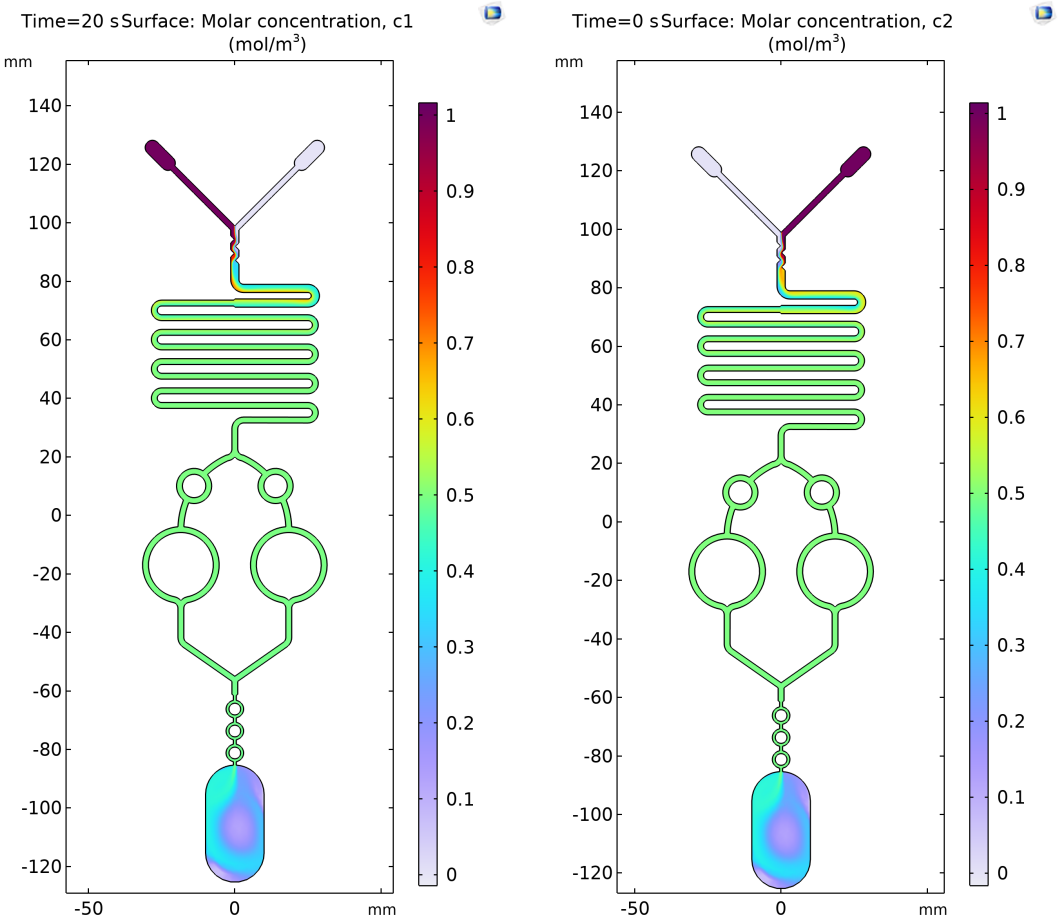

Fig. 6.16 Molar concentration distribution of c_1 (a) and c_2 (b). At the end of the split-and-recombine stage the concentrations are both 0.5 meaning that the two solutions are perfectly mixed.

To complement the visual analysis, a quantitative metric was introduced to evaluate mixing performance.

The concentration difference $\mid c_1 - c_2 \mid$ was used as a complementary measure to map the local concentration imbalance along the channel. Although this simple

difference can sometimes be misleading (e.g., in regions where no flow occurs, the difference may appear zero even without actual mixing) it remains a valuable qualitative indicator when interpreted together with the flow field and concentration maps.

The computed results demonstrated that the serpentine with split-and-recombine configuration provided the highest mixing efficiency. The progressive bending of the channels generated secondary flow vortices and chaotic advection, which continuously folded and stretched the fluid interfaces. These effects greatly enhanced the action of molecular diffusion, leading to a nearly uniform concentration field at the outlet. In contrast, the straight channel and simple narrowing geometries exhibited poor mixing performance, with the mixing index remaining low even at high residence times. The simulations confirmed that the enhanced design could achieve a mixing nearly to homogeneous mixture at the outlet cross-section.

Overall, the combination of qualitative visualization and quantitative mixing metrics provided a robust framework for evaluating and optimizing the microfluidic geometry prior to fabrication. These results validated the feasibility of the proposed design and demonstrated that efficient passive mixing can be achieved without the need for active components or external energy sources.

Part II

Cultural heritage monitoring

Chapter 7

Cultural Heritage

Cultural Heritage conservation is a well-established discipline that has evolved continuously since the nineteenth century. Initially founded on empirical practices, it has progressively developed through the adoption of scientific methodologies. Over the last decades of the twentieth century, technological progress provided conservators with advanced tools to better understand original artistic techniques. From that moment the characterization of materials has become a fundamental step to allow the development of new recovery and restoration methodologies. Today, research efforts are increasingly directed toward the development of new, more efficient recovery and conservation methodologies based on a scientific and quantitative approach.

In recent years, multi-analytical approaches have become central to conservation science [51]. These methodologies typically combine imaging techniques for an initial screening of the surface distribution of materials, followed by quantitative or semi-quantitative spot analysis for the chemical and morphological characterizations of micro-sample [52]. Optical and electronic microscopy investigations often complement these analyses, providing high-resolution insight into surface structures and degradation patterns. Among the various analytical techniques available, electron microscopy is particularly valuable for its ability to deliver detailed information on the fine microstructure and stratigraphy of surfaces. However, its routine and extensive use during conservation treatments is limited due to its invasiveness both because small samples must be extracted from the artifact, and because the sample preparation for the analysis makes it disposable; moreover, it may influence the measurement outcomes. Other non-invasive or minimally invasive techniques,

such as multi-spectral imaging [53], are increasingly used, sometimes integrated with chemical analyses like Fourier Transform Infrared (FTIR) spectroscopy or gas chromatography–mass spectrometry (GC-MS). An accurate evaluation of the composition and thickness of at least the most superficial layer of an artifact provides essential information prior to any conservation treatment planning, in particular, when the treatment devises removal of substances from the original artifact.

Cleaning, in particular, is considered one of the most delicate operations in conservation practice due to the potentially irreversible effects it may have on the artwork. The effectiveness and safety of a cleaning procedure are usually assessed by analyzing the surface before and after preliminary cleaning tests. However, this procedure may not be effective because the layers to be removed generally lack thickness homogeneity. Although scientific research has provided several methodologies to ensure gradual and selective removal of unwanted materials [54–56], the monitoring of treatment effects in real time remains a major challenge: it is difficult to objectively monitor the impact of any treatment in real time, going beyond subjective assessments by the conservator. However, in the event of inadequate treatment, permanent damage occurs and recovery of the original material is impossible. For these reasons, the real challenge in monitoring cleaning treatments is having stratigraphic information with a nondestructive tool, which must also work in real time and be cost effective [57, 58].

Optical methods have recently emerged as promising tools for non-invasive monitoring of cleaning processes. Alongside multi-spectral imaging, other optical techniques such as colorimetric analysis, profilometry, photoacoustic, reflection infrared spectroscopy, and Optical Coherence Tomography (OCT) [59] have shown great potential for use in conservation. In particular, OCT is attractive for its good balance between the information available and the complexity of use [60, 61].

OCT operates by exploiting a low-power broadband light source or a swept laser to generate cross-sectional images of semi-transparent samples, with micrometer-scale resolution and very fast acquisition times. Because OCT is a non-contact technique and can be implemented as a portable instrument, it is commonly used in biomedical applications to obtain images of tissues below the surface. In recent years, its use in cultural heritage conservation has gained increasing attention, supported by advancements in instrumentation, data processing and segmentation algorithms.

Studies published so far mainly report qualitative evaluations of the cleaning process evolution, without attempting to quantify the actual thickness of the layers, which instead requires an accurate estimation of their refractive index values [62]. Moreover, OCT performs best when the investigated layers are semi-transparent and exhibit a clear refractive index contrast. To overcome these limitations, the most promising approach for effective aid during cleaning of artifacts is to combine OCT measurements with data from other techniques, such as FTIR spectroscopy [63].

Within this framework, an alternative approach based on the integration of OCT with Fluorescence Spectroscopy (FS) is being explored. FS offers rapid, reagent-free analysis with minimal sample preparation and provides great sensitivity. Many materials exhibit characteristic fluorescence spectra, acting as natural fluorophores; this property can be exploited to identify specific chemical fingerprints. When combined with machine learning algorithms, fluorescence data can also support the estimation of refractive index values required for quantitative OCT analysis.

As a step toward the integration of these different optical technologies, it is necessary to validate the ability of OCT and related techniques to accurately measure and discriminate material layers in artworks surfaces. The present study focuses on this validation, for the first time using a simple and low-cost commercial OCT instrument [64] that offers acceptable performance at a price significantly lower than conventional systems. The primary objective is to assess whether such an instrument can provide reliable, reproducible, and non-invasive measurements suitable for both laboratory testing and potential in situ applications.

Chapter 8

OCT monitoring

To date, imaging analyses providing preliminary insights to understand the distribution of the superficial film-forming materials are usually integrated by non-invasive and micro-invasive spot analyses, to inform conservators with chemical characterization, description of the stratigraphic sequences and with specific measurements of materials' thickness. The information gained, represent only the point at the sampling area: a variability must be always considered. While performing cleaning treatments, conservators monitor the effectiveness and safeness of their practice almost under stereo microscopes or through magnifying tools. The analytical measure of the results is eventually carried out only after the treatment and conservators must lean back to personal technical competence, experience, precision, and capability of observation. Any occurred damage, especially at microscopic and chemical levels, is only detected but not prevented.

OCT is an optical imaging technique capable of generating a cross-section image of semi-transparent samples, with micrometer resolution. OCT is fast (a cross-sectional image is produced within milliseconds) and uses very low levels of light. Moreover, being a non-invasive and non-contact technique and featuring capability of in-situ measurements, OCT is a very attractive tool for applications in the cultural heritage restoration.

OCT, employing either a low power broadband source or a swept laser, producing a cross-section image of semi-transparent samples and yielding fast sampling (images are produced within milliseconds) and micrometer resolution. It is attractive for its good balance between the information available and the complexity of use [60] [61].

OCT, in its simplest and low-cost implementation, uses a low-coherence broadband light in the near infrared region (usually in the range 0.7 µm to 1.5 µm, with investigations at 2 µm using custom instruments [65]) and the optical signal is reflected by the sample, which behaves as one arm of a Michelson interferometer. Interferometric patterns are collected and processed over a scanning length to return the internal structure of the sample.

The results of the measurement are then shown as a grayscale map extending in depth (up to 3 mm) and whose intensity levels depend on the refractive index and scattering coefficient of the materials. Because OCT is a non-contact technique and can be implemented as a portable instrument, it is commonly used in biomedical applications to obtain images of tissues below the surface [66], but it is proved to be a promising tool in the conservation of cultural heritage thanks to the development of new systems and segmentation algorithms [67]. However, studies published so far mainly report qualitative evaluations of the cleaning process evolution, without attempting to quantify the actual thickness of the layers, which instead requires an accurate estimation of their refractive index values [62]. Besides, OCT is very effective only when the layers under investigation are semitransparent and have a sufficient refractive index contrast. For these reasons, a recent work has highlighted that the most promising approach for effective aid during cleaning of artifacts is to combine OCT measurements with data from other techniques, such as Fourier transform infrared (FTIR) spectroscopy [63].

As a preliminary step, it is necessary to validate the ability of the OCT to discriminate and measure the thickness of layers, in particular those of layered varnishes, to be used as a portable aid during processes of cleaning and removal of superficial layers of painted surfaces. In this first part of the work, only the validation of the OCT alone is performed, providing also different tools (based on AI and image processing) to speed up image analysis.

The primary objective is to assess whether such an instrument can provide reliable, reproducible, and non-invasive measurements suitable for both laboratory testing and potential in situ applications. Two sets of layered samples were prepared: the first, with well-defined and controlled layer thicknesses, was used to calibrate the measurement procedure; the second, with hand-brushed layers that replicate typical coated painted surfaces, served as a testbed for OCT-based thickness evaluation. The OCT-derived measurements were validated through comparison

with coating thickness gauge and Scanning Electron Microscopy (SEM), considered benchmark techniques for this type of analysis. Furthermore, a series of repeated OCT measurements was carried out to assess the reproducibility of the method.

8.1 OCT capabilities analysis

The potentiality of OCT was investigated in a simplified case, but representative of actual scenarios: a layer of Paraloid® B72, a transparent protective material, applied on Egyptian blue painting. Paraloid® B72, an ethyl methacrylate-methyl acrylate copolymer, is one of the most used chemicals in restoration of artifacts thanks to its properties of being stable, water resistant and non-yellowing finish. It is extensively employed by conservators as a coating, consolidant, and adhesive, even if in some cases leads to an increase of superficial gloss and in others to matting, yellowing, adhesion and possible incorporation of atmospheric particulate [68, 69].

Egyptian blue, a pigment used in ancient Egypt, is a calcium copper silicate, whose accepted chemical formula is the same as cuprorivaite ($CaCuSi_4O_{10}$) [70]. It represents a relevant test-bench for the evaluation of the optical techniques described in this work because it mimics a porous layer of color generally coated by an acrylic resin with different thickness, frequently found on real artifacts. Modern artworks or restored artifacts can exhibit irregular acrylic resin coatings over such pigments, making Egyptian blue a relevant model substrate.

OCT is compared with coating thickness gauge and SEM to validate and calibrate the measurement procedure. Both methods, while being a reference for in-lab measurements and during sample preparation, do not permit monitoring "on field". In particular, the first requires the varnish to be measured during the deposition process or at least while the varnish is still wet. On the other hand, SEM requires a micro-invasive sampling to allow the measurement of the layers thickness, giving a pre-treatment information, and it is not considerable suitable for a monitoring during the intervention. In addition, SEM allows for a single measure in a limited number of locations to minimize damages, whereas OCT allows monitoring of the extended area and repeating the measurements multiple times during the cleaning intervention and throughout the aging process, thus ensuring a precise assessment of the effectiveness of the treatment and long-term stability.

8.1.1 Samples preparation

Two sets of samples were prepared by deposition of Paraloid® B72 and Egyptian blue layers on glass microscope slides to replicate typical stratigraphies encountered in conservation.

The layer structure of the two sets is illustrated in Fig. 8.1.

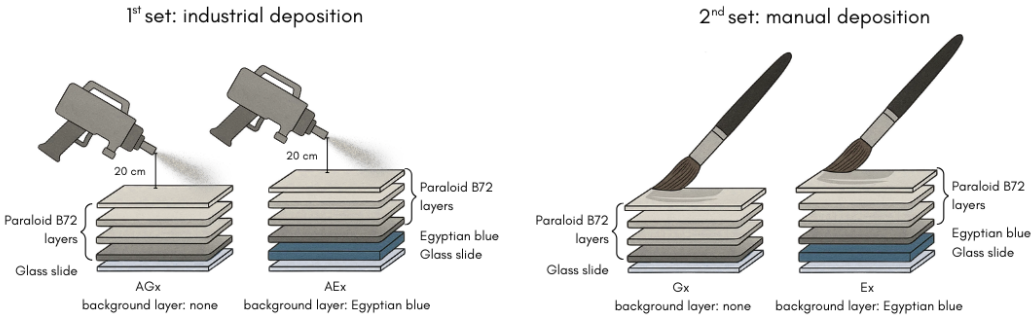

Fig. 8.1 Schematic of the fabrication process of the two sets of samples, performed by industrial deposition (1st set) and manual brushing (2nd set) respectively.

The first set aimed at providing a reference with controlled conditions, while the second one used to validate the calibration process in a nearly real case.

In the first set (Fig. 8.1, left) Paraloid® B72 was deposited using an industrial-grade professional sprayer onto both glass microscope slides and compressed tablets of Egyptian blue pigment. The sprayer was maintained perpendicular to the surface at a fixed distance of 20 cm, and coating thickness was verified with a coating thickness gauge. The resin solution was prepared at 20% v/v in acetone (70:30 acetone:Paraloid® B72). The subset of samples with Paraloid® B72 applied directly on a glass slide would be used to analyze the behavior of OCT in the case of single material. In the case of the second subset (labeled as AEx), to reduce porosity, Egyptian blue powder (Kremer pigment no. 10060) was mechanically grounded and compressed into tablets without binders. For each substrate (glass and pigment), the deposition of Paraloid® B72 was repeated up to 5 times, creating a different resin layer thicknesses.

The second set (Fig. 8.1, right) consisted of manually deposited samples to simulate real-world manual applications. Paraloid® B72 was mixed in acetone (20 vol% v/v) and then applied by repeated brushing to obtain samples with multiple layers of different thicknesses. Also in this case, two subsets were prepared: the

first one with Paraloid® B72 directly deposited on the microscope slides, while the second having a background layer of Egyptian blue. For the preparation of the latter, Egyptian blue pigments in a water solution of Arabic gum (10% vol.) were manually applied on the microscope slides, producing a layer of about 1 mm. The brushing technique and the use of Arabic gum simulate traditional artistic practices. This second set was used to validate the calibration on samples with more realistic variability in surface morphology and resin distribution.

The pigment layers in both sample sets were not standardized in thickness, as they were largely thicker than the OCT penetration depth and thus did not interfere with the measurement of the varnish layers. No binder (e.g., Arabic gum) was added during the preparation of the compressed pigment tablets, since the pigment was used only as an inert substrate. As the calibration procedure targeted the varnish layer, variations in pigment thickness or composition behind it had no influence on the reliability of the results.

Fig. 8.2 shows an example of the stratification obtained in the samples form the second sets with Paraloid® B72 deposited on a background layer of Egyptian blue.

Fig. 8.2 Example of the stratification obtained in the samples form the second sets with Paraloid® B72 deposited on a background layer of Egyptian blue

8.1.2 OCT acquisition

The measurements reported were performed with a Lumedica budget instrument [64]. The system exploits the spectral domain optical coherence tomography scheme (SD-OCT) and is equipped with a broadband source at 840 nm, yielding an output power of just 750 µW, that can be considered non perturbing even for light-sensitive materials.

The system shows a depth resolution of 7 µm in air and of 5 µm in tissues, with a transverse resolution of 15 µm. The cross-section of the sample is shown in a gray color scale: bright white corresponds to an higher reflection/scattering of the light,

while gray and darker white corresponds to a lower reflection/scattering. The dark areas of the image indicate a transparent media at the measurement wavelength (e.g. clear varnishes, air or glass) or a section that is beyond the penetration depth of light.

It is important to notice that the distances reported on the OCT images are optical distances, e.g. they depend both on the real thickness and on the refractive index of the measured layer. Therefore, in order to measure the actual thickness of each layer some adjustments must be done [14] relying on a preliminary calibration performed on reference samples that exhibit layers of known material and thickness. In other words, OCT shows different depth measurements depending on the refractive index n of the material under analysis. If the measurement is through air ($n = 1$), the depth measurement corresponds to the actual depth, while it is magnified when the medium has $n > 1$.

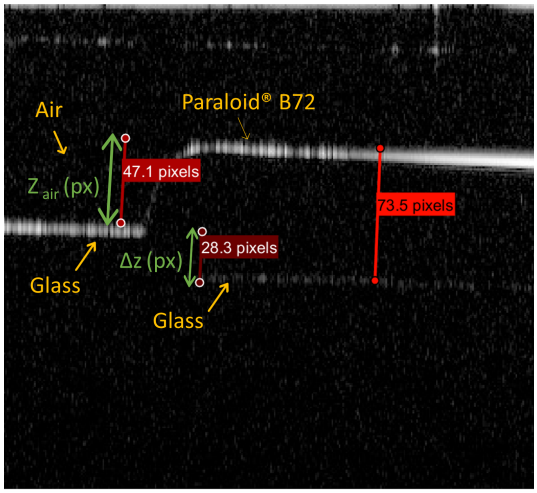

Fig. 8.3 OCT image acquisition of sample G5 at the interface between glass and Paraloid® B72 layer. The image depicting the artifact of non-flat glass surface that is caused by the varnish, can be used to evaluate the refractive index of the deposited layer and to measure subsequent samples containing Paraloid® B72 layers.

The acquired image of the Lumedica OCT system has 512 pixels depth and, as explained before, each pixel corresponds to a different depth in µm according to the refractive index of the material. In the case of air each pixel corresponds to 5.71 µm, meaning that the OCT has a maximum penetration of 2.92 mm in air. For example, with reference to Fig. 8.3, if Z_{air} is the optical thickness measured in air (i.e., considering $n = 1$) of the Paraloid® B72 layer in pixels, the conversion into the actual thickness T_{air} in µm is:

$$T_{\text{air}}(\mu\text{m}) = 5.71(\mu\text{m/px}) \cdot Z_{\text{air}}(\text{px}) \tag{8.1}$$

where 5.71 is the calibration factor of that OCT instrument.

Eq. 8.1 is specific for the thickness measurement in air and can be generalized to T_{RI} in Eq. 8.2 for a generic refractive index, measuring Z_{RI} (in pixels), which takes into account Z_{air} and the difference Δz (see Fig. 8.3) between the optical thickness in air ($n = 1$) and in another media ($n > 1$).

$$T_{\text{RI}}(\mu\text{m}) = \frac{5.71(\mu\text{m/px}) \cdot (Z_{\text{air}} + \Delta z)(\text{px})}{n} \tag{8.2}$$

where

$$Z_{\text{air}} + \Delta z = Z_{\text{RI}} \tag{8.3}$$

Starting from the information provided in Fig. 8.3 and using Eq. 8.1 and Eq. 8.2, it is possible to find that Paraloid® B72 has $n = 1.487$, in good agreement with the values reported in the literature [71] [72].

Every sample was analyzed with the OCT and then the recovered thickness values were compared with the reference thicknesses, both obtained during the deposition and from SEM images, to validate the reliability of the OCT system during cleaning of artifacts.

The OCT images were acquired and processed in MATLAB®, exploiting the image processing toolbox. Each image has been measured three times to have a minimum number of data to assess the accuracy of the measurement and uniformity of deposition. Once every sample had been measured in pixel, Eq. 8.2 was applied on the mean value in pixel to obtain the thickness value in µm. The results for the measurements before and after the conversion are reported in Fig. 8.4.

When comparing the two sets, a clear difference in deposition method emerges: the first subset, obtained using the industrial sprayer, shows a minimum layer thickness of approximately 20 µm, indicating a more controlled and uniform application. In contrast, the second subset, obtained via manual brushing, presents a thicker and more irregular layer, with an average thickness around 35 µm.

The difference of thickness between the two types of substrates is partially due to the fact that the application of the varnish were performed manually, so the results can differ from sample to sample and even among different areas of the same sample.

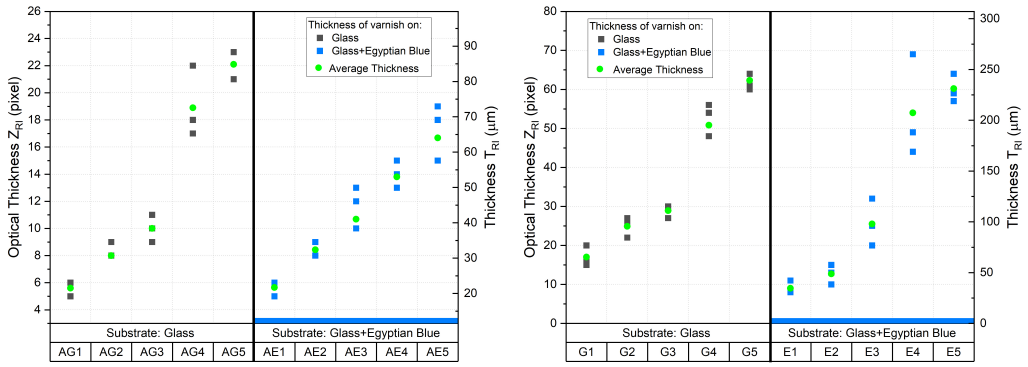

(a) First set: samples with layers deposited by an industrial sprayer

(b) Second set: samples prepared by manual brushing.

Fig. 8.4 Thickness measurement of first and second set of samples. The optical thickness of the varnish is reported in px on the left y scale, while the actual thickness in µm is displayed on the right y scale. The x axis reports the samples codes and their substrate structures NOT on scale.

The second explanation is given by the fact that the Egyptian blue is porous and absorbs the liquid varnish applied on it; this can be seen in Fig. 8.5b where the Paraloid® B72 partially coincides with the Egyptian blue substrate, while in Fig. 8.5a the Paraloid® B72 is well separated from the glass substrate.

Taking into account only the case of industrial deposition of Paraloid® B72 directly on glass the thickness does not have a linear increment with the number of layers, this is due to the surface tension and poor adhesion that produce a shrinkage of the varnish and a spurious assembling of material at the center of the glass, where the measure takes place. On the other hand, samples AE1-AE5 deposited on Egyptian blue show better adhesion and improved uniformity, as demonstrated by the nearly linear increment of thickness as a function of the number of layers. This does not hold for the second set: even for samples E1-E5 the adhesion to the hand-brushed Egyptian blue is lower. Both deposition processes of Paraloid® B72 were performed using a "wet-on-dry" technique, where the first layer of Paraloid® B72 was allowed to dry before the next layer was applied.

The porosity of the material can be a problem during the usage of the OCT in “real life” since the detection of slim varnish layers can be tricky for a non-expert user. The two layers looks like a single one at first sight (Fig. 8.5b), while a more accurate analysis can highlight that some more luminous particles are present on the

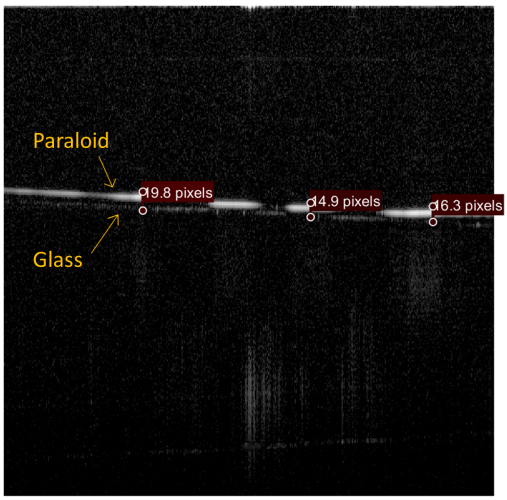

(a) Example of OCT image acquisition of sample G1.

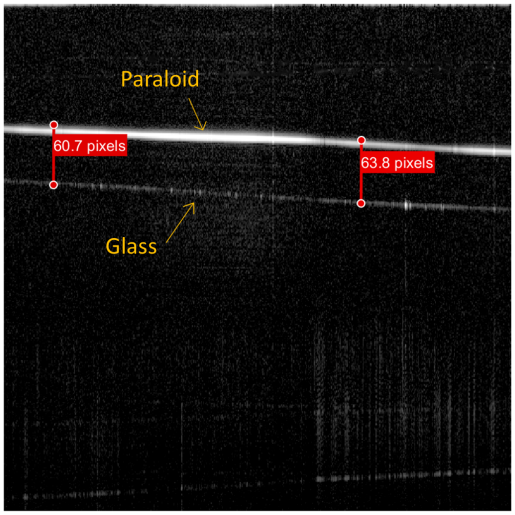

(c) Example of OCT image acquisition of sample G5.

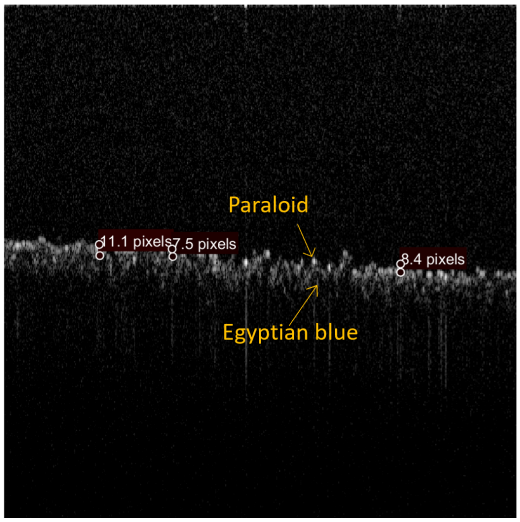

(b) Example of OCT image acquisition of sample E1.

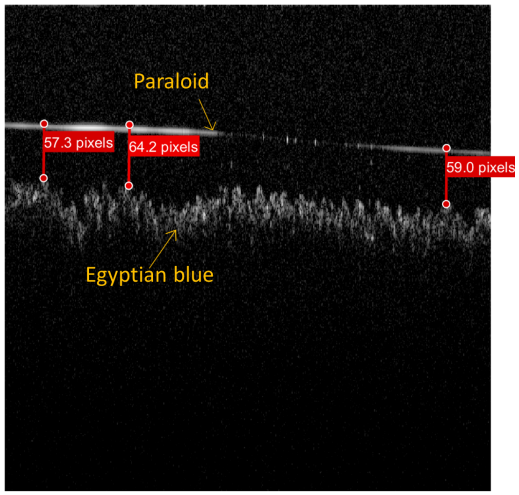

(d) Example of OCT image acquisition of sample E5.

Fig. 8.5 Example of OCT image acquisition of the second set of samples.

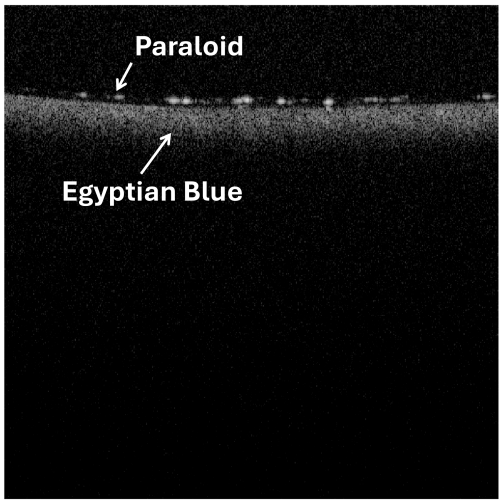

Fig. 8.6 Example of OCT image of the 1st set of samples (AE3).

top of the layers: those are the varnish layer quite completely superimposed to the Egyptian blue substrate.

The OCT measurements for the first set of samples were compared to those from the coating thickness gauge (Erichsen, Wet Film Thickness Gauge Model 333, Measuring range 0-120 µm, Read-off accuracy 5 µm). Fig. 8.6 shows the OCT image of sample AE3, showing both the Egyptian blue layer and three Paraloid® B72 layers. The varnish layer is well detectable and the interface with the substrate is clear and smooth, whereas the interface with the glass substrate is masked by the absorbing Egyptian blue.

8.1.3 OCT vs coating thickness gauge

Fig. 8.7 reports the comparison between the OCT and the coating thickness gauge measurements: a maximum deviation of 12 µm occurs on the samples with Paraloid® B72 directly on glass because it is susceptible to shrinkage and produces areas of non-uniform varnish distribution.

This effect is also observable on AE1-AE5 samples that have the varnish deposited on the compressed tablets of Egyptian blue that also enhances the surface tension effect. The results are satisfactory, considering the lack of information on uncertainty of the coating thickness gauge, which only provides the nominal value.

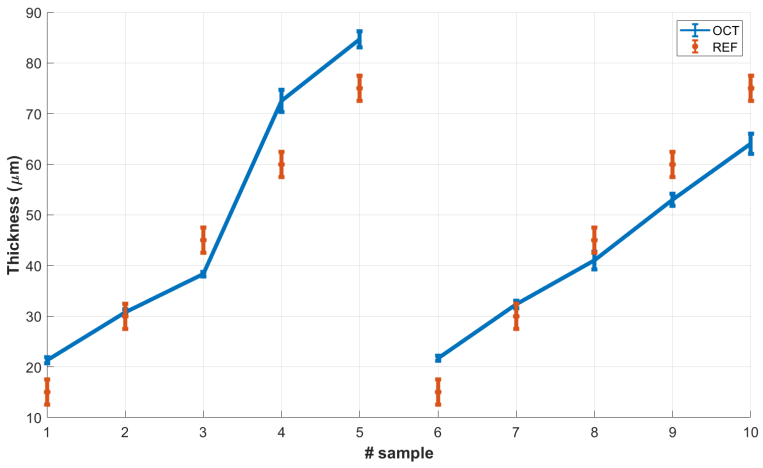

Fig. 8.7 Comparison of the thickness of the Paraloid® B72 layer measured by OCT with the reference (coating thickness gauge) for the first set of samples (deposited by an industrial sprayer).

8.1.4 OCT vs SEM

To validate the OCT's performances in a real artifact removal setting, its measurements were compared against the data from the second set of samples, i.e. fabricated by manual deposition of pigment and varnish, with those obtained by Scanning Electron Microscope (SEM) (Zeiss Supra40 Field Emission Scanning Electron Microscope), which would be used as a reference. After acquisition of OCT images, each sample was sharp cut at 1 cm from the edge, paying attention to preserve the cross section. The cut-off interface has been coated by an electrically-conducting platinum thin film (about 10 nm), which does not interfere with the measurement of the layer thickness, but allows to enhance the contrast of the image. As an example, Fig. 8.8 reports a cross-section image of the E5 sample. The interface between the Paraloid® B72 and the Egyptian blue layers is observable as the varnish appears more compact and smooth than the pigment.

Fig. 8.5d shows the correspondent OCT image along with those of samples G1, E1 and G5 (Fig. 8.5a, 8.5b, 8.5c). Samples G1 and G5, exhibit a more uniform thickness due to the flatness of the supporting glass surface.

Fig. 8.9 compares the thickness measurements from OCT and from SEM. Because access to the SEM was limited, the analysis was restricted to a small number of samples. Fig. 8.9 highlights, for a given number of varnish layers, that samples with

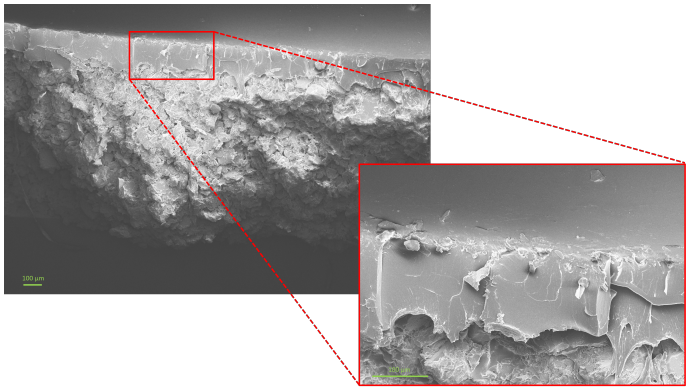

Fig. 8.8 SEM image of the cross-section of sample E5 with the detail of the Paraloid® B72 layer. From top: Paraloid® B72 and Egyptian blue layers on the glass substrate (not visible in the picture). The Paraloid® B72 layer thickness is estimated to be 203.4 µm.

the Egyptian Blue substrate exhibit a lower thickness of Paraloid® B72 compared to those with glass substrate. This difference is mainly due to compression during the glass slide cutting process.

The OCT measures exhibit a larger error bar than those measured from SEM images, in particular for the samples containing the Egyptian blue pigment. This is mainly due to the porosity of the pigment layer, which causes an absorption of the varnish into the pigment layer. This effect is evident in Fig. 8.5b, where the Paraloid® B72 shows partial diffusion into the Egyptian blue substrate (gets blurred at the interface with the pigment layer), while in Fig. 8.5a no diffusion into the glass substrate is observed.

It is important to note that no significant swelling (i.e., macroscopic volume expansion) of the varnish layer was observed; the reduction in apparent thickness is only due to the absorption of Paraloid® B72 into the pores of the pigment. The porosity of Egyptian blue is further highlighted by comparing Fig. 8.5b and Fig. 8.6, where in the second one the pigment layer (i.e., the lower one) is more compact than the corresponding one in the first image. The porosity of the material can be challenging when using OCT in real-case applications, since identifying thin varnish layers on porous substrates can be challenging for untrained operators. However, a careful inspection can still identify the varnish by the presence of a denser distribution of bright spots above the pigment layer, as shown in Fig. 8.5a.

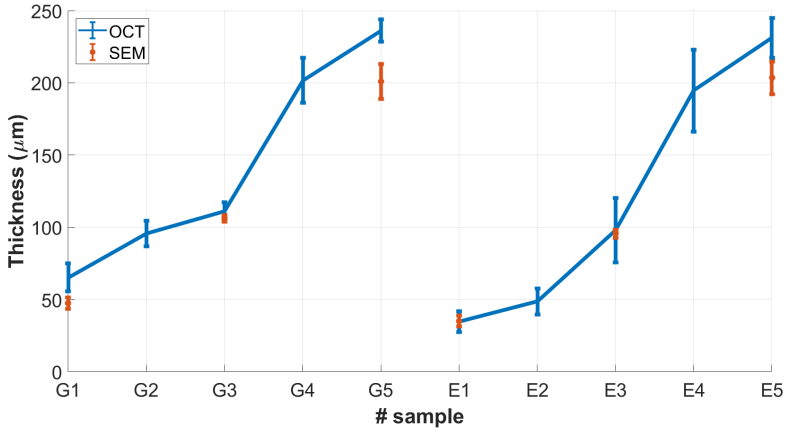

Fig. 8.9 Comparison of the thickness of the Paraloid® B72 layer measured by OCT and SEM for the second set of samples.

In conclusion the thickness values obtained through OCT imaging were compared to reference data acquired via SEM and coating thickness gauges. The absolute error ranged from 0.5 µm to 30.2 µm (for a thickness value of about 230 µm), depending on layer homogeneity and thickness. A Pearson correlation analysis revealed a statistically significant correlation ($r = 0.991$), supporting the accuracy of the low-cost OCT device to measure the layers of transparent varnish. It should be noted that the comparison involves an inherent source of error related to the preparation of the samples for SEM analysis, as random compression of the layers may occur during cutting, as significantly recognizable in sample G5. Further investigations shall overcome this issue by implementing advanced sectioning techniques techniques, such as femtosecond laser cross-sectioning [73]. Overall, the comparison still supports the applicability of the OCT system for the analysis of artifacts and cultural heritage objects. Possibly the accuracy can be enhanced by complementing it with fluorescence analysis. Yet, the ability of OCT to perform non-contact, in situ measurements without any sample preparation strongly reinforces its potential for art conservation purposes.

8.1.5 Validation of the reliability of the OCT measurements of handcrafted samples

Measurement repeatability was evaluated through statistical analysis. For this purpose, 50 measurements were carried out on samples G4 and E4, and the correspond-

ing mean values and standard deviations were calculated. The 50 measurements were taken in 10 different areas of the sample, 5 images for each spot, to have a more representative case of practical applications in cultural heritage analyses.

As it can be seen from Fig. 8.10, the measurements differ one from the other, but this is mainly due to the inhomogeneity of the Paraloid® B72 film resulting in slightly different thicknesses in the different areas of the sample.

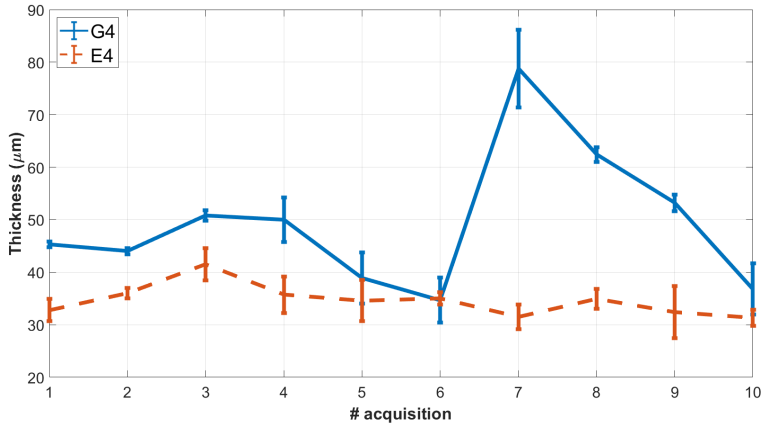

Fig. 8.10 Mean and standard deviation of Paraloid® B72 thickness on samples G4 and E4.

Sample G4 exhibits a larger variability due to the lack of homogeneity of the Paraloid® B72 film across the glass substrate. However, it is important to highlight that, for each acquisition, the spreading of the measurements is well within acceptable ranges for the intended application. This means that the thickness of the Paraloid® B72 layer can be measured with enough accuracy within the small acquisition area of the OCT (7 mm).

8.2 OCT image segmentation

Since the measurement process is quite long and difficult to be performed manually, an image segmentation algorithm can be implemented in order to speed up the measurement process. The automatic evaluation of the layer position and thickness enable a fully integrated analysis within the cleaning process without the need of additional time or operators to evaluate it.

In OCT images, the cross-section of the sample is typically represented in a grayscale color map, where:

- bright white corresponds to an higher reflection/scattering of the light,
- gray and darker white corresponds to a lower reflection/scattering,
- dark areas corresponds to a transparent media at the measurement wavelength or a section beyond the penetration depth of light.

While this grayscale representation is intuitive and suitable for human interpretation, it poses several challenges for automatic processing. Specifically, the lack of well-defined boundaries or distinct intensity thresholds makes conventional image processing techniques (e.g., edge detection, thresholding, or morphological filtering) unreliable without manual intervention. For this reason an approach purely based on traditional image analysis tools, such as the one presented in the previous section, is not useful without the human intervention and cannot guarantee robust or repeatable results across different samples or imaging conditions.

To overcome this limitations a data-driven method based on image segmentation can be adopted. Such algorithms can learn to identify and delineate the various layers within the OCT images directly from labeled examples, even when the contrast or texture differences between layers are weak. By training the segmentation model on a set of representative labeled images, it becomes possible to generalize the identification of layer boundaries in new, unseen samples, thus achieving a fully automatic and objective analysis.

The dataset available for this research consist of more than 10k images in-house from custom made samples. However, this dataset is currently unlabeled, which poses a limitation for supervised learning approaches. To mitigate this issue, a smaller

secondary dataset was identified online, containing 10 labeled ophthalmological OCT images that exhibit a similar layered structure.

Although these images differ in origin and content, they can be used as an initial reference or as a pretraining source to develop a preliminary segmentation model. Their labeled structure provides the foundation for building a network capable of recognizing layered patterns similar to those observed in the custom-made samples. To increase the effective size and diversity of this limited labeled dataset, data augmentation techniques can be applied. These operations artificially expand the dataset by generating modified versions of the existing labeled images, allowing the model to generalize better to unseen data and to become more robust to variations in acquisition conditions. The following augmentations were considered:

- Horizontal flips: Since the OCT images have a strong directional specificity, only horizontal flips were applied to maintain the physical consistency of the sample geometry.
- Noise injection: Gaussian noise was added to simulate real acquisition artifacts and improve the model's resilience to sensor or optical noise.
- Geometric transformations: Operations such as cropping, zooming, and stretching were used to increase variability in spatial scale and position of layers.
- Photometric adjustments: Modifications in contrast and brightness were performed to simulate changes in illumination or signal intensity.

An example of image augmentations is reported in Fig. 8.11. By applying these augmentations, the network is exposed to a broader range of conditions, which reduces overfitting and enhances generalization. However, even with augmentation, the small number of labeled samples constitutes a major limitation. To further address this challenge, a semi-supervised learning approach was implemented. This strategy takes advantage of both the limited labeled dataset and the much larger unlabeled dataset available from in-house acquisitions. The process consists of the following main steps:

- Supervised pretraining: A convolutional segmentation model is first trained on the small labeled dataset to learn the mapping between grayscale OCT inputs and their corresponding segmented output masks.

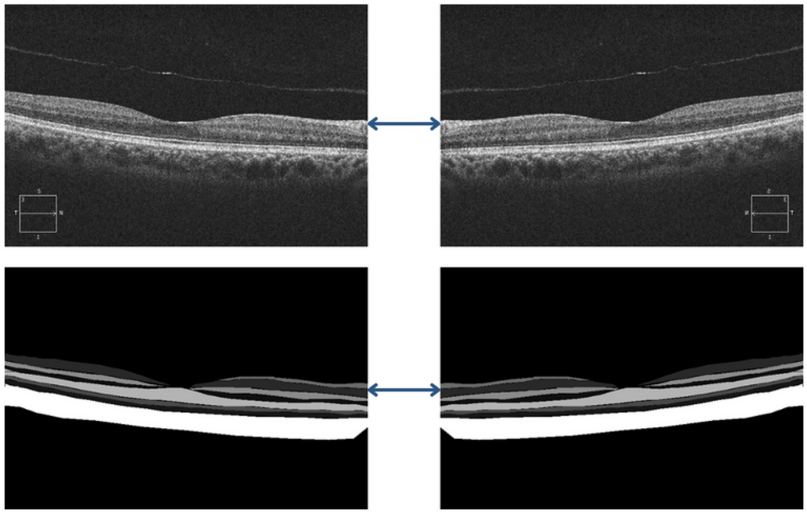

Fig. 8.11 Data augmentation (horizontal flip) example.

- Pseudo-label generation: Once the initial model achieves satisfactory performance, it is used to predict the segmentation maps of the unlabeled images. These predicted maps are used as pseudo-labels.
- Iterative retraining: The newly pseudo-labeled images are progressively added to the training set, and the model is retrained on this extended dataset. Through multiple iterations, the network improves its ability to detect and delineate layer boundaries even in unlabeled data.

This approach effectively exploits the large volume of available unlabeled data, allowing the model to continuously refine its segmentation capability while reducing the dependency on manual annotation.

As an initial implementation, a Convolutional Neural Network (CNN) based on the U-Net architecture was employed. U-Net is widely used in biomedical imaging due to its ability to perform fast and accurate pixel-level segmentation, even with a relatively small number of training samples. The U-Net consists of a contracting path that captures contextual information through successive convolution and pooling layers, and an expanding path that enables precise localization through up-sampling and concatenation with the corresponding feature maps from the encoder.

In this implementation, the input to the network consists of grayscale OCT images (Fig.8.12, left), while the output is the corresponding segmented mask (either

labeled or pseudo-labeled, Fig.8.12, right). Due to the very limited dataset size, the model was prone to overfitting, as expected, it began to overfit after approximately 200 training epochs when trained with only few images. To mitigate this, an early stopping criterion was applied, automatically stopping the training process once the validation loss stopped improving.

Even under these constrained conditions, the preliminary results were promising: the U-Net model achieved an accuracy of 96.22% on the labeled validation set. This result demonstrates that, despite the small dataset, the network was capable of learning meaningful structural information from the OCT images (Fig. 8.12).

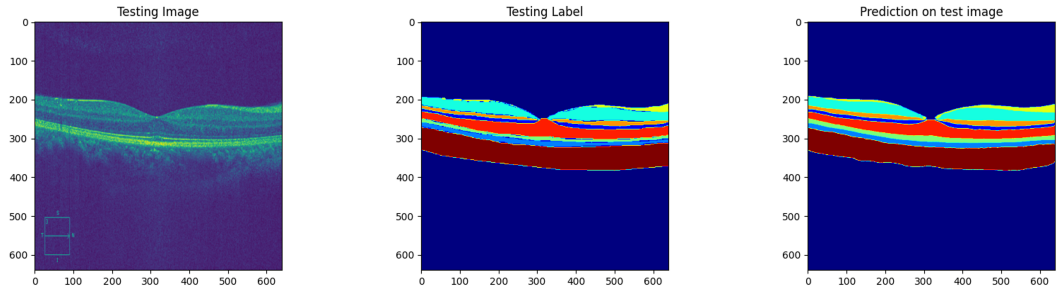

Fig. 8.12 Example of the input dataset (left and center) and example of the predicted mask after training (right).

Following this first experiment, the trained model was used to generate pseudo-labels for a subset of the in-house unlabeled images. The resulting predictions (Fig. 8.13) appeared consistent with the expected layer structures and showed potential for integration into the semi-supervised learning pipeline. With further optimization, such as fine-tuning the network hyperparameters, expanding the augmented dataset, and refining the pseudo-labeling strategy, this approach can be extended to automatically label the entire dataset and support a fully automated analysis workflow.

In summary, the combination of data augmentation, semi-supervised learning, and a U-Net-based segmentation model represents a promising framework for automating the evaluation of OCT layer structures. This strategy enables the effective use of limited labeled data, leverages the large pool of unlabeled samples, and lays the groundwork for future real-time integration into the measurement or cleaning processes.

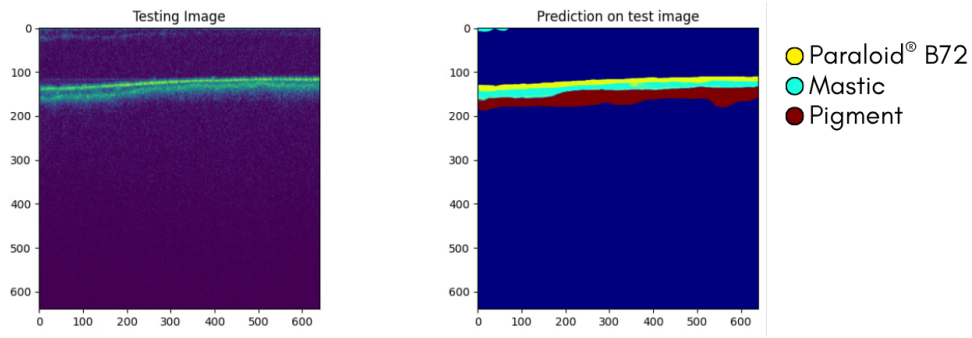

Fig. 8.13 Example of generated pseudo-labels (right) for a in-house unlabeled image (left).

8.3 Roughness monitoring

The measurement of an artifact's morphological characteristics is as important as the investigation of the thickness of its material layers. In recent years, the development of advanced three-dimensional acquisition and imaging technologies has provided new opportunities for the documentation and analysis of cultural heritage surfaces. Techniques such as photogrammetry, laser scanning, reflectance transformation imaging (RTI), and 3D microscopy allows to accurately describe the morphological features of objects at different precisions. However, these methods are limited to the investigation of superficial characteristics and do not allow the examination of sub-surface structures. This limitation is a critical issue in conservation practice, as the evaluation of roughness and morphological variations at the interface between the original material and the overlying layers is essential to reduce the effect of the cleaning on the material to be preserved. In this context, the use of non-invasive optical techniques such as OCT is a promising approach to extend roughness measurements beyond the visible surface. The measurements presented below aim to explore the potential of OCT for the characterization of both surface and sub-surface morphology.

A new series of samples was specifically prepared to investigate surface roughness through OCT. Egyptian blue pigment (Kremer Pigments No. 10060) was bound in a 10% v/v aqueous solution of Arabic gum brushed onto a microscope slides (2×2 cm). The sample was used as a reference to validate the OCT-based roughness measurements. A non-varnished sample was chosen to simplify the analysis, enabling direct assessment of the surface morphology at the air/color interface. This

avoided potential distortions caused by the presence of a varnish layer, both due to its refractive index differing from air and because it prevents direct comparison with SEM or profilometric techniques. All OCT measurements were performed on a selected region of the sample, characterized by moderate roughness and a regular surface profile, comparable to that typically found on real artefacts.

Roughness Measurement and Analytical Parameters

The profile method (line-based roughness analysis) was selected as the main validation approach for the OCT system, as it provides standardized and reproducible results in accordance with ISO 21920-3:2021. This method also enables direct comparison between OCT data and complementary techniques.

Average roughness (R_a) and Ten Points Height ($R_{z(ISO)}$) were chosen for quantification: the first one represents the mean magnitude of surface irregularities, while the second one indicates the mean distance between the five highest peaks and the five deepest valleys, often used to capture vertical extremes (Eq. 8.4) [74].

$$\begin{aligned} R_a &\approx \frac{1}{n}\sum_{i=1}^{n}|z_i| \\ R_{z(\mathrm{ISO})} &= \frac{1}{5}\left(\sum_{i=1}^{5}p_i + \sum_{i=1}^{5}v_i\right) \end{aligned} \tag{8.4}$$

Since R_a provides only an average magnitude of roughness without describing spatial variability, additional standardized parameters were included [74]: R_p (Maximum Peak Height) and R_v (Maximum Valley Depth), used for sub-surface roughness characterization.

8.3.1 Development of the Python-Based Roughness Analysis Algorithm

Also in this case, measurement process is quite long and difficult to be performed manually. A dedicated Python script was developed to automate the extraction of roughness parameters from OCT B-scan profiles. The validation of the algorithm was performed by comparing its results with manual measurements on a subset of

images. Manual roughness measurements were conducted by selecting N significant points along the air–color interface using ImageJ, evaluating the vertical deviation of approximately 70 points in the reference area (Fig. 8.14).

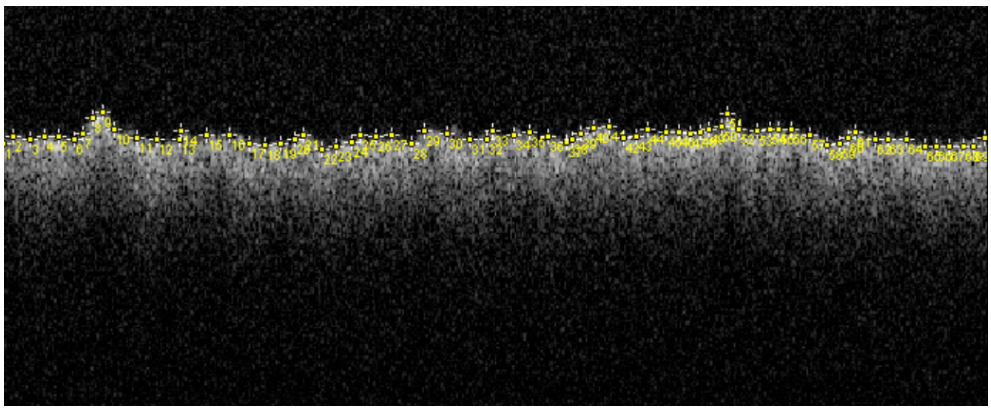

Fig. 8.14 Manual roughness measurements conducted by selecting ≈70 significant points along the air–color interface.

The automated algorithm replicated this process in a fully reproducible and automated way. It imports grayscale images (Fig. 8.15a), crops borders, enhances contrast (histogram equalization), and applies Gaussian filtering to reduce noise. A binary threshold isolates the interface region (Fig. 8.15c); the image is inverted and contours extracted with OpenCV.

However, it is important to note that this script must be used in combination with the image segmentation model described in the previous section. The segmentation model is essential to correctly isolate the relevant interface when multiple layers are present, for example, when a resin coating covers the colored layer. The roughness extraction algorithm alone only detects the uppermost visible boundary, and would therefore measure the surface of the resin rather than the color layer beneath it. The combination of the two algorithms ensures that the correct interface is analyzed in any case.

For each x-coordinate, the algorithm extracts the minimum y-value (highest point), reconstructing a discrete surface profile. After inverting the y-axis for physical orientation, the height profile is saved as a text file. From this, roughness parameters (R_a, R_z, R_p, R_v) are computed and recorded in CSV format. Visual verification is provided by overlaying the detected boundary on both the original (Fig. 8.15b) and binary (Fig. 8.15d) images, and by exporting the extracted profile plot (Fig. 8.16).

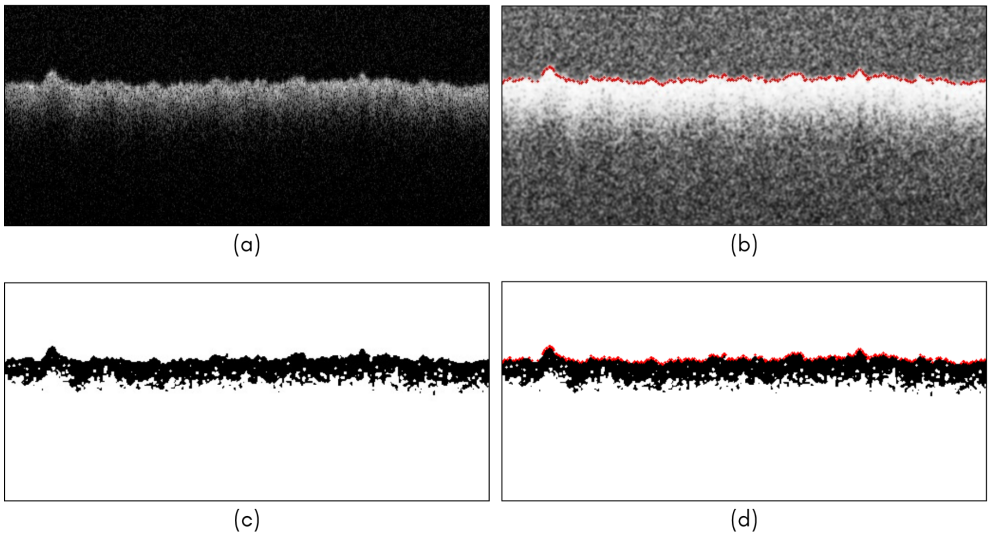

Fig. 8.15 OCT image: original(a) and binary (c). Reconstructed discrete surface profile on the original image (b) and on the binary one (d)

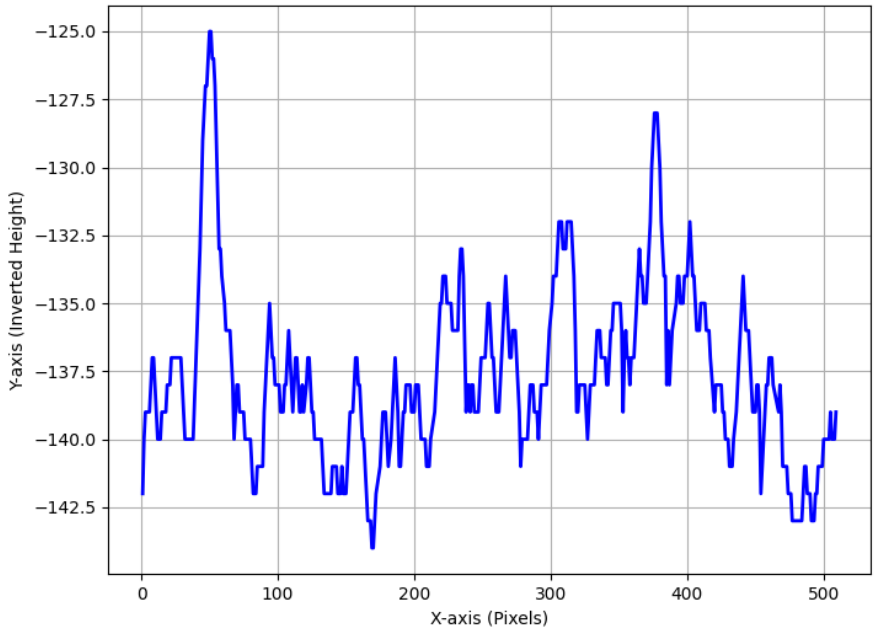

Fig. 8.16 Reconstructed surface profile.

This automated workflow significantly increases efficiency and consistency, reducing analysis time for a 512 images volume from approximately 25 min (manual) to 4.3 s (automated), a reduction exceeding 99%.

8.3.2 Comparison with Reference Measurements

Reference measurements were acquired using a contact roughness meter on five lines across the sample to establish baseline values (Tab. 8.1) and to better interpret the results gained by means of non-direct measurements (i.e., SEM and OCT).

Parameter	L1 (µm)	L2 (µm)	L3 (µm)	L4 (µm)	L5 (µm)	Mean value (µm)	St. Dev. (µm)
R_a	6.68	7.11	8.31	6.70	7.99	7.36	0.75
R_z	41.14	39.95	44.05	41.00	54.51	44.13	5.99
R_p	15.82	14.60	17.56	16.08	18.40	16.49	1.50
R_v	23.31	25.34	26.50	24.92	36.11	27.24	4.77

Table 8.1 Roughness parameters measured at five different locations with a contact roughness meter (L1 to L5).

The results confirm a uniform R_a across the area, with greater variability in R_v linked to brush-stroke patterns. Line 5 (L5) presents deeper valleys, likely corresponding to regions with minimal pigment, resulting in higher R_z value.

Before contact measurements, non-contact analyses (OCT and SEM) were performed to avoid potential surface damage. Mean SEM and OCT parameters derived from the automated algorithm are summarized in Tab. 8.2 with the mean values from the contact roughness meter.

Comparative analysis reveals that OCT consistently yields higher roughness values than SEM, particularly for R_z values. OCT measures roughness values approximately twice as high both for R_a and for R_z. When compared to contact roughness meter data (Tab. 8.2), both non-contact techniques show compatibility with the gold standard: OCT tends to overestimate, while SEM underestimates roughness parameters.

The differences can be due to the distinct vertical resolution and filtering characteristics of each method. OCT's axial–lateral resolution and surface approximation may cause minor overestimation, whereas SEM, particularly at lower magnifications, may lose height detail.

Interestingly, the higher R_p values obtained by OCT indicate its sensitivity to peak detection, potentially capturing features missed by the contact method. This

Parameters	**Roughness meter** (μm)	**SEM** (μm)	**OCT** (μm)
R_a	7.36 ± 0.75	5.93 ± 2.42	9.33 ± 2.72
R_z	44.13 ± 5.99	29.23 ± 11.62	57.21 ± 14.81
R_p	16.49 ± 1.50	–	31.89 ± 2.01
R_v	27.63 ± 4.77	–	32.95 ± 8.29

Table 8.2 Mean values comparison for the parameters acquired with the three measurement systems (Roughness meter, SEM and OCT).

aligns with observed surface abrasion effects, which might reduce peak prominence in the contact measurements.

Overall, the results can be considered encouraging. Even if the accuracy of OCT measurements does not reach that of direct contact roughness methods, the technique proves useful for the intended applications. The preliminary findings demonstrate that OCT can provide fully non-invasive information on the sub-surface roughness of varnished painted surfaces. Moreover, its applicability to real-case scenarios suggests that OCT is a feasible tool for monitoring the entire cleaning or conservation process, enabling quantitative assessment without risking damage to the artwork.

Chapter 9

Fluorescence spectroscopy

Fluorescence spectroscopy has become an increasingly valuable tool in the scientific analysis of cultural heritage materials: can be regarded as complementary optical tools for the characterization of surface coatings and varnish layers. While OCT provides depth-resolved structural information with micrometric resolution, its sensitivity may decrease in transparent or weakly scattering layers where the refractive index contrast is low. In such cases, fluorescence emission offers an alternative contrast mechanism that is highly sensitive to the optical absorption and thickness of the material.

This approach is particularly useful in the field of cultural heritage diagnostics, where direct sampling of the surface is often forbidden. Optical methods based on fluorescence emission, combined with reflectance and OCT models, allow for a quantitative, contactless characterization of protective coatings applied over pictorial layers. Understanding the optical response of these stratified systems enables conservators to assess the effectiveness, homogeneity, and aging state of varnishes without altering the original artwork.

The intensity and spectral profile of the emitted light depend on the excitation wavelength, the absorption coefficient, and the quantum yield of the fluorescent species. In the context of cultural heritage, many protective coatings, synthetic resins, and pigments exhibit intrinsic fluorescence in the visible or near-infrared region, which can be detected and quantitatively analyzed.

Compared to OCT, fluorescence-based techniques provide complementary contrast and sensitivity to molecular composition and optical absorption, making them

particularly useful when structural interfaces are not clearly resolved by interferometric imaging. Furthermore, fluorescence can be combined with reflectance or transmittance measurements to decouple the effects of absorption, reflection, and emission, enabling a more comprehensive description of multilayer systems such as varnish–pigment composites.

In this chapter, a fluorescence modeling and optimization framework is presented to simulate and analyze the optical behavior of stratified systems representative of painted surfaces. The approach combines reflectance fitting, used to estimate the optical parameters of each layer, with a fluorescence emission model that accounts for absorption, transmission, and re-emission processes. This methodology allows the non-destructive estimation of varnish thickness and provides an interpretative link between experimental fluorescence data and the physical properties of the coating.

9.1 Experimental analysis

To validate the modeling approach, an experimental measurement campaign was carried out on reference samples (see Ch. 8.1.1 for details) representative of painted surfaces. The purpose of these measurements was to acquire reflectance and fluorescence data under controlled conditions, for the extraction of the optical parameters of each layer.

The experimental data thus obtained served a dual purpose: first, to extract and calibrate the optical parameters used in the reflectance fitting procedure; and second, to test the predictive capability of the fluorescence emission model in reproducing the observed intensity–thickness relationship. This combined validation approach ensured that the numerical model accurately reflects the physical processes occurring within the stratified media and can be reliably applied to the non-invasive estimation of varnish thickness on real cultural heritage surfaces.

The experimental setup was designed to enable the simultaneous acquisition of reflectance and fluorescence signals from multilayered samples representative of painted cultural heritage surfaces. The system consisted of an optical bench with a broadband LED, a spectrometer unit, and a positioning stage for precise control of the measurement position. Excitation was provided by a broadband light source between 400 and 800 nm, selected to efficiently excite the characteristic

near-infrared fluorescence of the Egyptian Blue pigment under the Paraloid® B72 layer. The incident beam was directed onto the sample at normal incidence at a distance of ≈1 mm to simplify the interpretation of the reflectance data and to ensure homogeneous illumination over the sampled area. The emitted and reflected light were collected through an optical fiber bundle connected to the spectrometer. Fig. 9.1 shows a detail of the acquisition setup.

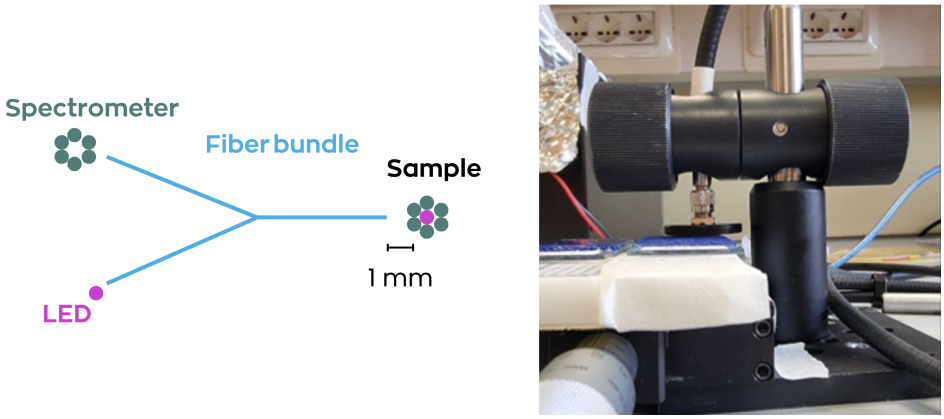

Fig. 9.1 Fluorescence acquisition set-up.

All measurements were carried out under controlled ambient conditions to minimize the influence of unwanted light and temperature fluctuations. For each varnish thickness (see Ch. 8.1.2, second sample set deposited on Egyptian blue), five acquisition were done across the sample surface to take into account inhomogeneities in layer deposition. The resulting spectra were averaged to obtain representative reflectance and fluorescence profiles for each sample.

The experimental data were preprocessed: the curves were normalized with respect to their maximum intensity to emphasize the shape and relative evolution of the signal as a function of varnish thickness and background subtraction was applied to remove any unwanted contribution.

The final results are presented in Fig. 9.2: the evaluation of both fluorescence and absorbance signals was performed to quantitatively characterize the optical response of the multilayer system and to establish a reliable link between experimental data and model parameters. In particular, five spectra for each sample have been acquired to monitor the stability. Specifically, the fluorescence intensity was analyzed at 900 nm (Fig. 9.2, red dots), corresponding to the main near-infrared emission band of Egyptian Blue, while the absorbance was evaluated at 660 nm (Fig. 9.2, black

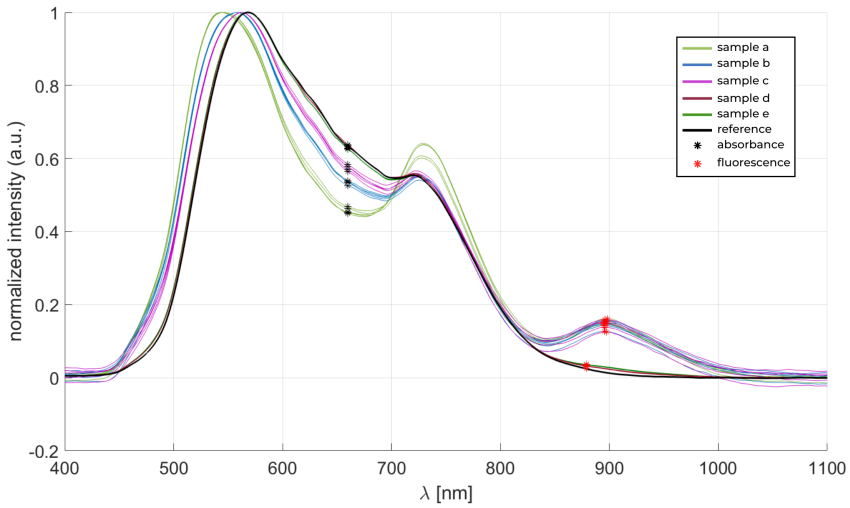

Fig. 9.2 Spectral evaluation of both fluorescence (red) and absorbance (black) signals performed to quantitatively characterize the optical response of the layers.

dots), where the absorption of the varnish and pigment layers is most significant. The absorbance values were extracted from the reflectance spectra according to the relation $A = 1 - R$, where R is the normalized reflectance, allowing the estimation of the optical attenuation due to both absorption and scattering processes within the stratified medium.

The summary of the absorption (red dots) and fluorescence (blue dots) data, including the mean value for each sample, is presented in Fig. 9.3.

By considering only the absorption component (Fig. 9.4), a clearly monotonic trend can be observed, indicating a strong correlation between the measured absorption intensity and the varnish layer thickness. This consistent behavior suggests that absorption can be used as a reliable parameter for estimating the thickness of the varnish and, when combined with an appropriate optical model, can also provide insight into the intrinsic optical properties of the constituent materials, such as their absorption and scattering coefficients.

Also, considering the fluorescence (Fig. 9.3, blue dots) a similar monotonic trend can be observed, reflecting the same general dependence on the varnish layer thickness. However, the fluorescence response seems to be less sensitive to thickness variations compared to the absorption behavior. Nevertheless, with an appropriate calibration procedure, the fluorescence intensity can still be employed as a

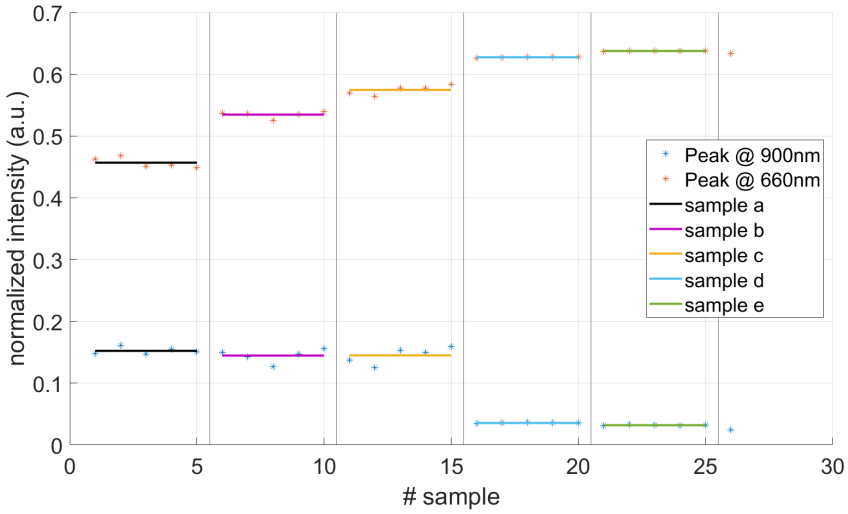

Fig. 9.3 Evaluation of fluorescence (blue) and absorbance (orange) intensities, with the mean value reported for each thickness.

complementary parameter for estimating layer thickness and assessing the optical characteristics of the surface materials, as explained in Sec.9.2.2.

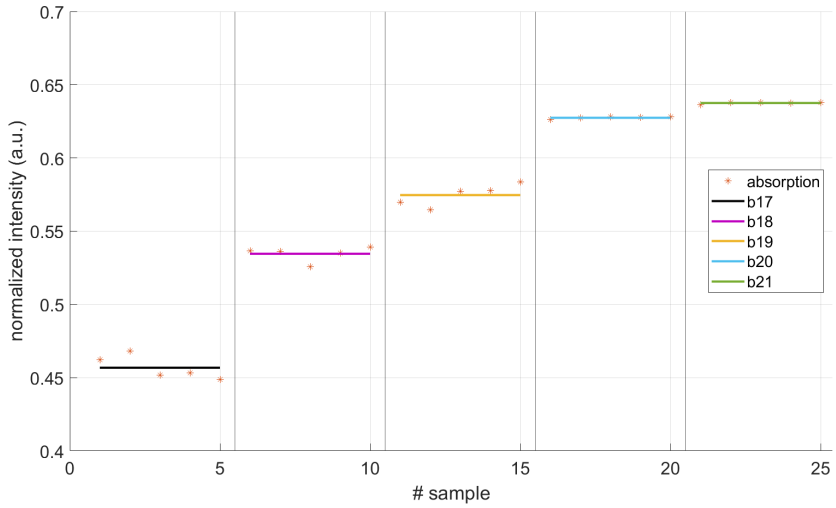

Fig. 9.4 Absorbance intensities, with the mean value reported for each thickness.

9.2 Simulation analysis

The focus now is to characterize the optical properties of the protective varnish layer (Paraloid® B72) applied over the pigment (Egyptian Blue).

The first section aims to determine the optical parameters of the Paraloid® B72 (α_p, n_2) and the underlying Egyptian blue (n_3) by fitting a theoretical reflectivity model to experimental data collected at various Paraloid® B72 thicknesses (Sec. 9.1).

9.2.1 Theoretical reflectivity model/parameter estimation

The optical response of cultural heritage materials coated with varnishes or protective layers can be accurately described using stratified media models, where each layer is characterized by its complex refractive index and absorption coefficient. In the simplest configuration, the system consists of three media (Fig. 9.5):

- Air (n_1)
- Paraloid® B72 (n_2)
- Egyptian blue ($n_3 = n_3' + ik_3$)

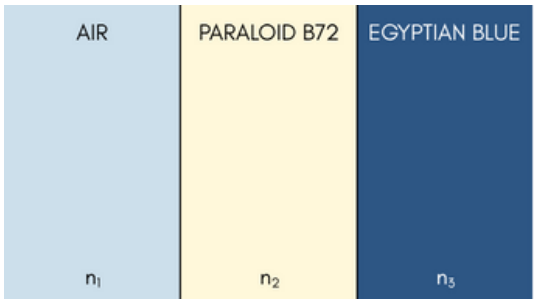

Fig. 9.5 Schematic illustration of the three layered structure.

According to Fresnel's equations (Eq. 9.1), at each interface part of the incident light is reflected (R) and part is transmitted (T):

$$R_{ij} = \left|\frac{n_i - n_j}{n_i + n_j}\right|^2$$
$$T_{ij} = 1 - R_{ij} \tag{9.1}$$

If the varnish has a finite thickness L, the light propagating in it undergoes an exponential attenuation due to absorption, according to Beer-Lambert law (Eq. 9.2):

$$I(z) = I_0 e^{-\alpha z} \tag{9.2}$$

where α is the absorption coefficient of the varnish (m^{-1}), and z is the distance from the air/varnish interface.

The total reflectance of the system can be expressed as the sum of multiple internal reflections occurring at the interfaces (see Fig. 9.6), attenuated by the absorption of the varnish layer.

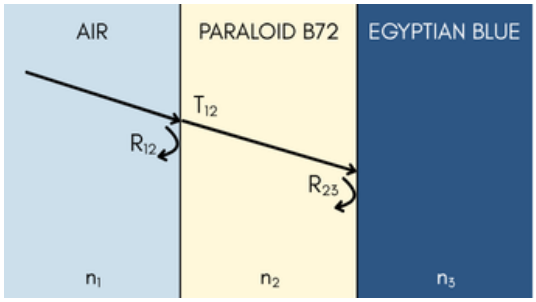

Fig. 9.6 Schematic illustration of the three layered structure with the internal reflections occurring at the interfaces.

Assuming that the varnish layer is weakly absorbing Eq. 9.3 expresses the total reflectance of the system.

$$R(L) = R_{12} + (1 - R_{12})^2 R_{23} \frac{e^{-2\alpha L}}{1 - R_{12} R_{23} e^{-2\alpha L}} \tag{9.3}$$

where R_{12} and R_{23} are the Fresnel reflectances at the first and second interfaces and α and L are the absorption coefficient and the thickness of the varnish.

By substituting Eq. 9.1 and Eq. 9.2 in Eq. 9.3 for each material the theoretical reflectance is obtained (Eq. 9.4):

$$R_{\text{model}}(L_p; \mathbf{p}) = R_{12} + \frac{(1 - R_{12})^2 R_{23}\, e^{-2\alpha_p L_p}}{1 - R_{12} R_{23}\, e^{-2\alpha_p L_p}}, \tag{9.4}$$

with the parameter vector defined as

$$p = [\alpha_p,\ n_2,\ n_3,\ k_3] \tag{9.5}$$

This formulation includes the effect of multiple reflections and exponential attenuation, making it suitable for films of medium/large thickness, where internal reflections cannot be neglected.

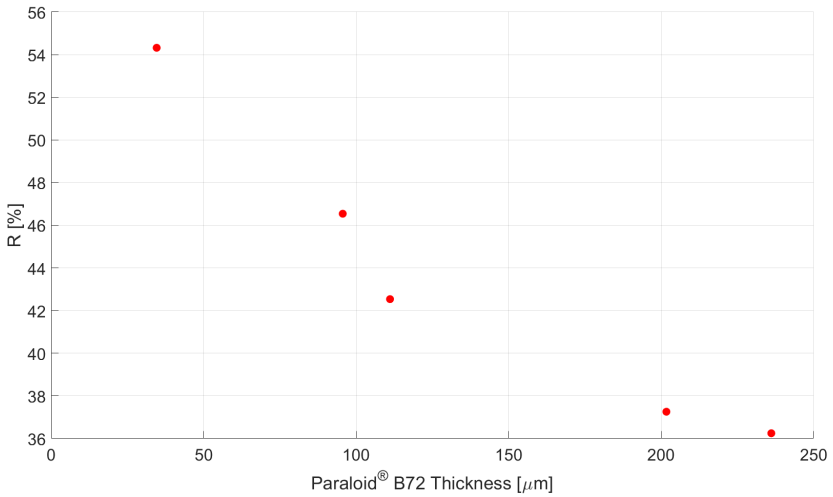

Fig. 9.7 Experimentally acquired reflectance data as a function of thickness.

To find the parameters that best reproduce the experimental reflectance data (Fig. 9.7), a least-squares minimization is performed. The cost function is defined in Eq. 9.6 and quantifies the total deviation between the model and the experimental measurements.

$$J(\mathbf{p}) = \sum_{i=1}^{N} \left[R_{\text{model}}(L_{p,i};\mathbf{p}) - R_{\text{exp},i}\right]^2. \tag{9.6}$$

To isolate the fit quality based only on the shape of the attenuation curve (reflectivity versus thickness), both the experimental data (R_{exp}) and the model output (M) were normalized by dividing by their respective maximum values.

To ensure physically valid estimations, the following boundaries on the parameters are imposed (Eq. 9.7):

$$\begin{aligned} 10^2 \leq \alpha_p \leq 5 \cdot 10^5 \\ 1.3 \leq n_2 \leq 1.6 \\ 1.4 \leq n_3' \leq 2.5 \\ 0 \leq k_3 \leq 0.8 \end{aligned} \tag{9.7}$$

Additionally, a nonlinear constraint (Eq. 9.8) is applied on the interface reflectance R_{23} to restrict it to a feasible range:

$$0.7 \leq R_{23} \leq 1 \tag{9.8}$$

This ensures that the model does not produce unphysical values for the interfacial reflectance.

The minimization was performed using MATLAB®'s *fmincon* routine with parameter vector from Eq. 9.6 and initial guess: $p_0 = [10^4,\ 1.48,\ 1.6,\ 0.05]$.

After convergence, the estimated parameters p_{est} yield the modeled reflectance curve $R_{\text{model}}(L_p; p_{\text{est}})$ which must be compared to the experimental values. The goodness of the fit was evaluated through the coefficient of determination ($R^2 = 0.8944$), the root mean squared error ($RMSE = 0.0396$), and the mean absolute error ($MAE = 0.0284$), indicating a good agreement between the model and the experimental data. Fig. 9.8 shows the obtained simulated curve.

The optimization converged to the following set of parameters:

Estimated Parameter	Symbol	Value
Paraloid® B72 Absorption Coeff. [m^{-1}]	α_p	10^4
Paraloid® B72 Refractive Index	n_2	1.600
Pigment Real Index (n_3')	n_3'	2.405
Pigment Extinction Coeff. (k_3)	k_3	0.491
Final Cost Function Value	$fval$	$7.833 \cdot 10^{-3}$

Table 9.1 Estimated parameters p_{est}.

The very small final value of the cost function ($fval$) indicates an excellent fit between the normalized theoretical model and the experimental reflectivity data.

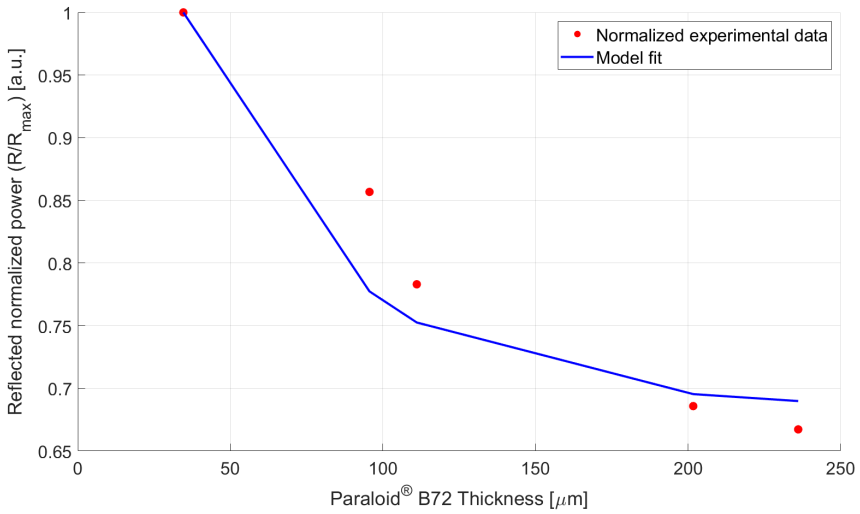

Fig. 9.8 Experimentally acquired reflectance data as a function of thickness with the corresponding simulated fitting curve.g

From these parameters, the reflectivity at the internal interface R_{23} is calculated: $R_{\text{interface}} = R_{23} = 0.055$

9.2.2 Simulation

Once the parameter have been correctly estimated from the experimental values, the total emitted Near-Infrared (NIR) fluorescence ($I_{\text{em\_tot}}$) can be estimated as the Paraloid® B72 thickness (d_1) varies from 0 µm to 250 µm.

When the varnish or the pigment absorbs light at the excitation wavelength λ_{exc}, part of the absorbed energy is re-emitted at a longer wavelength λ_{em} due to the fluorescence process. The local generation rate of fluorescence in each infinitesimal layer d_z is given by Eq. 9.9:

$$dI_{\text{gen}}(z) = \eta_q dI_{\text{gen}}(z) = \eta_q I_0 \alpha_{\text{exc}} e^{-\alpha_{\text{exc}} z}\, dz \tag{9.9}$$

where η_q is the quantum yield (fraction of absorbed photons re-emitted as fluorescence), α_{exc} is the absorption coefficient at the excitation wavelength, and I_0 is the incident excitation intensity. Each infinitesimal element emits radiation in all directions. The forward-propagating component, reaching the outer surface after crossing the remaining thickness $L - z$, is attenuated by self-absorption according to

Eq. 9.10:

$$dI_{\text{em,forward}}(z) = \eta_q I_0 \alpha_{\text{exc}} e^{-\alpha_{\text{exc}} z} e^{-\alpha_{\text{em}}(L-z)}\, dz \tag{9.10}$$

where α_{em} is the absorption coefficient at the emission wavelength. Integrating over the entire varnish thickness yields the total emitted fluorescence intensity is given by Eq. 9.11:

$$I_{\text{em,tot}}(L) = \eta_q I_0 \alpha_{\text{exc}} \int_0^L e^{-\alpha_{\text{exc}} z} e^{-\alpha_{\text{em}}(L-z)}\, dz \tag{9.11}$$

After solving the integral, the analytical solution can be written as Eq. 9.12:

$$I_{\text{em,tot}}(L) = \eta_q I_0 \alpha_{\text{exc}} \frac{e^{-\alpha_{\text{em}} L} - e^{-\alpha_{\text{exc}} L}}{\alpha_{\text{exc}} - \alpha_{\text{em}}} \tag{9.12}$$

This equation predicts that the fluorescence intensity first increases with thickness (as more material absorbs the excitation light) and then decreases exponentially for large L, due to self-absorption of both excitation and emission. Therefore, a maximum fluorescence intensity is expected for an intermediate varnish thickness, a behavior observed experimentally and reproduced numerically.

The simulation uses the parameters derived above and applies the Beer-Lambert law in a layer-by-layer structure. The key assumption here is that the Egyptian Blue substrate is semi-infinite and totally absorbing for the transmitted light. The absorption coefficient of the Egyptian Blue at the excitation wavelength ($\lambda_{ecc} = 600\,\text{nm}$) is estimated directly from the optimized extinction coefficient k_3 in Eq. 9.13:

$$\alpha_{\text{ecc},2} = \frac{4\pi k_3}{\lambda_{\text{ecc}}} \approx 439,820\ [\text{m}^{-1}] \tag{9.13}$$

This extremely high value confirms the pigment's strong absorption. The Total Emitted Fluorescence ($I_{\text{em\_tot}}$) is the sum of two main contributions, both attenuated as they exit the system:

$$I_{\text{em\_tot}}(d_1) = I_{\text{em\_BWD}} + I_{\text{em\_sub}} \tag{9.14}$$

Where $I_{\text{em\_BWD}}$ is the weak fluorescence generated within the varnish layer itself, propagating backwards (BWD) and $I_{\text{em\_sub}}$ is the strong fluorescence generated by the Egyptian Blue, which must pass back through the Paraloid® B72, experiencing auto-reabsorption ($e^{-\alpha_{\text{em},1} d_1}$). The dominant term ($I_{\text{em\_sub}}$) is therefore determined by the combined exponential attenuation of the excitation light reaching the pigment

layer and of the emitted light passing through the varnish:

$$I_{\text{em\_sub}} \propto e^{-(\alpha_{\text{ecc},1}+\alpha_{\text{em},1})d_1} \tag{9.15}$$

The simulation results are presented in two plots, reported in Fig. 9.9 and Fig. 9.10.

- Total Emitted Fluorescence (I_{em}) vs. Varnish Thickness Behavior – Fig. 9.9: The fluorescence intensity exhibits a sharp exponential decay as the Paraloid® B72 thickness (d_1) increases. This decay demonstrates that the Paraloid® B72 works as an optical filter or absorber. Even if the pigment presents a strong intrinsic fluorescence (quantum efficiency $\eta_{q,2} = 0.15$), the signal drops because the varnish absorbs both the incoming excitation light (λ_{ecc}) and the back-propagating NIR fluorescence light (λ_{em}) before it reaches the air again. This plot has great relevance for non-invasive analysis, as it quantifies how much a given varnish thickness reduces the fluorescence, allowing for a preliminary calibration of the pigment thickness.

- Transmitted Light vs. Varnish Thickness – Fig. 9.10: the transmitted intensity ($I_{\text{ecc\_tx}}$) is zero across all simulated thicknesses. This plot is just to verify that the results are consistent with the model assumption that the Egyptian Blue acts as a semi-infinite, opaque substrate ($\alpha_{\text{ecc},2} \approx 440000\ \text{m}^{-1}$). All the light that is not absorbed by the Paraloid® B72 is immediately absorbed by the pigment. The measurement is confirmed to be purely in reflection.

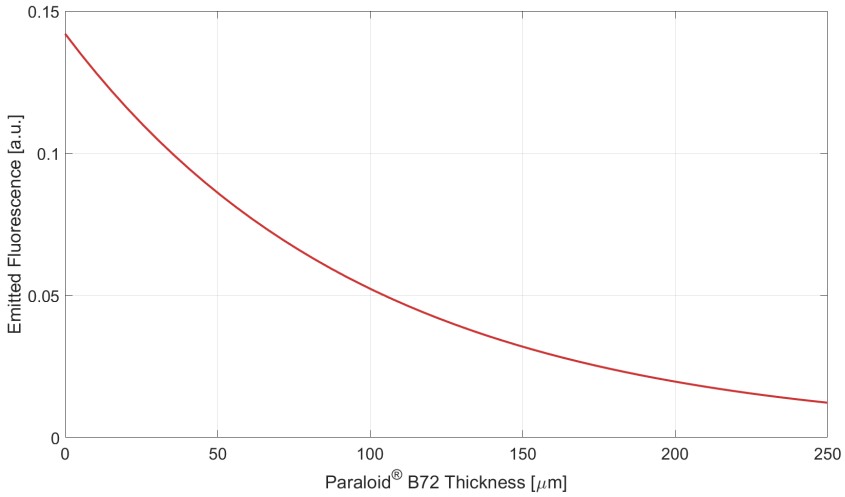

Fig. 9.9 Total Emitted Fluorescence (I_{em}) vs. Varnish Thickness Behavior

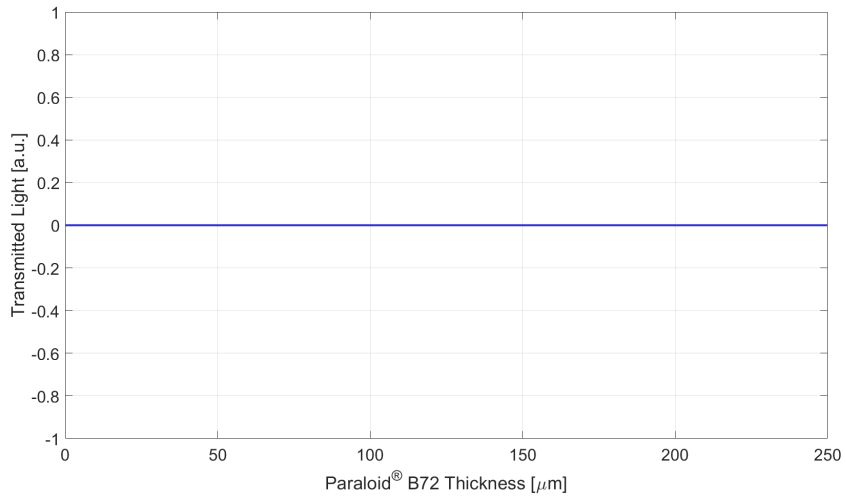

Fig. 9.10 Transmitted Light vs. Varnish Thickness

Chapter 10

Real case study

Since the measurements on prepared samples yielded satisfactory results, the OCT was tested on an ancient Egyptian wooden coffin, applying the calibration described in previous sections. Fig. 10.1 reports a picture of the analyzed area, where the artifact white line indicates the location of the OCT measurement. At that position, the artifact has a dark painted line partially covered by ancient mastic, whereas the area is coated by a Paraloid® B72 layer that was deposited during a previous intervention.

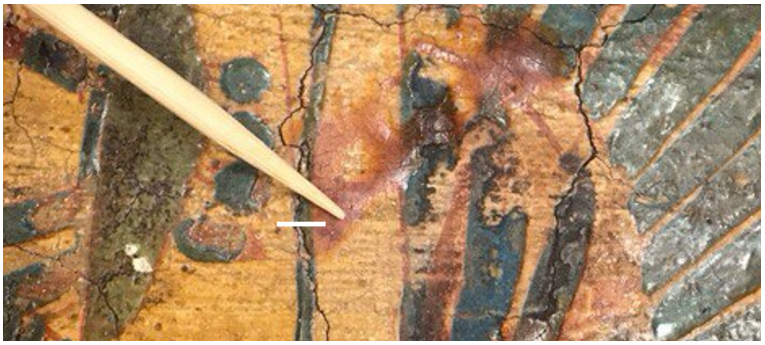

Fig. 10.1 Egyptian artifact. The white line indicates the cross section of OCT measurements.

Fig. 10.2 shows the correspondent OCT image. The layer thickness was evaluated by applying the procedure described in Sec. 8.1.2. In all the points measured, a value of 15.4 µm was obtained, with deviations between 0.9 µm and 4.8 µm, thus suggesting a discrete overestimation of OCT measurements. Concerning the point of analysis of Fig. 10.1, of a value of 31.7 µm, a higher variability of the Paraloid® B72

layer might be hypothesized and ascribed to the hand-made deposition of the varnish during the previous intervention.

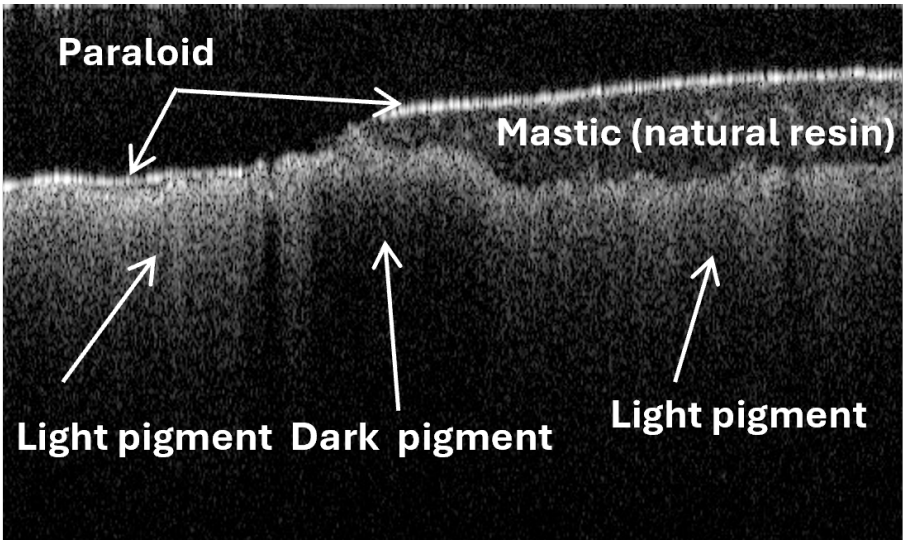

Fig. 10.2 OCT image correspondent to the white line of Fig. 10.1. The Paraloid® B72 layer thickness is estimated to be 31.7 µm.

As already said, the manual analysis of the images is long and difficult to be performed. The trained segmentation model (see Sec. 8.2 for further details) was applied to OCT images acquired on the surface of the Egyptian sarcophagus to identify and map the different stratigraphic layers. Fig. 10.3 shows the application of the algorithm on the image acquired in the point of analysis of Fig. 10.1. The automated segmentation successfully delineated the varnish, pigment, and preparation layers, providing a clear visualization of their thickness variations across the scanned region. This application demonstrates the potential of the model to assist in the rapid, objective interpretation of complex OCT datasets, offering valuable support for material characterization and conservation diagnostics directly on cultural heritage objects.

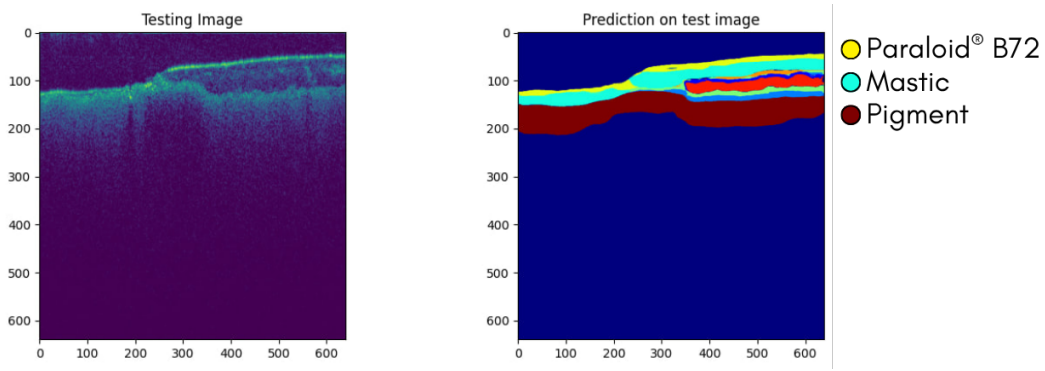

Fig. 10.3 OCT image and the correspondent image segmentation correspondent to the white line of Fig. 10.1. Left: original image. Right: segmented image.

The system's ability to acquire 512 images within a 1×7 mm^2 analysis area underscores its potential for comprehensive, nondestructive mapping of layer thickness variability, offering a promising approach for detailed assessment of material distribution across the surface.

A volumetric OCT acquisition was performed on a selected area of the Egyptian sarcophagus (Fig. 10.4) to investigate the internal structure of the pictorial layers without the need for any sampling or invasive procedures.

Fig. 10.4 Egyptian artifact. The wooden stick indicates the area of OCT volume measurement.

The reconstructed volume provides a three-dimensional representation (Fig. 10.5) of the stratigraphy, where distinct layers and interfaces can be clearly distinguished based on their optical reflectivity and scattering contrast.

Overall, the OCT results demonstrate the capability of the technique to deliver high-resolution volumetric information on complex, multilayered surfaces typical of ancient painted artifacts. This approach not only enables the visualization of

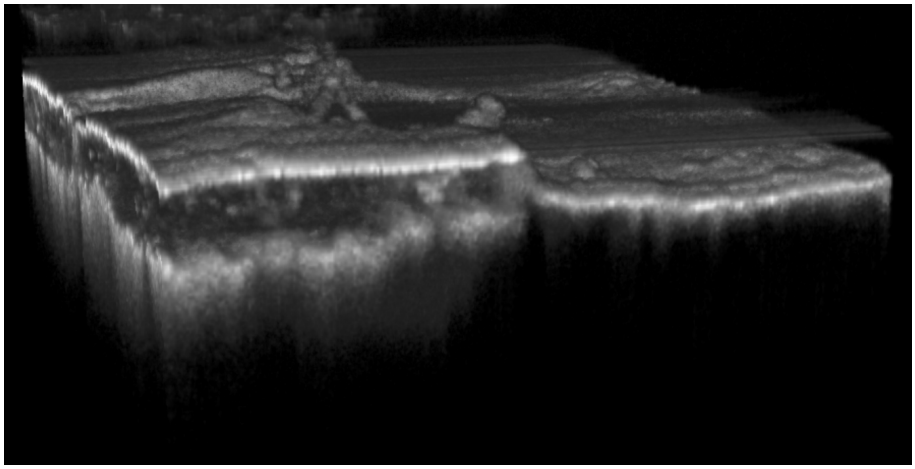

Fig. 10.5 OCT reconstructed volume image correspondent to the area in Fig. 10.4.

subsurface features and layer boundaries but also offers valuable insight into the distribution, thickness, and preservation state of the materials.

To conclude the analysis of the artifact, a fluorescence analysis was also carried out. Figure 10.6 shows the normalized spectra acquired from the region highlighted in Figure 10.1. The acquisitions were performed on both sides of the area, namely with and without the mastic layer. The region containing the mastic (whose thickness was estimated to be approximately 200 µm) exhibits an emitted fluorescence at 900 nm of 0.019. When this value is compared with the simulated fluorescence shown in Figure 9.9, it corresponds to a thickness of 198 µm, which is perfectly consistent with the values estimated through the OCT measurements.

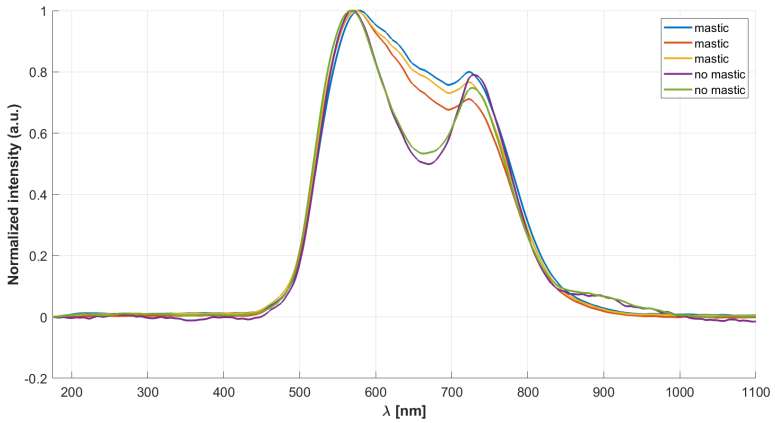

Fig. 10.6 Normalized spectra acquired from the region highlighted in Figure 10.1.

Chapter 11

Conclusions

Optical fiber sensors, owing to their well-known advantages, have been applied in various critical monitoring domains. Despite this, their widespread use is still hindered by the cost, size, and complexity of the interrogation units.

Currently, monitoring strategies largely rely on discrete sampling, transportation of samples to specialized laboratories, use of complex analytical instruments, and expertise of trained personnel. However, future developments are expected to enable a transition towards ubiquitous, real-time, non-invasive assessment through compact and low-cost devices. Such an approach would allow continuous, in-situ monitoring across diverse contexts, ranging from environmental systems, water quality monitoring, agri-food sustainability and safety, to cultural and natural heritage protection.

This research aimed to explore and experimentally validate the combination of a set of optical sensing technologies for real-time, continuous, and minimally invasive monitoring in two distinct yet complementary fields: environmental systems and cultural heritage conservation. The main idea was to exploit the intrinsic advantages of light–based sensing like high sensitivity, immunity to electromagnetic interference, compactness, and the possibility of distributed measurements, to develop simple, robust, and cost-effective devices capable of providing reliable information without the need for invasive assessment and sampling, complex laboratory analyses or highly specialized operators.

This study is strongly aligned with several United Nations Sustainable Development Goals (SDGs), which demand for affordable and sustainable monitoring

strategies, essential to ensure the responsible use of resources and the protection of both natural and cultural assets. By focusing on applications with strong societal impact, specifically water quality and cultural heritage conservation, the research here presented aligns with clean water and sanitation (SDG 6), zero hunger and sustainable agriculture (SDG 2), good health and well-being (SDG 3), and sustainable cities and communities (SDG 11).

For instance, SDG 6 aims to ensure access to clean and safe water for all; however, billions of people worldwide still live without safe drinking water. Similarly, SDG 2 promotes sustainable agriculture, while food safety is recognized as a fundamental requirement for healthy lives (SDG 3). Furthermore, cultural heritage represents one of the most significant assets in countries such as Italy, where its preservation is essential not only for safeguarding it for future generations (SDG 11) but also for its considerable economic impact.

In more detail, the research activity presented in this thesis has been focused on the development of two main case studies.

The first case study focused on water monitoring, where Surface Plasmon Resonance (SPR) and Fluorescence Spectroscopy (FS) were investigated as complementary optical methods for assessing the quality of liquid samples. In particular, SPR-based refractometers enable the measurement of refractive index variations as indicators of contamination, while fluorescence combined with microfluidics allows accurate and continuous pH monitoring. The design of the SPR sensors was first optimized through numerical simulations, allowing the evaluation of different geometries and configurations to identify those most suitable for production and successive experimental implementation. Following the design phase an automated procedure, based on fit tree algorithms, for the calibration has been developed. The results confirmed the feasibility of achieving reliable measurements while maintaining low cost and mechanical robustness, making the approach particularly promising for deployment in developing regions where water quality issues are most severe. For fluorescence-based sensing, as a first step pH monitoring was implemented through the use of fluorescent dyes integrated within microfluidic platforms. This configuration enabled accurate, continuous, and stable measurements over extended periods, demonstrating the potential of this approach for real-time water quality tracking. Together, the SPR and fluorescence results highlight how optical tech-

nologies can enable a quasi-complete understanding of the chemical and physical processes occurring in water systems.

The second application area focused on cultural heritage monitoring, where the preservation of artworks and artifacts requires non-destructive analytical methods capable of distinguishing between material layers and identifying them. The integration of Fluorescence Imaging, Optical Coherence Tomography (OCT), and Artificial Intelligence (AI)-based image segmentation proved to be an effective and innovative solution for the cultural heritage monitoring during conservation

Fluorescence enabled the identification and measurements of varnish layers, while OCT provided depth-resolved information about their thickness and structure, in particular the rugosity. The AI-powered segmentation algorithms allowed automated layer recognition and improved the repeatability of the analysis, reducing the time required for each spot and the need of and expert operator.

The developed methodology demonstrated that a combined optical approach can yield accurate, non-invasive characterization of multilayer systems, making it easy to use on a regular basis in conservation laboratories and museums. Compared to conventional methods such as Scanning Electron Microscopy (SEM), which require sample removal and specialized operation, the proposed optical system offers a safer, faster, and more cost-effective alternative. It is important to highlight that this approach can be used on artworks without damaging them, allowing a real time and continuous monitoring during conservation intervention.

The outcomes of this research confirm the effectiveness and versatility of optical fiber and light-based sensing techniques in a wide range of monitoring scenarios. The design process and the experiments carried out demonstrated that such technologies are capable of providing quantitative and reliable data, often in conditions where traditional sensors or analytical methods are impractical or too invasive. The integration of AI and advanced signal processing further enhanced the interpretability of the data and contributed to a more automated and reliable analysis results.

From a broader perspective, the results highlight the possibility of implementing low-cost, compact, and user-friendly optical systems, opening new opportunities for large-scale implementation in different contexts. In environmental monitoring, such systems could be integrated into smart infrastructures or autonomous sensor networks, while in cultural heritage, they can be a useful tool to help conservators

during restoration interventions to monitor in real time the effectiveness and safety of a cleaning procedure.

In conclusion, this Ph.D. path demonstrates that optical sensing technologies, by combining physics, materials science, and artificial intelligence, can provide powerful tools for sustainable and intelligent monitoring. The approaches developed within this research are not only technical but also aligned with global needs for sustainability, accessibility, and resource efficiency. The findings lay the foundation for future implementations of compact optical sensors capable of delivering high-quality, real-time information across different fields, contributing to a safer, cleaner, and more resilient society.

References

[1] https://sdgs.un.org/goals.

[2] Faramarz Farahi. *Handbook of Optical Sensors*. 2014.

[3] Pravati Panda and Subhendu Chakroborty. Optical sensor technology and its application in detecting environmental effluents: a review. *International Journal of Environmental Analytical Chemistry*, 104(16):4057–4072, 2024.

[4] K.Fidanboylu and Hasan Efendioğlu. Fiber optic sensors and their applications. 05 2009.

[5] Cristiano Pendão and Ivo Silva. Optical fiber sensors and sensing networks: Overview of the main principles and applications. *Sensors*, 22(19), 2022.

[6] Thomas Wriedt. *Mie Theory: A Review*, pages 53–71. Springer Berlin Heidelberg, Berlin, Heidelberg, 2012.

[7] Andrew T. Young. Rayleigh scattering. *Appl. Opt.*, 20(4):533–535, Feb 1981.

[8] Leizi Jiao, Nianbing Zhong, Xiande Zhao, Shixiang Ma, Xinglan Fu, and Daming Dong. Recent advances in fiber-optic evanescent wave sensors for monitoring organic and inorganic pollutants in water. *TrAC Trends in Analytical Chemistry*, 127:115892, 2020.

[9] Pierre Giacomo. The michelson interferometer. *Mikrochim Acta*, 93:19–31, 1987.

[10] Hamed Saghaei, Payam Elyasi, and Rouhollah Karimzadeh. Design, fabrication, and characterization of mach–zehnder interferometers. *Photonics and Nanostructures - Fundamentals and Applications*, 37:100733, 2019.

[11] Jasjot K. Sahota, Neena Gupta, and Divya Dhawan. Fiber Bragg grating sensors for monitoring of physical parameters: a comprehensive review. *Optical Engineering*, 59(6):060901, 2020.

[12] Vasimalla Yesudasu, Himansu Shekhar Pradhan, and Rahul Jasvanthbhai Pandya. Recent progress in surface plasmon resonance based sensors: A comprehensive review. *Heliyon*, 7(3):e06321, 2021.

[13] J M Pitarke, V M Silkin, E V Chulkov, and P M Echenique. Theory of surface plasmons and surface-plasmon polaritons. *Reports on Progress in Physics*, 70(1):1, 2007.

[14] Jean-Jacques Greffet. Introduction to surface plasmon theory. In S. Enoch and N. Bonod, editors, *Plasmonics*, volume 167 of *Springer Series in Optical Sciences*, page Chapter 4. Springer-Verlag Berlin Heidelberg, 2012.

[15] Zeev Zalevsky and Ibrahim Abdulhalim. Chapter 6 - plasmonics. In Zeev Zalevsky and Ibrahim Abdulhalim, editors, *Integrated Nanophotonic Devices*, Micro and Nano Technologies, pages 175–240. William Andrew Publishing, Oxford, 2010.

[16] Richard B. M. Schasfoort. Introduction to Surface Plasmon Resonance. In *Handbook of Surface Plasmon Resonance*. The Royal Society of Chemistry, May 2017.

[17] Lukas Novotny and Bert Hecht. *Principles of nano-optics*. Cambridge University Press, 2012.

[18] Anatoly V Zayats, Igor I Smolyaninov, and Alexei A Maradudin. Nano-optics of surface plasmon polaritons. *Physics Reports*, 408(3-4):131–314, 2005.

[19] Erwin Kretschmann and Heinz Raether. Notizen: radiative decay of non radiative surface plasmons excited by light. *Zeitschrift für Naturforschung A*, 23(12):2135–2136, 1968.

[20] Andreas Otto. Excitation of nonradiative surface plasma waves in silver by the method of frustrated total reflection. *Zeitschrift für Physik*, 216(4):398–410, 1968.

[21] M. Oliverio, S. Perotto, G.C. Messina, L. Lovato, and F. De Angelis. Chemical functionalization of plasmonic surface biosensors: a tutorial review on issues, strategies, and costs. *ACS Applied Materials & Interfaces*, 9:29394–29411, 2017.

[22] F. Wu, P. Thomas, V. Kravets, H. Arola, M. Soikkeli, and et al. Layered material platform for surface plasmon resonance biosensing. *Scientific Reports*, 9:1–10, 2019.

[23] N. Cennamo, G. D'Agostino, F. Sequeira, F. Mattiello, G. Porto, A. Biasiolo, R. Nogueira, L. Bilro, and L. Zeni. A simple and low-cost optical fiber intensity-based configuration for perfluorinated compounds in water solution. *Sensors*, 18:3009, 2018.

[24] X. Zhao, Y. Chu-Su, W.-H. Tsai, C.-H. Wang, T.-L. Chuang, C.-W. Lin, Y.-C. Tsao, and M.-S. Wu. Improvement of the sensitivity of the surface plasmon resonance sensors based on multi-layer modulation techniques. *Optics Communications*, 335:32–36, 2015.

[25] Banshi Dhar Gupta, Sachin Kumar Srivastava, and Roli Verma. *Fiber optic sensors based on plasmonics*. World Scientific, 2015.

[26] Anuj K Sharma and BD Gupta. On the sensitivity and signal to noise ratio of a step-index fiber optic surface plasmon resonance sensor with bimetallic layers. *Optics Communications*, 245(1-6):159–169, 2005.

[27] Rana Tabassum and Banshi D Gupta. Spr based fiber-optic sensor with enhanced electric field intensity and figure of merit using different single and bimetallic configurations. *Optics Communications*, 367:23–34, 2016.

[28] V. Brucker. *To the Use of Sellmeier Formula*, pages 1–7. Springer, 2017.

[29] Hitoshi Suzuki, Mitsunori Sugimoto, Yoshikazu Matsui, and Jun Kondoh. Effects of gold film thickness on spectrum profile and sensitivity of a multimode-optical-fiber spr sensor. *Sensors and Actuators B: Chemical*, 132(1):26–33, 2008.

[30] Yogendra S Dwivedi, Anuj K Sharma, and Banshi D Gupta. Influence of skew rays on the sensitivity and signal-to-noise ratio of a fiber-optic surface-plasmon-resonance sensor: a theoretical study. *Applied optics*, 46(21):4563–4569, 2007.

[31] Dalibor Ciprian and Petr Hlubina. Theoretical model of the influence of oxide overlayer thickness on the performance of a surface plasmon fibre-optic sensor. *Measurement Science and Technology*, 24(2), 2013.

[32] B D Gupta and C D Singh. Evanescent-absorption coefficient for diffuse source illumination: uniform-and tapered-fiber sensors. *Applied optics*, 33(13):2737–2742, 1994.

[33] Yu Xu, H. S. Lee, P. C. Chen, Y. T. Wu, H. F. Chung, and C. P. Lee. Analytical estimates of the characteristics of surface plasmon resonance fibre-optic sensors. *Journal of Modern Optics*, 47(6):1099–1110, 2000.

[34] M. Kanso, Stéphane Cuenot, and G. Louarn. Sensitivity of optical fiber sensor based on surface plasmon resonance: modeling and experiments. *Plasmonics*, 3(2-3):49–57, 2008.

[35] Support Vector Regressor Theory. https://medium.com/@niousha.rf/support-vector-regressor-theory-and-coding-exercise-in-python-ca6a7dfda927. Accessed: 2025-10-29.

[36] Support Vector Machine (SVM), MathWorks. https://it.mathworks.com/discovery/support-vector-machine.html. Accessed: 2025-10-29.

[37] Statistics and Machine Learning Toolbox, MathWorks. https://it.mathworks.com/products/statistics.html. Accessed: 2025-10-29.

[38] Adam Slowik and Halina Kwasnicka. Evolutionary algorithms and their applications to engineering problems. *Neural Computing and Applications*, 32:12363–12379, 2020.

[39] Genetic Algorithm, MathWorks. https://it.mathworks.com/discovery/genetic-algorithm.html. Accessed: 2025-10-29.

[40] Optimization Toolbox, MathWorks. https://it.mathworks.com/products/optimization.html. Accessed: 2025-10-29.

[41] Decision Tree Regressor. https://medium.com/data-science/decision-tree-regressor-explained-a-visual-guide-with-code-examples-fbd2836c3bef. Accessed: 2025-10-29.

[42] Joseph Lakowicz. *Principles of Fluorescence Spectroscopy*, volume 1. 01 2006.

[43] Jablonski Diagram. https://www.edinst.com/blog/jablonski-diagram-2/. Accessed: 2025-10-29.

[44] F. Le Guern, V. Mussard, A. Gaucher, M. Rottman, and D. Prim. Fluorescein derivatives as fluorescent probes for ph monitoring along recent biological applications. *Int J Mol Sci*, 21(23), 2020.

[45] Mounted LED. https://www.thorlabs.com/thorproduct.cfm?partnumber=M450LP2. Accessed: 2025-10-29.

[46] AvaSpec-3648 Fiber Optic Spectrometer. https://www.avantes.ru/en/spectrometer/avaspec3648.php. Accessed: 2025-10-29.

[47] USB Data Acquisition – NI USB-6003. https://www.ni.com/docs/en-US/bundle/usb-6003-specs/resource/374372a.pdf. Accessed: 2025-10-29.

[48] Adafruit AS7341 8-Channel Light. https://www.adafruit.com/product/4698. Accessed: 2025-10-29.

[49] k-Nearest Neighbors (kNN). https://scikit-learn.org/stable/modules/neighbors.html. Accessed: 2025-10-29.

[50] fitcknn, MathWorks. https://it.mathworks.com/help/stats/fitcknn.html. Accessed: 2025-10-29.

[51] Jorien R. Duivenvoorden. How to approach long-term monitoring of chemical dynamics in oil paintings? *npj Heritage Science*, 13:24, 2 2025.

[52] Raffaella Fontana, Marco Bellini, Chiara Corsi, Maria Mastroianni, Marzia Materazzi, Luca Pezzati, and Alessandra Tortora. Optical coherence diagnostics for painting conservation. 6618:661808, 2007.

[53] Leila Es Sebar, Luca Lombardo, Paola Buscaglia, Tiziana Cavaleri, Alessandro Lo Giudice, Alessandro Re, Matilde Borla, Sara Aicardi, and Sabrina Grassini. 3D multispectral imaging for cultural heritage preservation: The case study of a wooden sculpture of the Museo Egizio di Torino. *Heritage*, 6, 2023.

[54] Louise Husby, Cecil Andersen, Nanna Bjerregaard Pedersen, and Bronwyn Ormsby. Evaluating three water-based systems and one organic solvent for the removal of dammar varnish from artificially aged oil paint samples. *Heritage Science*, 11, 11 2023.

[55] Chiara Biribicchi, Laura Giuliani, Andrea Macchia, and Gabriele Favero. Organogels for low-polar organic solvents: Potential applications on cultural heritage materials. *Sustainability*, 15(23), 2023.

[56] Nicole Manfredda, Paola Buscaglia, Paolo Gallo, Matilde Borla, Sara Aicardi, Giovanna Poggi, Piero Baglioni, Marco Nervo, Dominique Scalarone, Alessandro Borghi, Alessandro Re, Laura Guidorzi, and Alessandro Lo Giudice. An ancient egyptian multilayered polychrome wooden sculpture belonging to the museo egizio of torino: Characterization of painting materials and design of cleaning processes by means of highly retentive hydrogels. *Coatings*, 11(11), 2021.

[57] Emilio Catelli, Zelan Li, Giorgia Sciutto, Paolo Oliveri, Silvia Prati, Michele Occhipinti, Alessandro Tocchio, Roberto Alberti, Teo Frizzi, Cristina Malegori, and Mazzeo Rocco. Towards the non-destructive analysis of multilayered samples: A novel XRF-VNIR-SWIR hyperspectral imaging system combined with multiblock data processing. *Analytica Chimica Acta*, 2022.

[58] Alessia Volino, Maria Rosaria Barone Lumaga, Paola Cennamo, Giancarlo Fatigati, and Giorgio Trojsi. Multidisciplinary approach for the study of the Ptolemaic coffin of Ankhhapy from the egyptian collection of MANN in Naples. In *2018 Metrology for Archaeology and Cultural Heritage (MetroArchaeo)*, pages 6–11, 2018.

[59] Piotr Targowski, Magdalena Iwanicka, Ludmiła Tymińska-Widmer, Marcin Sylwestrzak, and Ewa A. Kwiatkowska. Structural examination of easel paintings with optical coherence tomography. *Accounts of Chemical Research*, 43(6):826–836, jun 2010.

[60] Jana Striova, Barbara Salvadori, Raffaella Fontana, Antonio Sansonetti, Marco Barucci, Enrico Pampaloni, Eleonora Marconi, Luca Pezzati, and Maria Perla Colombini. Optical and spectroscopic tools for evaluating Er:YAG laser removal of shellac varnish. *Studies in Conservation*, 2015.

[61] Paulina Strąkowska, Marcin Strąkowski, Jerzy Pluciński, and Bogdan Kosmowski. Non-destructive inspection of anti-corrosion protective coatings using optical coherent tomography. *Metrology and Measurement Systems*, 19, 01 2012.

[62] Magdalena Iwanicka, Ewa A. Kwiatkowska, Marcin Sylwestrzak, and Piotr Targowski. Application of optical coherence tomography (OCT) for real time monitoring of consolidation of the paint layer in Hinterglasmalerei objects. 8084:80840G, 2011.

[63] Magdalena Iwanicka, Patrizia Moretti, Saskia van Oudheusden, Marcin Sylwestrzak, Laura Cartechini, Klaas Jan van den Berg, Piotr Targowski, and Costanza Miliani. Complementary use of Optical Coherence Tomography (OCT) and Reflection FTIR spectroscopy for in-situ non-invasive monitoring of varnish removal from easel paintings. *Microchemical Journal*, 2018.

[64] AA.VV. Lumedica Labscope. https://www.lumedicasystems.com/oq-labscope/. Accessed: 2023-12-07.

[65] Margaret Read, C. S. Cheung, Haida Liang, Andrew Meek, and Capucine Korenberg. A Non-invasive Investigation of Egyptian Faience Using Long Wavelength Optical Coherence Tomography (OCT) at 2 m. *Studies in Conservation*, 67:168–175, 2022.

[66] Manob Jyoti Saikia. A spectroscopic diffuse optical tomography system for the continuous 3-d functional imaging of tissue—a phantom study. *IEEE Transactions on Instrumentation and Measurement*, 70:1–8, 2021.

[67] Maryam Monemian and Hossein Rabbani. Analysis of a novel segmentation algorithm for optical coherence tomography images based on pixels intensity correlations. *IEEE Transactions on Instrumentation and Measurement*, 70:1–12, 2021.

[68] Stephen P. Koob. The use of Paraloid B-72 as an adhesive: its application for archaeological ceramics and other materials. *Studies in Conservation*, 31(1):7–14, 1986.

[69] Velson Horie. Materials for conservation: Organic consolidants, adhesives and coatings, second edition. *Materials for Conservation: Organic consolidants, adhesives and coatings, Second Edition*, pages 1–489, 01 2013.

[70] M.S. Tite, M. Bimson, and M.R. Cowell. *Technological Examination of Egyptian Blue*, chapter 11, pages 215–242. ACS Publications, 1984.

[71] Paraloid B72 Refractive Index. https://cameo.mfa.org/wiki/Paraloid_B-72. Accessed: 2024-07-31.

[72] Paraloid B72 Refractive Index. https://cool.culturalheritage.org/jaic/articles/jaic42-02-011.html. Accessed: 2024-07-31.

[73] Takaaki Harada, Stephanie Spence, Athanasios Margiolakis, Skylar Deckoff-Jones, Rebecca Ploeger, Aaron N. Shugar, James F. Hamm, Keshav M. Dani, and Anya R. Dani. Obtaining cross-sections of paint layers in cultural artifacts using femtosecond pulsed lasers. *Materials*, 10(2), 2017.

[74] Pedro M.D. Santos and Eduardo N.B.S. Júlio. A state-of-the-art review on roughness quantification methods for concrete surfaces. *Construction and Building Materials*, 38:912–923, 2013.

[75] https://www.thorlabs.com/thorproduct.cfm?partnumber=MBB1F1.

[76] https://www.thorlabs.com/thorproduct.cfm?partnumber=LEDD1B.

[77] https://www.ni.com/it-it/shop/model/usb-tc01.html?srsltid=AfmBOor$_H$*Ksdt*09*lE*03*AYg* − 369*aY*8*GF*$_P$7*L*6*lwhZp*8*tqLgq*7*Lzw*6*gFF*.

[78] https://docs.rs online.com/51f6/0900766b815bb510.pdf.

Appendix A

Sensor Fabrication and Acquisition

Fiber preparation and stripping

For the fabrication of the fiber-optic sensors, standard single-mode optical fiber segments with a total length of approximately 40 cm were employed. A central section (l_{sens}) was designated as the sensing region (Fig. A.1). In this portion, the polymer coating and the silica cladding were removed in order to expose the silica core of the fiber.

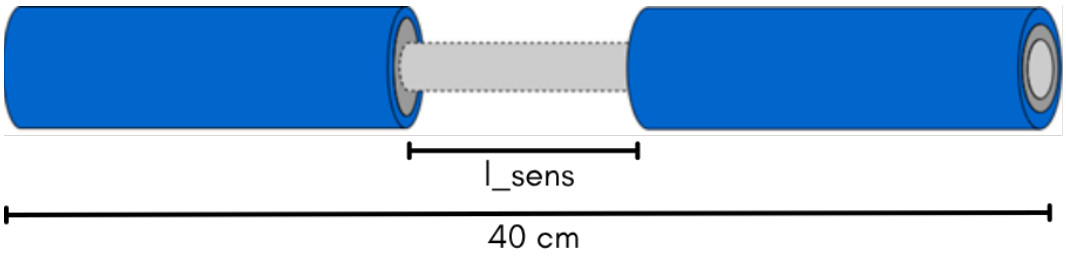

Fig. A.1 Schematic of the fiber with the polymer coating and the silica cladding removed to expose the silica core of the fiber.

The stripping process was carried out using a precision fiber-stripping machine, specifically adjusted to ensure complete and uniform removal of the protective layers without inducing structural damage to the fiber core. The exposed segment of the fiber core obtained through this process constituted the region for subsequent thin-film deposition.

Metallic Film Deposition by Sputtering

The metallic thin films required for plasmonic sensing were deposited onto the exposed fiber cores by means of DC magnetron sputtering, a Physical Vapor Deposition (PVD) technique that uses a DC power source to generate a plasma, that allows highly controlled and reproducible coating of dielectric substrates with metallic layers. The deposition was carried out in two sequential steps:

1. Titanium adhesion layer – A film of approximately 20 nm thickness was first deposited.
2. Gold plasmonic layer – A gold layer of approximately 50 nm thickness was then deposited on top of the titanium(Fig. A.2).

Prior to deposition, the sputtering chamber was evacuated to high vacuum levels (on the order of 10×10^{-6} mbar), and an argon atmosphere was introduced to serve as the working gas. The deposition rate was carefully calibrated by adjusting the discharge power and argon pressure, allowing control over the final thickness of the deposited films (Fig. A.3).

The stripped fiber segments were mounted on a custom-designed holder (Fig. A.4 left) that ensured proper alignment and uniform coating of half the cylindrical fiber core. The holder was positioned at a defined distance from the sputtering target to minimize shadowing effects and guarantee homogeneous deposition around the curved surface of the fiber. At the end of the deposition procedure the fiber were rotated by 180° to cover the other half of the surface. By combining the titanium adhesion layer with the gold overlayer, a robust and continuous bilayer structure was obtained, suitable for supporting surface plasmon resonance (SPR) phenomena (Fig. A.4 right).

Film Characterization by Profilometry and SEM

Following deposition, the thickness and morphology of the films were characterized. Initial thickness measurements were performed using a surface profilometer, which evaluates the vertical step between coated and uncoated regions of a reference substrate. For this purpose, a flat silicon slide had been placed in the sputtering chamber alongside the fibers during deposition. After deposition, the film thickness

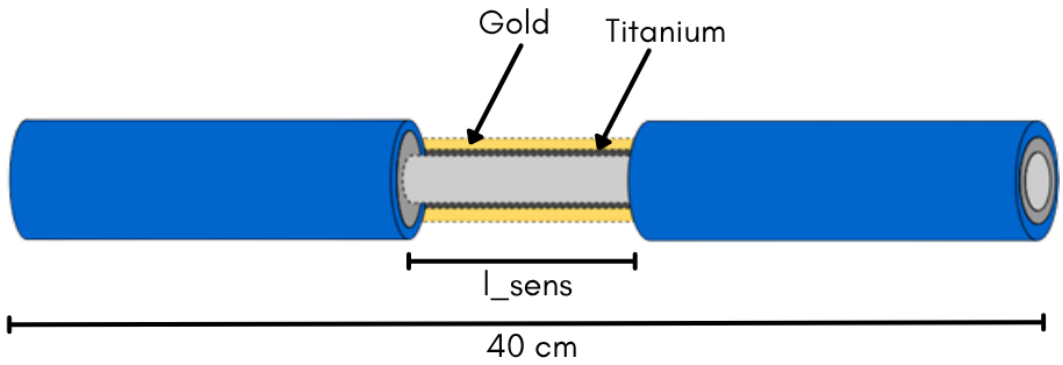

Fig. A.2 Schematic of the fiber with the deposited layers of gold and titanium on the silica core.

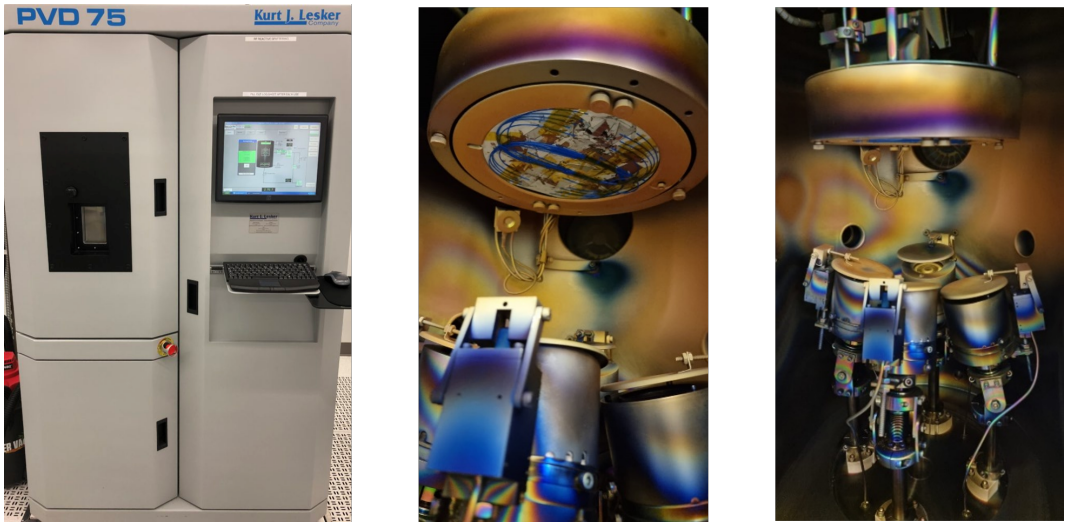

Fig. A.3 Sputtering machine

on the silicon sample was measured, yielding an average value of approximately 60 nm. While profilometry provides a reliable first estimation of film thickness, its resolution is limited, particularly when applied to ultrathin layers below 100 nm. For this reason, additional high-resolution imaging was carried out. Scanning electron microscopy was employed to directly observe the deposited films and to confirm their structural and dimensional properties with nanometric resolution. SEM analysis was conducted both on the silicon reference sample and on the coated fiber segments.

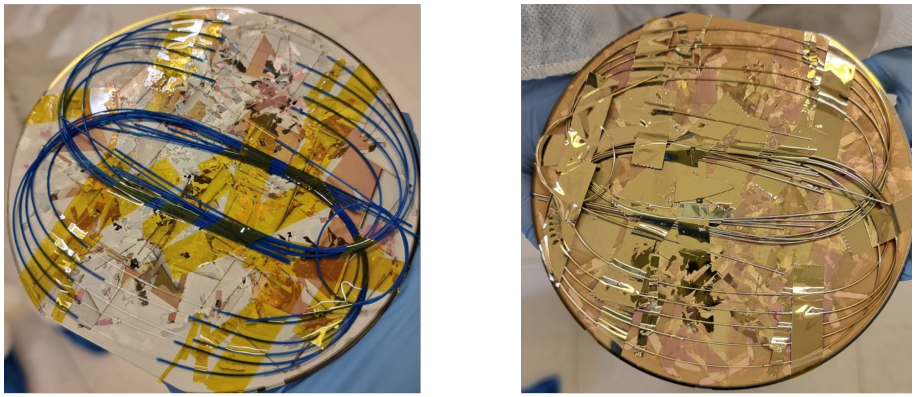

Fig. A.4 Stripped fiber segments mounted on a custom-designed holder before and after the deposition process.

- Silicon reference sample (Fig. A.6): SEM images were acquired at the edge of the deposited film, allowing direct visualization of the transition between coated and uncoated regions. By measuring this step, the thickness of the bilayer film was determined with high precision. The SEM-derived value was consistent with profilometer measurements, confirming a total thickness of approximately 60 nm.
- Optical fiber sample (Fig. A.5): SEM imaging of the fiber cross-section enabled direct observation of the coating on the curved fiber surface. Distinct layers corresponding to the silica core, the titanium adhesion layer, and the gold overlayer were resolved. The gold layer appeared as a continuous and uniform film, while the titanium interlayer was clearly distinguishable at the interface, confirming successful adhesion and proper bilayer formation.

In addition to thickness verification, SEM analysis provided valuable information regarding the homogeneity and continuity of the films. The gold layer was observed to be free from cracks and discontinuities, features that are critical to ensure stable and reproducible plasmonic responses. Although the final thickness was marginally lower than the nominal target ($\approx$ 70 nm), the measured value remained within acceptable tolerances for SPR-based sensing. The deposition process was therefore considered successful.

Fig. A.5 SEM image of the optical fiber sample.

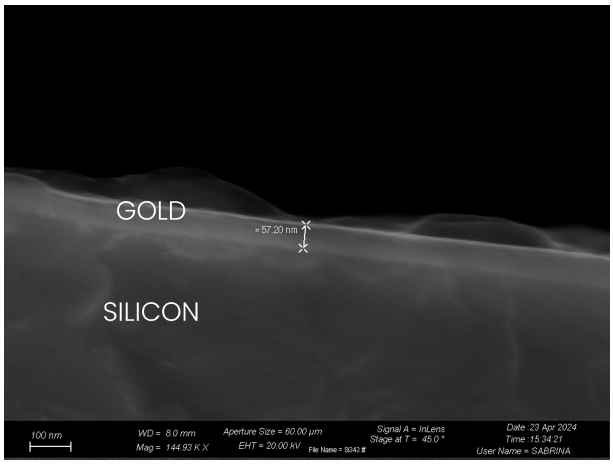

Fig. A.6 SEM image of the silicon reference sample.

Fiber Cutting and Connectorization

Following deposition, the extremities of each fiber were prepared for optical connection (Fig. A.7). The polymer coating at both ends was stripped, and the fibers were cleaved using a precision fiber cleaver to produce flat and perpendicular end faces. This preparation ensured compatibility with either temporary adaptors or permanent optical connectors, facilitating their subsequent integration into experimental setups.

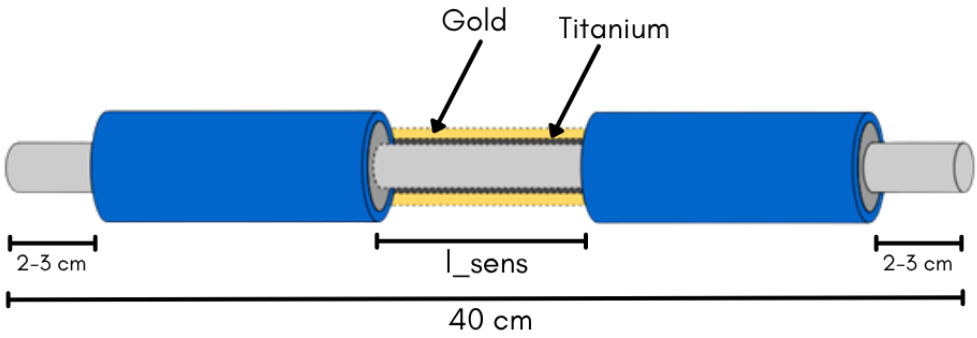

Fig. A.7 Schematic of the fiber with the deposited layers of gold and titanium on the silica core and the extremities stripped for the connection with sensing instruments.

Spectral Acquisition Set-up

The optical characterization of the fabricated sensors was performed through spectral transmission measurements. The experimental set-up consisted of the following components (see Fig. A.8):

1. A broadband LED light source with dedicated driver [75, 76].
2. The fabricated fiber-optic sensor.
3. An optical spectrometer [46].
4. A thermocouple for temperature monitoring [77, 78].

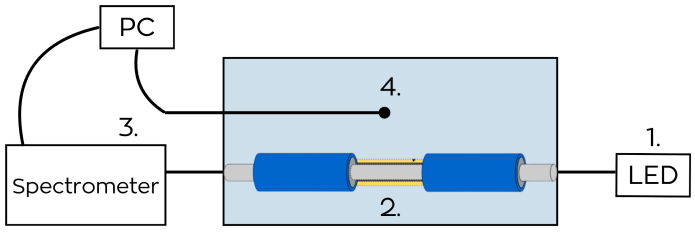

Fig. A.8 Schematic of the Set-up.

The light source was coupled to one end of the fiber sensor, while the opposite end was connected to the spectrometer. The spectrometer was interfaced with the computer via USB, and the LED driver was connected to the power supply. The sensing region of the fiber was positioned on a custom support capable of

accommodating liquid samples, enabling controlled immersion of the sensor into different media during testing.

Prior to data acquisition, the spectrometer parameters were carefully optimized. The integration time was set to approximately 8 ms in order to avoid detector saturation while ensuring adequate signal intensity. To minimize random fluctuations, signal averaging over 30 consecutive scans was performed, providing stable and reproducible spectral profiles. Under these conditions, well-defined transmission spectra were acquired, allowing the characteristic spectral features associated with surface plasmon resonance to be reliably observed and subsequently analyzed.

Data Processing Algorithm

Once the sensors had been fabricated and their spectral response verified under different surrounding media, attention was directed towards the development of a dedicated algorithm for data processing. The objective of this algorithm was to reliably extract and present information from the acquired spectra, enabling the detection of subtle changes in water composition. A key preliminary stage consisted of the preparation of the test solutions. For each refractive index under study, the corresponding aqueous solutions were prepared and subsequently characterized with a refractometer in order to determine their refractive indices. This procedure had to be repeated systematically for every solution and for every individual sensor tested, which significantly increased both the complexity and the duration of the overall process. The need to prepare, characterize, and handle multiple solutions for each experimental run represented one of the most time-consuming aspects of the workflow, yet was essential to establish a reliable reference dataset for later correlation.

Once the refractometric values had been obtained, the algorithm was applied to the spectral data acquired from the optical set-up. The processing workflow comprised several steps: loading of the reference spectrum (air), loading of the measured spectra (solutions), subtraction of the reference to isolate the resonance features (Fig. A.9), and extraction of the resonance minima. The minima were determined through three complementary approaches (direct minimum search, parabolic curve fitting, and centroid calculation) after the spectra had been smoothed to reduce high-frequency noise. Following this step, the wavelengths corresponding to the resonance minima were identified and correlated first with the solution concentrations

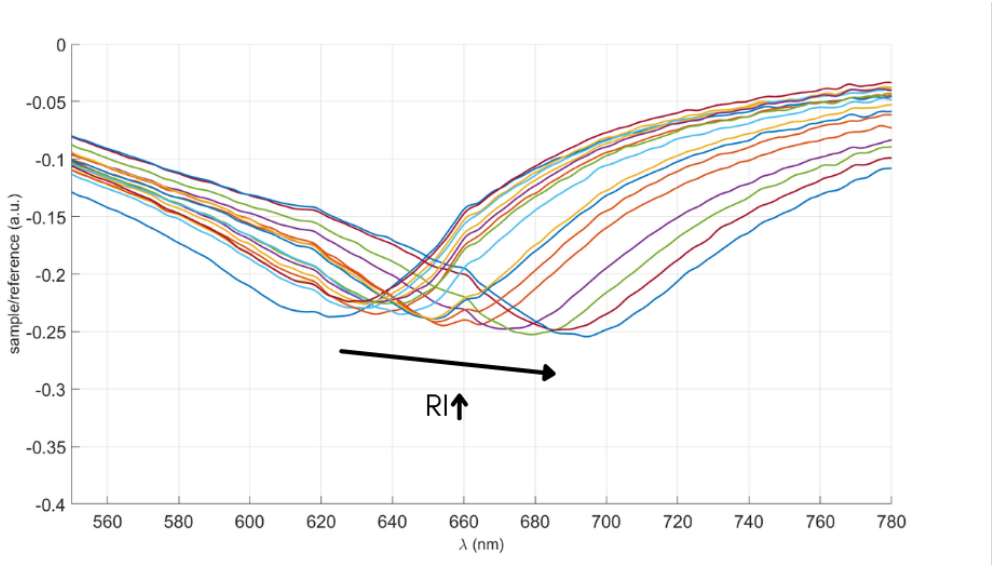

Fig. A.9 Example of pre-processed SPR spectra. An increase in refractive index (RI) results in a red shift of the resonance peak.

(Fig. A.10a) and subsequently with the refractive indices measured independently by the refractometer (Fig. A.10b).

A calibration curve was thus generated: Wavelength vs. Refractive Index. To establish the correlation, the refractometer data were fitted to obtain a continuous trend, onto which the resonance shifts detected by the sensor were mapped.

In summary, although the algorithm ultimately condenses the information into clear calibration graphs, the overall workflow is lengthy and technically demanding. The need to prepare and characterize multiple solutions for each sensor, combined with the multi-stage computational analysis of the spectra, makes the process both meticulous and labor-intensive. Nevertheless, each step, from solution preparation to spectral processing and refractometric correlation, was indispensable to ensure the robustness and reliability

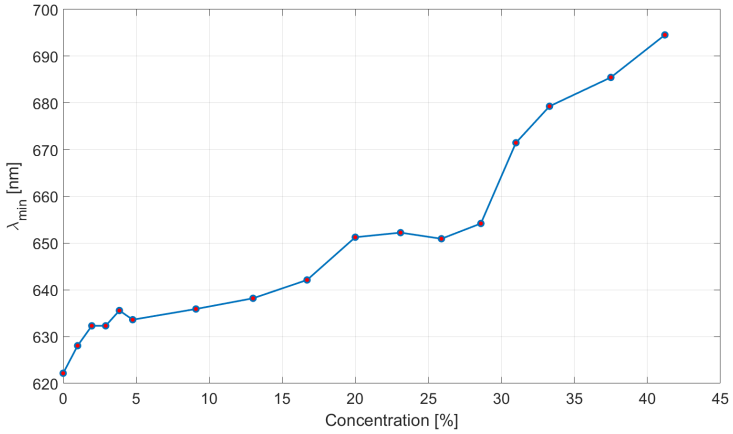

(a) Correlation between the wavelength of the minimum of the curve and the concentration of the solution under test.

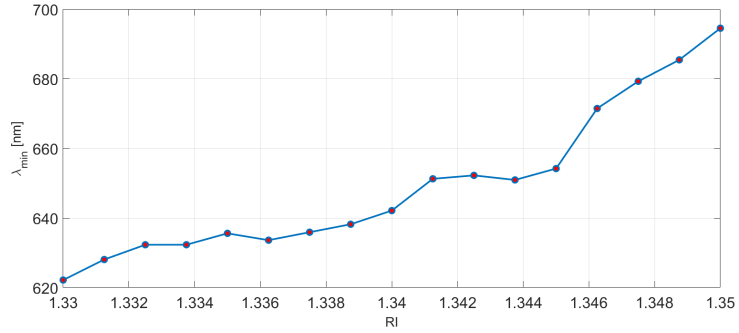

(b) Correlation between the wavelength of the minimum of the curve and the refractive index of the solution under test.

Fig. A.10 Correlation between the wavelength of the minimum of the curve and the concentration (a) and refractive index (b) of the solution under test.